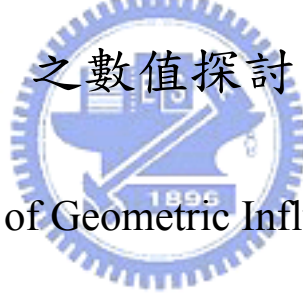


國立交通大學

機械工程學系

碩士論文

質子交換膜燃料電池中流道幾何形狀對其性能影響  
之數值探討



The Numerical Study of Geometric Influence of Flow Channel  
Patterns on Performance of PEMFC

研究生：陳長新

指導教授：陳俊勳 教授

中華民國九十八年六月

質子交換膜燃料電池中流道幾何形狀對其性能影響之數值探討

The Numerical Study of Geometric Influence of Flow Channel

Patterns on Performance of PEMFC

研究生：陳長新

Student : Chang-Hsin Chen

指導教授：陳俊勳

Advisor : Chiun-Hsun Chen

國立交通大學  
機械工程學系  
碩士論文



Submitted to Department of Mechanical Engineering

College of Engineering

National Chiao Tung University

in partial Fulfillment of the Requirements

for the Degree of

Master Science

in

Mechanical Engineering

June 2009

Hsinchu, Taiwan, Republic of China

中華民國九十八年六月


# 質子交換膜燃料電池中流道幾何形狀對其性能影響之數值探討

學生：陳長新

指導教授：陳俊勳

國立交通大學機械工程研究所碩士班

## 摘要



本論文係以數值模擬方法來探討不同幾何形狀的蛇形流場板對質子交換膜燃料電池的性能影響，並分析此項研究參數所得出的不同變數之分佈變化。本模擬使用商用套裝軟體 CFD-ACE+ 來建構一個穩態、三維、雙相流、多物種並包含電化學反應的數值模型。論文內容可分為三部分。第一部分主要是分析流場、溫度場及其他電化學變數在質子交換膜燃料電池內的基本現象。從模擬結果得知，電流密度、溫度以及水含量彼此的分佈情形呈現緊密的正相關性。而其中存在於邊緣勒條的些許差異來自於等溫的邊界條例。另外，這三項變數從陽極流道入口逐漸向陽極流道出口遞減，說明其分佈情形主要受制於氫氣濃度的影響。除此之外，當操作溫度超過 348K 時，液態水的生成變得相當微弱並未在電池內產生水氾濫的情形。第二部分主要是研究在兩個不同操作溫度(323K、353K)下不同彎道角度(45°、60

°、90°、120°與135°)的流場板對質子交換膜燃料電池的性能影響。數值計算結果顯示，因著質傳擴散速率的提升，結合60°與120°的流場板可以得到最好的性能尤其在低操作電壓下(0.4 - 0.6 V)。然而，不同角度的流場板的性能差異隨著操作溫度的降低而增加，說明彎道角度對性能的影響跟操作溫度呈負相關。另一方面，從薄膜溫度分佈圖中得知不同角度流場板的溫度分佈是相似的，說明改變流道角度並未能降低薄膜裡的溫度變化。

第三部分接著探討不同彎道寬度的流場板在相同於第二部分的操作條件下對質子交換膜燃料電池的性能影響。從模擬結果得知，因著物質擴散能力的提升，擁有較寬彎道的流場板可以得到最好的性能。然而，從電流密度及溫度的分佈圖中得知，該兩項變數在較寬彎道流場的薄膜中分佈地相當不平均並且伴隨著熱點存在於彎道裡，而此現象對薄膜的使用壽命有相當程度的傷害。

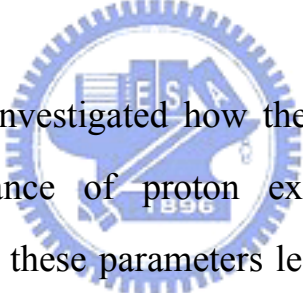
# The Numerical Study of Geometric Influence of Flow Channel Patterns on Performance of PEMFC

Student: Chang-Hsin Chen

Advisor: Prof. Chiun-Hsun Chen

Department of Mechanical Engineering  
National Chiao Tung University

## ABSTRACT



This study numerically investigated how the geometry of serpentine flow pattern influences performance of proton exchange membrane fuel cell (PEMFC), and analyzed how these parameters lead to different distributions of model variables. Three-dimensional simulations were carried out with a steady, two-phase, multi-component and electrochemical model, using CFD-ACE+, the commercial CFD code. This thesis consists of three parts. In first part, the fundamental behaviors of the flow field, temperature and the electrochemical variables inside a PEMFC are analyzed. From the numerical results, it shows a close and positive correlation between the distributions of current density, temperature and water content with only a slight discrepancy existing at the marginal rib due to isothermal conditions. Also, these three variables decrease gradually from anodic inlet toward anodic outlet, indicating that their distributions are principally dictated by the hydrogen concentration. Additionally, with the cell temperature increased beyond 348K, liquid water

formation doesn't appear to be considerable nor result in flooding effect inside the cell. In the second part, the effects of bend angle on the PEMFC performance is studied with various angles ( $45^\circ$ ,  $60^\circ$ ,  $90^\circ$ ,  $120^\circ$  and  $135^\circ$ ) with cell temperature of 323K and 353K. The numerical results indicate that the combination of  $60^\circ$  and  $120^\circ$  enables flow pattern to achieve the highest performance, especially at low operating voltages, due to the increase mass diffusion rate. Also, the differences in performance for different angles become more noticeable with decreasing cell temperature, implying that the influence of bend angle on the performance is inversely proportional to the operating temperature. On the other hand, the temperature distributions of flow patterns in the membrane with different angles are more or less similar indicating the variation of temperature in the membrane is not reduced from the change of bend angles. In the third part, the effects of bend width on the PEMFC performance are subsequently studied under the same operating conditions applied in the second part. Simulation results show that flow pattern with wider bend width achieves the highest performance compared to patterns with narrower width results from the enhanced mass diffusion. However, the distributions of current density and temperature in the membrane with wider bend show a high non-uniformity with the existence of hot spot at bending areas that is fatal to membrane lifetime.

## 誌 謝

回首兩年在實驗室的時光，雖不算長，但卻是刻骨銘心。從一開始模型的建立、測試到最後的收殮，有太多滾燙的淚水與無盡的感謝。能進入燃燒防火實驗室，心裡是感恩的，其中無數的試煉與挑戰，使我得以成長，也因此使我不斷的進步。

感謝我的恩師-陳教授。因著老師的教導、賞賜與肯定，使我能在大三時開始做專題研究，並在大四時進入實驗室學習並且申請到國科會大專生研究計畫，以及一年完成碩士學位的表現，對此我永遠感激在心。

謝謝好朋友暨學長的瑋圓，對於在研究及課業上給予許多的幫助，並且一起分享了生活中許多的快樂。謝謝俊翔學長在研究的事上給予了我許多的教導。謝謝育誠學長對於課業及事業給予了我許多的教導，並且在硬體上提供了相當大的幫助，使得模擬得以順利完成。謝謝耀文學長在課業上有許多的分享。謝謝遠達、彥成及榮貴三位學長對於論文上的教導與幫助。謝謝義嘉從大學時所分享的友情。謝謝家維、金輝、智欽及育祈學長們及信錡的關照。

最後的感謝歸於我的家人及親人，因著您們的關心及付出，使我渡過許多的難關，是您們的支持，使我不畏艱難。兩年在實驗室的生活，謝謝您們所給予我的幫助，這是耶穌基督的恩典，因著信靠使這工作得以完成。

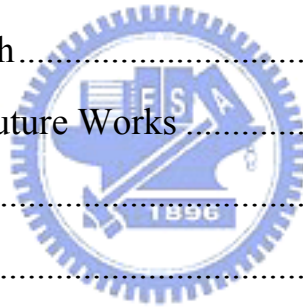


# CONTENTS

摘要 .....	i
ABSTRACT .....	iii
誌謝 .....	v
CONTENTS .....	vi
List of Tables .....	viii
List of Figures .....	ix
Nomenclature .....	xiii
Chapter 1 Introduction .....	1
1.1 Background .....	1
1.2 Literature Review .....	4
1.2.1 Modeling Development .....	4
1.2.2 Investigation of PEMFC Design and Operation .....	6
1.3 Scope of Present Study .....	10
Chapter 2 Simulation Model .....	15
2.1 Model Descriptions .....	15
2.2 Model Assumptions .....	17
2.3 Governing Equations .....	18
2.3.1 Continuity and Momentum Equations .....	18
2.3.2 Energy Equation .....	20
2.3.3 Species Equation .....	21
2.3.4 Electrochemical Reaction .....	23
2.3.5 Current Equation .....	24
2.3.6 Liquid Water Transport .....	25



2.3.7 Concentration Loss.....	28
2.4 Boundary Conditions.....	29
Chapter 3 Numerical Methods .....	35
3.1 Introduction to CFD-ACE+ software.....	35
3.2 Numerical Method for CFD-ACE+ .....	35
3.2.1 Finite-volume method .....	35
3.2.2 SIMPLEC scheme .....	37
3.3 Computational procedure of PEMFC simulation.....	40
Chapter 4 Results and Discussion.....	45
4.1 Fundamental Behaviors of Reference Case .....	46
4.2 Effects of Bend Angle .....	53
4.3 Effects of Bend Width.....	59
Chapter 5 Conclusions and Future Works.....	102
5.1 Conclusions .....	102
5.2 Future works.....	103
References .....	105



# List of Tables

Table 2.1 Geometries of Model .....	16
Table 2.2 Electrochemical parameters and transport properties.....	16
Table 3.1 Grid independence test.....	41
Table 3.2 Grid for different components.....	41
Table 4.1 Operating conditions of the reference case.....	45
Table 4.2 Operating conditions .....	53
Table 4.3 Operating conditions .....	59



# List of Figures

Fig. 1.1 Cross section of a PEMFC illustrating steps of electrochemical reaction and major structure.....	12
Fig. 1.2 Schematic of fuel cell I-V curve with three losses that influence the curve. ....	13
Fig. 1.3 Pictorial illustration of the effect of a leakage current loss on overall fuel cell performance.....	14
Fig. 2.1 Flow field pattern in PEMFC (a) 45-135; (b) 60-120; (c) 90-90, respectively.....	31
Fig. 2.2 Flow field pattern in PEMFC (a) 1007; (b) 1010; (c) 1020, respectively. ....	32
Fig. 2.3 Schematic of electrochemical reaction and the transfer current within a porous catalyst-containing conductor [33].....	33
Fig. 2.4 Schematic of the PEMFC mass transport model [3]. ....	34
Fig. 3.1 Grid structure of current model. ....	42
Fig. 3.2 Numerical flow chart of current study [33]. ....	43
Fig. 4.1 Polarization curve of reference case.....	64
Fig. 4.2 The specified number for each bend entrance along anodic flow channel where the corresponding values of Pe number are obtained.....	65
Fig. 4.3 The inverse of local Peclet number at each bend entrance (0.4V). ....	66
Fig. 4.4 Distribution of current density in the membrane at 0.4V.....	67
Fig. 4.5 Distributions of flow velocity in PEMFC at 0.4V: (a) anodic channel; (b) cathodic channel.....	68
Fig. 4.6 Distributions of temperature: (a) at anodic channel; (b) in the membrane; (c) at cathodic channel.....	69

Fig. 4.7 Distribution of hydrogen concentration on the interface between anodic GDL and catalyst layer at operating voltage of 0.4V. ....	70
Fig. 4.8 Distribution of oxygen concentration on the interface between cathodic GDL and catalyst layer at operating voltage of 0.4V. ....	71
Fig. 4.9 Distribution of water gas on the interface between cathodic GDL and catalyst layer and water flux in the membrane at operating voltage of 0.4V. ....	72
Fig. 4.10 Distribution of liquid water on the interface between cathodic GDL and catalyst layer at operating voltage of 0.4V. ....	73
Fig. 4.11 Distribution of water content in the membrane at 0.4V. ....	74
Fig. 4.12 Average values of temperature and water content for each current density. ....	75
Fig. 4.13 Polarization curves of flow patterns with three different bend angles at 323K and 353K. ....	76
Fig. 4.14 The inverse of Peclet number at each bend entrance ....	77
Fig. 4.15 Distributions of current density in the membrane at 323K (0.4V): (a) 45-135 flow pattern; (b) 60-120 flow pattern; (c) 90-90 flow pattern. ....	78
Fig. 4.16 Distributions of current density in the membrane at 353K (0.4V): (a) 45-135 flow pattern; (b) 60-120 flow pattern; (c) 90-90 flow pattern. ....	79
Fig. 4.17 Distributions of temperature in the membrane at 323K (0.4V): (a) 45-135 flow pattern; (b) 60-120 flow pattern; (c) 90-90 flow pattern. ....	80
Fig. 4.18 Distributions of temperature in the membrane at 353K (0.4V): (a) 45-135 flow pattern; (b) 60-120 flow pattern; (c) 90-90 flow pattern. ....	81
Fig. 4.19 Average value of temperature in the membrane at 323K and 353K. ..	82
Fig. 4.20 Distributions of water content in membrane at 323K (0.4V): (a) 45-135 flow pattern; (b) 60-120 flow pattern; (c) 90-90 flow pattern. ....	83
Fig. 4.21 Distributions of water content in membrane at 353K (0.4V): (a) 45-135	

flow pattern; (b) 60-120 flow pattern; (c) 90-90 flow pattern. ....	84
Fig. 4.22 Average value of membrane water content at 323K. ....	85
Fig. 4.23 Average value of membrane water content at 353K. ....	86
Fig. 4.24 Distributions of saturation on the interface between cathodic GDL and catalyst layer at 323K. ....	87
Fig. 4.25 Distributions of saturation on the interface between cathodic GDL and catalyst layer at 353K. ....	88
Fig. 4.26 Polarization curves of flow patterns with three different bend widths at 323K and 353K. ....	89
Fig. 4.27 The inverse of Peclet number at each bend entrance. ....	90
Fig. 4.28 Distributions of current density in membrane at 323K (0.4V): (a) 1007 flow pattern; (b) 90-90 flow pattern; (c) 1020 flow pattern. ....	91
Fig. 4.29 Distributions of current density in membrane at 353K (0.4V): (a) 1007 flow pattern; (b) 90-90 flow pattern; (c) 1020 flow pattern. ....	92
Fig. 4.30 Distributions of temperature in membrane at 323K (0.4V): (a) 1007 flow pattern; (b) 90-90 flow pattern; (c) 1020 flow pattern. ....	93
Fig. 4.31 Distributions of temperature in membrane at 353K (0.4V): (a) 1007 flow pattern; (b) 90-90 flow pattern; (c) 1020 flow pattern. ....	94
Fig. 4.32 Average value of temperature in membrane at 323K and 353K. ....	95
Fig. 4.33 Distributions of water content in membrane at 323K (0.4V): (a) 1007 flow pattern; (b) 90-90 flow pattern; (c) 1020 flow pattern. ....	96
Fig. 4.34 Distributions of water content in membrane at 353K (0.4V): (a) 1007 flow pattern; (b) 90-90 flow pattern; (c) 1020 flow pattern. ....	97
Fig. 4.35 Average value of membrane water content at 323K. ....	98
Fig. 4.36 Average value of membrane water content at 353K. ....	99
Fig. 4.37 Distributions of saturation on the interface between cathodic GDL and	

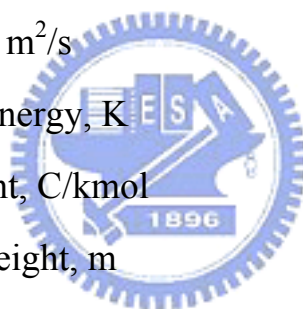
catalyst layer at 323K..... 100

Fig. 4.38 Distributions of saturation on the interface between cathodic GDL and  
catalyst layer at 353K..... 101



# Nomenclature

a	Water activity
$a_i$	Stoichiometric coefficient
A	The y-dir. position in channel, m
B	Body force, N
$c_{\text{ref}}$	Reference molar concentration, kmol/m <sup>3</sup>
$c_C^R$	Molar concentration of hydrogen in channels, kmol/m <sup>3</sup>
$c_L^R$	Molar concentration of hydrogen in catalyst layer, kmol/m <sup>3</sup>
$C_p$	Specific heat, J/kg K
$D_{\text{eff}}$	Gas effective diffusivity, m <sup>2</sup> /s
D	Gas diffusivity, m <sup>2</sup> /s
E	Characteristic energy, K
F	Faraday constant, C/kmol
$H_C$	Flow channel height, m
$H_G$	GDL height, m
h	Mixture enthalpy, J/kg
$J_C^{\text{conv}}$	The mass flow rate from channels to GDL, kg/s
$J_G^{\text{diff}}$	The mass flow rate from GDL to catalyst layer, kg/s
i	Current, A
J	Mass flux, kg/m <sup>2</sup> s
j	Net current density, A/m <sup>2</sup>
$j_0$	Reference current density, A/m <sup>2</sup>
k	Boltzmann constant, eV/K
$k_{\text{eff}}$	Thermal conductivity, W/m K
M	Molecular weight, kg/kmol



p	Absolute pressure, Pa
q	Heat flux, J/m <sup>2</sup>
R	Universal gas constant, kJ/kmo K
S	Surface area, m <sup>2</sup>
Sh	Sherwood number
T	Temperature, K
U	Fluid velocity, m/s
V	Volume, m <sup>3</sup>
Y	Fluid mass fraction

#### Greek Symbols

$\alpha$	Mass transfer coefficient
$\beta$	Kinetic constant
$\delta$	Diffusion scale length, m
$\varepsilon$	porosity
$\zeta$	Relative mobility
$\rho$	Fluid density, kg/m <sup>3</sup>
$\eta$	Overpotential, V
$\kappa$	Permeability
$\lambda$	Water content
$\mu$	Dynamic viscosity, kg/m s
$\sigma$	Electrical conductivity 1/ $\Omega$ m
$\tau$	Shear stress tensor, N m <sup>2</sup>
$\tau$	Tortuosity
$\varphi$	concentration exponent





$\omega$	Production rate of water, $\text{kg/m}^3 \text{ s}^1$
$\Phi$	Electrical potential, V
$\Omega$	Collision integral

### Superscripts

conv	Convection
diff	Diffusion
K	Reaction kinetics
N	Nerst
R	Molar
tot	Total
*	Dimensionless



### Subscripts

an	Anode
atm	Atmosphere
C	Flow direction
ca	Cathode
con	Concentration losses
d	Dry state
eff	Effective value
F	Fluid
G	GDL
h	Enthalpy
in	Inlet

L	Catalyst layer
mix	Mixture
re	Reversible
S	Solid
sat	Saturation



# Chapter 1

## Introduction

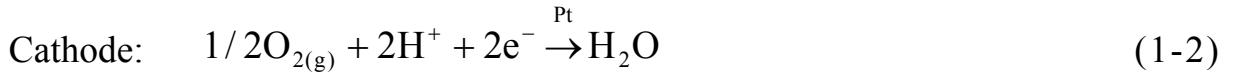
### 1.1 Background

Carbon dioxide generated during combustion of fossil fuels is inextricably linked to the greenhouse effect. Carbon dioxide, as other greenhouse gases, is essential to maintain the temperature of the earth. However, an excess of carbon dioxide can raise the temperature of our planet to lethal levels by absorbing and emitting infrared radiation. During the pre-industrial Holocene, the concentration of carbon dioxide was roughly 280ppm. Since then, the current concentration has grown to 384ppm, and the current global temperature has increased by 0.75°C since 1860, revealing a close bond between the growth of carbon dioxide concentration and global warming [1]. Besides, the efficiency of traditional engine is limited by Carnot cycle, according to thermodynamics. Therefore, research investigating new and clean energies has attracted considerable attention since the last decades of 20<sup>th</sup> century.

Proton exchange membrane fuel cell (PEMFC), as one of the most effective and clean technologies, may replace crude oil for generating power, and can be employed in cell phones, automobiles and power plants. The advantages of PEMFC are high efficiency, simplicity, low emissions and silence. Therefore, PEMFC, directly converting chemical energy to electricity, has received people's attention and comprehensive study, and furthermore, it may become the dominant new power source in the future.

During the power conversion process inside of PEMFC, the oxidation

reaction happens at the anode because electrons are being liberated from hydrogen by the reaction, and electrons are being combined with oxygen at the cathode by the reduction reaction. The anode, cathode and overall reaction are:



It should be noticed that the state of water could be either liquid or gas. The conditions that the final state of water depends on are complex, including saturation pressure, relative humidity, water content and temperature.

As shown in Fig. 1.1, the humidified hydrogen is supplied into the anode flow pattern and then it passes through the channel, meanwhile, some of the hydrogen molecules enter into gas diffusion layer (GDL). GDL made of carbon cloth provides gases an access to catalyst layer, enhances electrical conductivity and alleviates flooding effect. After that, hydrogen diffuses to anode catalyst layer, an extremely thin layer of platinum-based catalyst. Oxidation reaction happens at the anode catalyst layer, therefore, hydrogen molecules are oxidized to electrons and hydrogen ions also known as protons. Subsequently, electrons are conducted back to GDL or anode flow pattern and travel to cathode via external circuit. In the meanwhile, hydrogen ions proceed through polymer electrolyte membrane to cathode side.

As both electrons and hydrogen ions keep arriving at cathode catalyst layer, oxygen also reaches cathode catalyst layer by flowing through channel and passing through GDL. Reduction reaction happens as these three elements combine to form water, and heat is generated from this reaction. Some of the water produced from reduction reaction is drained off to flow channel and then

exits a PEMFC. Others would diffuse from cathode side to anode via the membrane. This back-diffusion phenomenon of water depends on the thickness of the electrolyte membrane and the relative humidity of each side.

At STP, thermodynamics dictates that the reversible voltage attainable from a PEMFC is 1.23V [2, 3]. However, the output voltage of a real cell decreases as current load is applying. The decrease based on three imperative losses provides a characteristic shape in the fuel cell current–voltage (I–V) curve for a PEMFC. The three losses are:

- 1 Activation losses. A proportion of voltage generated is lost in driving the chemical reaction that transfers the electrons to or from electrode.
- 2 Ohmic losses. This voltage drop is the straightforward resistance to the flow of electrons through the material of the electrodes and the various interactions, as well as the resistance to the flow of ions through electrolyte.
- 3 Concentration losses. These results from the change in concentration of the reactants at the reaction surfaces as gases are supplied. Accordingly, voltage drops due to the insufficiency of concentration.

The three losses each dominates at different parts of I–V curve are shown in Fig. 1.2. The activation losses mostly affect the initial part of the curve; the ohmic losses are most apparent in the middle section of the curve, and the concentration losses are dominant in the tale of the I–V curve. Additionally, there exists an additional term associated with the parasitical loss due to current leakage and gas crossover which has a significant impact on the reversible voltage and is the reason why the actual reversible voltage is lower compared with theoretical value. Pictorially, this loss is illustrated in Fig. 1.3.

## 1.2 Literature Review

### 1.2.1 Modeling Development

Because of the high cost of PEMFC manufacturing, modeling and simulation has been developed extensively in research across the world to acquire better understanding of the fundamental processes. With deeper insight for the processes, the design cycle can be shortened substantially and the performance can be improved.

Bernardi and Verbrugge [4] proposed a one-dimensional, half-cell mathematical model for a single cell. The transport of charge and species were based on Nerst-Planck equation. And the motion of liquid water was modified by Schlogl's velocity equation, the current transfer between membrane and solid conductor of catalyst layer were dominated by Butler-Volmer equation and the diffusivity of multi-species gas mixture was based on Stefan-Maxwell equations. Springer et al. [5] proposed an isothermal, one-dimensional, steady model for a full cell with 117 Nafion membranes. It showed that an increase in membrane resistance with increased current density and demonstrates the great advantage of a thinner membrane in alleviating this resistance problem. After a year, Bernardi and Verbrugge [6] developed the original half-cell model into a full-cell one. To get deeper insight for the gas concentration distribution and current transfer in PEMFC, a two-dimensional model was developed subsequently. Wang and Cheng's team [7] proposed a two-dimensional model for the transport of multi-phase and multi-component gases mixture in porous medium. The results revealed that the uneven oxygen concentration profile can cause the uneven distribution of current on the chemical reaction surfaces, and the decrease of current density is due to the formation of liquid water that

decreases the oxygen concentration near the reaction surfaces. The threshold current density for single-phase and two-phase models can be obtained from this model, therefore to investigate the water transport phenomenon and the gas distribution on the cathode side. He et al. [8] proposed a PEMFC model which was two-dimensional and steady. The thermal diffusivity and evaporation speed were assumed to be constant, and therefore, the phase-change speed was limited during the reaction. The results revealed that the transport of liquid water in the porous electrodes is dominated by the shear stress and capillarity which are generated from gas and liquid water motion. In the two-dimensional model proposed by Um et al. [9] where the presence of hydrogen dilution is considered, ohmic losses is neglected in GDL and catalyst layer, hence, electronic phase is uniform across them. And oxygen is assumed to dissolve in electrolyte in catalyst layer and membrane regions. The results revealed that hydrogen was depleted at the reaction surface, resulting in substantial anode mass transport polarization, and hence, a lower current density that is limited by hydrogen transport from fuel stream to reaction site. Wang et al. [10] studied the transport phenomena of air in the cathode with two-phase model. The model was able to handle the situation where a single-phase region co-exists with a two-phase zone in the air cathode. And the results showed that capillary action is the dominant mechanism for water transport inside the two-phase zone of the hydrophilic structure. Mazumder and Cole [11, 12] proposed an accurately three-dimensional, mathematical model. This full-cell model was included in the package CFD-ACE+ produced by ESI-CFD. The model was mainly based on the multi-phase gas model from Wang et al. [7] and He et al. [8]. Thus, this model can simulate the two-phase phenomenon and the transportation of liquid water in the porous media. Also, it was constructed energy equation to solve

the problem of temperature field. Results were compared against experimental data under various operating conditions, and showed that three-dimensional modeling is the key to predicting performance of PEMFC at high current densities instead of two-dimensional one. And it also revealed that inclusion of liquid water transport greatly enhances the predictive capability of the model and is necessary to match experimental data at high current densities.

### **1.2.2 Investigation of PEMFC Design and Operation**

PEMFC performance is strongly dominated by operating temperature, inlet relative humidity (RH) and flow pattern etc. Proper operating temperature leads to high reaction rate and low activation and ohmic losses. Appropriate RH prevents water clogging effect, moisturizes the membrane and increase the electrical conductivity of membrane. Besides, the performance of PEMFC is also depended on the distributions of reactant species, and therefore, the primary goal of flow pattern design is to increase reactant species uniformity, which can lead to uniform distributions of current density and temperature. Thus, performance would be improved, the lifetime of PEMFC would be extended, and the water flooding effect would be alleviated.

Hontañón et al. [13] tested various widths of flow channels and ribs to determine the effect of reactant species' consumption. According to this study, optimal rib width is 1mm, and optimal channel widths are 3 and 4 mm, instead of not 1 mm. In addition, the optimal consumption rate is 45.7%. Scholta et al. [14] investigated the mass transport and electrical conductivity of a flow pattern by varying the width of channels and ribs. Their analytical results showed that an optimum value of 0.7-1 mm applies to channel and rib widths. For wide dimensions of width, the influence on mass transport or lateral electrical conductivity is significant. For very small dimensions of widths, the



manufacturing effort becomes excessively high and the probability of channel clogging via the formation of water droplets increases. The influence of aspect ratio (AR) channel height to width—was tested by Chiang and Chu [15]. According to their simulation results, membrane electrical conductivity increases when AR decreases. Shimpalee and Van Zee [16] investigated how serpentine flow fields with different channel/rib cross-sectional areas affect performance and species distributions for both automotive and stationary conditions. Their simulation results revealed that for a stationary condition, a narrow channel with wide rib spacing improves performance; however, the opposite occurs when the automotive condition is applied.

In order to study the effect of humidity on the performance, Fell et al. [17] assessed the performance of experimental flow-field designs under different levels of humidity by utilizing a single-phase isothermal model of PEMFC segments. Shimpalee [18] studied the humidification effect numerically and experimentally. The results indicated that dry steams on either anode or cathode cause a low membrane electrical conductivity and performance. On the other hand, super-saturation streams results in a higher current density such that improves the performance. A few years later, Matamoros and Brüggemann [19] adopted steady and three-dimensional models to investigate the influence of geometrical parameters on the performance under different hydrating conditions. According to their results, anode and cathode liquid water saturation affects species transport and the polymer electrolyte water content. Thus, one must simultaneously calculate both water absorption and desorption through the polymer electrolyte and liquid water saturation in anode and cathode porous media to acquire an actual view of ohmic and concentration losses in PEMFC performance. The performance of PEMFC is considerably improved by

applying 100% RH at inlet flow in comparison with 50% RH, and such better performance is achieved especially at high current densities. Zhang et al. [20] studied the effect of RH on the performance as well. The fuel cells were performed at a typical high temperature 120°C, ambient pressure and various RHs from 25% to 100%. The experimental results indicated that the membrane resistance at 25% RH is about five times higher than that at 100%. At high RHs, the membrane adsorbs more water than at low RHs which enable more ionic clusters are filled with water, and therefore, protons can transport easily as free ions through membrane, results in low membrane resistance. As expected, the PEMFC performance increases dramatically with increasing RH.

Since temperature plays an important role in PEMFC operation, the investigations for the effect of temperature on PEMFC is necessary. Coppo et al. [21] proposed a three-dimensional model that accounts for water transport in the liquid, gas and dissolved phases to study the effect of temperature-dependent parameter variations on cell performance. The results showed that in the activation regime of the polarization curve, the performance of PEMFC is mainly improved by high temperature that leads to high values of both exchange current density and charge transfer coefficient. In ohmic region of the polarization curve, benefits of running the cell at high temperature can be explained with the high membrane ionic conductivity and an increase of water diffusivity as well as water content, which results in a decrease of electrical resistance to ion transport. Al-Baghdadi [22] numerically investigated the effect of temperature distribution on material deformation. According to the results, the non-uniform distribution of stresses, caused by the temperature gradient and moisture change in the cell, induces localized bending stresses and deformation, which can contribute to delaminating between membrane, GDL

and bipolar plates, especially in the cathode side. Also, the results indicated that the maximum von Mises stress exists on the corner of flow channels and the interface between membrane and GDL.

The effects of the permeability of the electrodes and the type of gas flow distributors on the PEMFC performance were investigated by Soler et al. [23]. The results of simulation showed that the effect of permeability is not notable in the case of grooved plates, but it is rather significant in case of the solid plates. The results also revealed that the performance with solid plates declines when the permeability of the electrodes decreases. Oosthuizen et al. [24] numerically tested the effect of channel-to-channel gas crossover on the pressure and temperature distribution. The results revealed that flow crossover is only significant when the porosity of the GDL exceeds approximately 0.65. And flow crossover tends to decrease the pressure drop across the flow channel. Also, the dominant factor in determining the temperature is the thermal conductivity of the flow plate material instead of the crossover. Shimpalee et al. [25] investigated various channel path lengths to estimate the impact of flow path length on temperature distributions, current density distributions and the performance. According to their results, local temperature, water content and current density distributions become more uniform under serpentine flow-field designs with shorter path lengths or greater number of channels. Karvonen et al. [26] proposed a parallel flow pattern that had uniform flow distribution by both numerical and experimental analyses. The inlet distributor of flow pattern is narrowed that leads to a better equality of flow velocities in different channels. The difference between the largest and the smallest velocities is decreased from 16% to 8%. Sun et al. [27] presented a model considering a serpentine flow channel with trapezoidal cross-section shape. The obtained results indicated

that an increase in the trapezoidal cross-section shape ratio  $R$  is associated with an increase in the flow-cross through GDL. And  $R$  has a significant effect on the pressure variation in the flow field. As  $R$  value increases, the pressure drop increases slightly for the cross-over case. Also, an increase in  $Re$  is associated with a slight increase in the flow cross-over. Park and Li [28] numerically and experimentally studied the characteristics and effect of cross flow through the porous electrode structure between two adjacent flow channels. The results indicated that the thickness and permeability of the GDL are the two most important parameters influencing the cross flow and the resultant pressure drop. Another numerical investigation on the influence of flow pattern geometry was carried out by Jeon et al. [29] for four  $10\text{ cm}^2$  serpentine flow-fields with single channel, double channel, cyclic-single channel and symmetric-single channel patterns at 100% and 64% inlet HR. According to their results, the double channel flow-field was found to have the highest performance at 100% inlet HR and to have most uniform current density distribution. However, for 64% inlet HR, there were little difference on performance and current density uniformity among the four serpentine flow-field patterns.

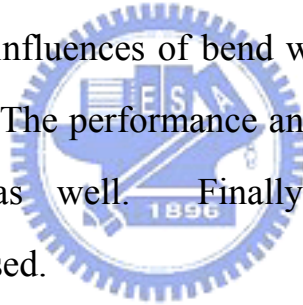
### **1.3 Scope of Present Study**

According to the results of reference [16], low current density is observed at the bending area of flow channels, where low water content and high temperature are presented. The non-uniform distribution of water and temperature will seriously cause mechanical damage to the membrane and shorten its lifetime. Therefore, the flow pattern design in this research will focus on the improvement of cell performance and the increase of distribution

uniformity of current density, temperature and water content.

This research applies a commercial package software, CFD-ACE+, for the full-cell simulation. The investigation mainly concerns on the improvement of flow-field design by changing the bend angles and widths in flow channels. Simulations are performed in a steady, two-phase and three-dimensional model with different flow channel patterns at different operating temperatures.

This numerical investigation consists of two parts. The first one is to study the effects of bend angle on PEMFC performance with three different flow patterns at two different operating temperatures, 323K and 353K. Comparisons will be given afterward to discuss how the performance and variables distributions change with bend angle. Another part of the investigation is to study the influences of bend width under the same operation conditions as the first part. The performance and variable distributions will be compared and analyzed as well. Finally, the advantages of those configurations will be discussed.



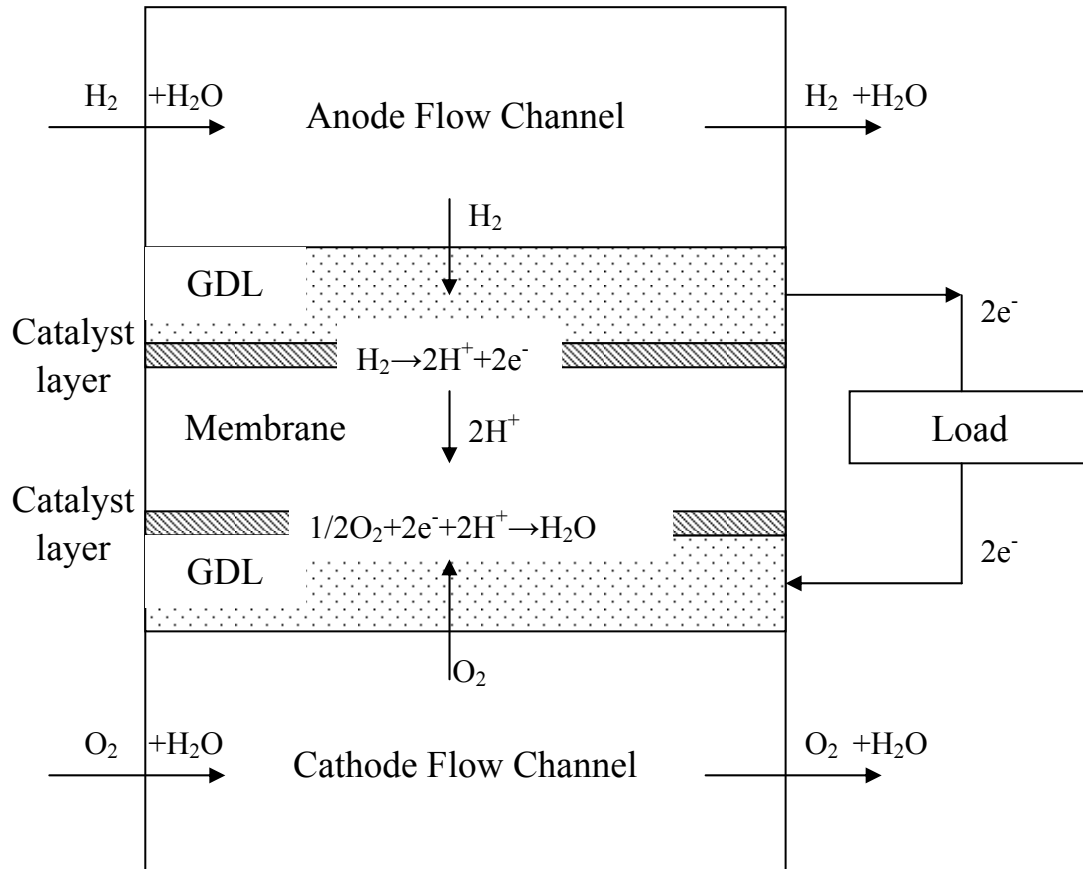


Fig. 1.1 Cross section of a PEMFC illustrating steps of electrochemical reaction and major structure.

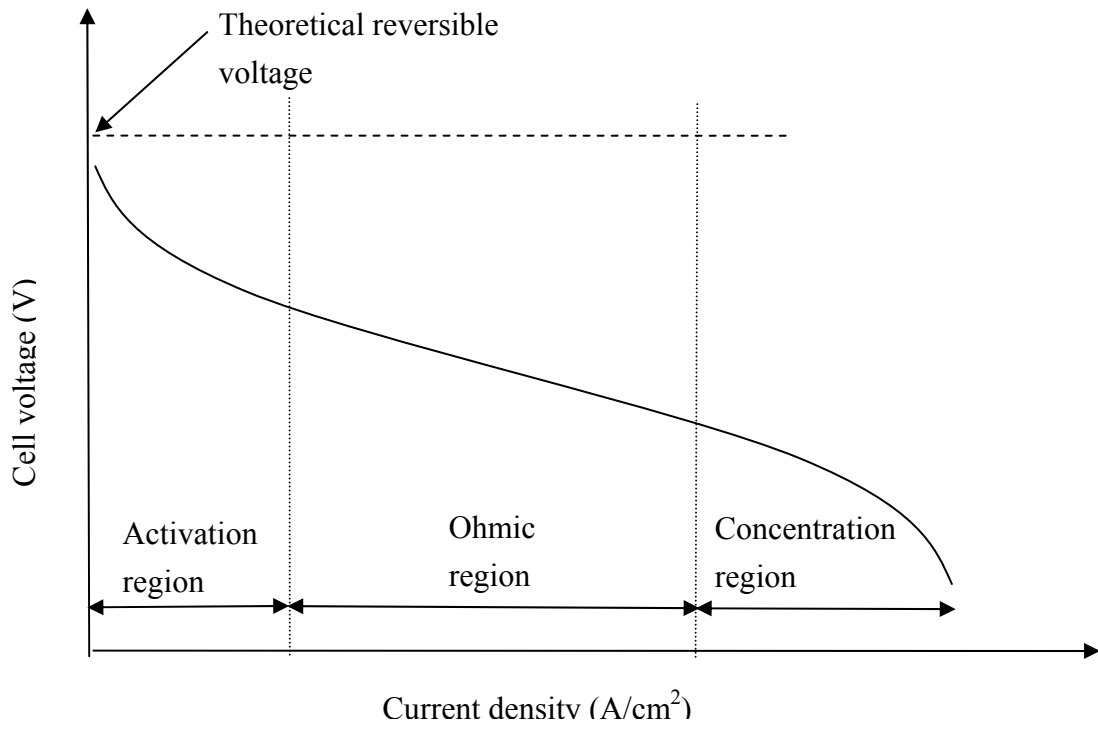
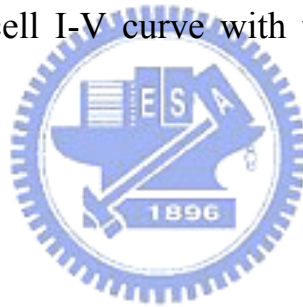


Fig. 1.2 Schematic of fuel cell I-V curve with three losses that influence the curve.



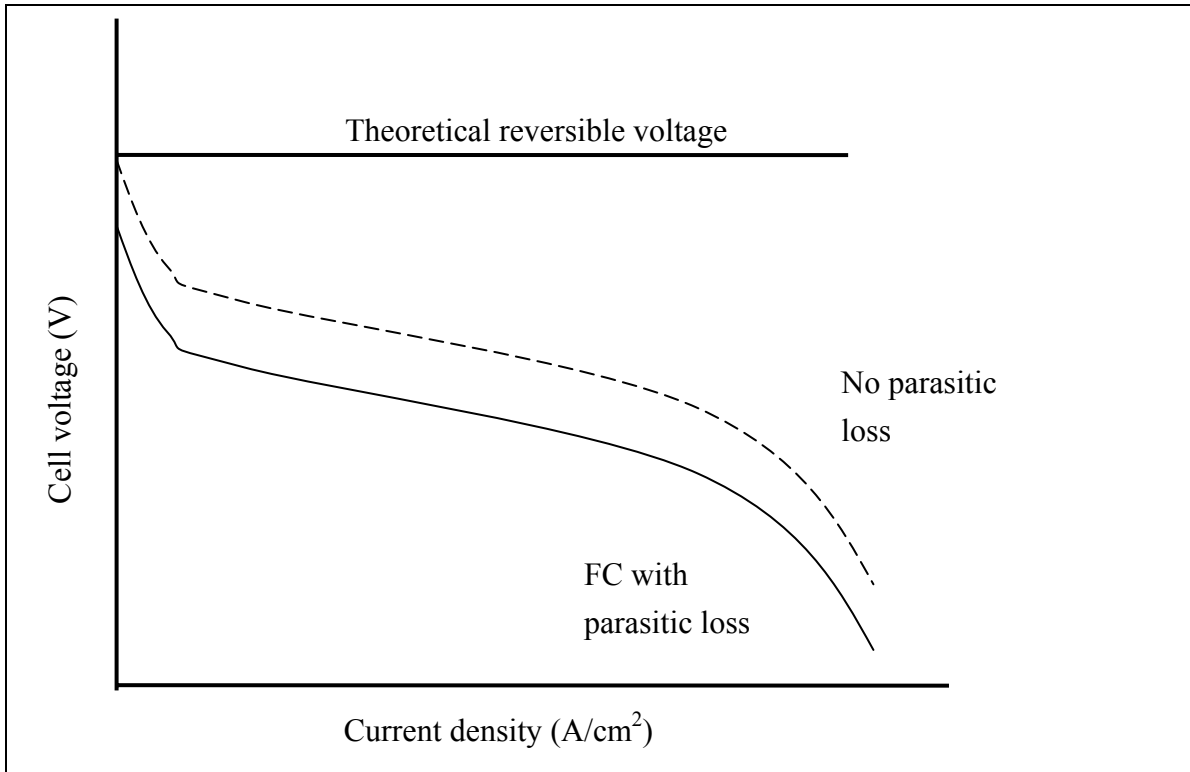


Fig. 1.3 Pictorial illustration of the effect of a leakage current loss on overall fuel cell performance.





# Chapter 2

## Simulation Model

The convenience of computational fluid dynamic (CFD) provides a low-cost way to study PEMFC and enables researchers to precisely understand the flow and temperature fields inside PEMFC. Besides, the distribution of chemical parameters can be studied and the effect of each parameter can also be further compared. Based on the governing equations that describe the correlations of various properties can be developed and solved by numerical methods, providing the necessary information for PEMFC design.

### 2.1 Model Descriptions

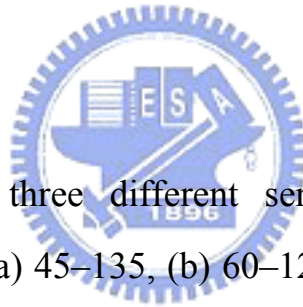


Figure 2.1 shows the three different serpentine flow patterns under investigation of bend angle (a) 45–135, (b) 60–120 and (c) 90–90, respectively. The first number in each pattern represents the first angle of the channels, and the second number represents the second angle. These two are combined to generate a complete u-turn flow channel. In addition, the patterns for investigation on the effect of bend width are shown in figure 2.2. Patterns (a) 1007, (b) 90–90 and (c) 1020, are considered. The first two numbers, 10's, represent the channel width of 1 mm, and the last two numbers, 07 and 20, represent the bend width of 0.7 mm and 2.0 mm, respectively. 90–90 is the most conventional flow pattern applied in most researches and is considered as a reference for comparison in this study. According to the results from Scholta et al. [14], the channel and rib dimension ratio of this model is 0.5 which would lead to superior performance. Based on the results from Chiang and Chu [15],

the AR is chosen to be 1 which provides the most uniform membrane conductivity. Table 2.1 shows the detailed geometries of current model. The electrochemical parameters and transport properties from Springer et al. [5] and Mazumder and Cole [11, 12] are listed in Table 2.2.

Table 2.1 Geometries of Model

<b>Geometry</b>	<b>Vlaues</b>
Reaction area	25 (cm <sup>2</sup> ), 5×5
Channel Width	1 (mm)
Channel Depth	1 (mm)
Rib Width	2 (mm)
GDL Thickness	0.3 (mm)
Catalyst Layer Thickness	10 (μm)
Membrane (Nafion117) Thickness	163 (μm)

Table 2.2 Electrochemical parameters and transport properties

<b>Parameter</b>	<b>Values</b>
<b>Electrochemical parameters</b>	
Transfer coefficients at anode	0.5
Transfer coefficients at cathode	1.5
Concentration dependence of H <sub>2</sub>	0.5
Concentration dependence of O <sub>2</sub>	1
<b>GDL and catalyst layer</b>	
GDL and catalyst layer porosity	0.4

GDL and catalyst layer permeability	$1.76 \times 10^{-11}$
Tortuosity	1.5
Electrode conductivity of catalyst layer	53 (1/ohm m)
Effective surface to volume ration of catalyst layers	1000
<b>Membrane</b>	
Membrane porosity	0.28
Membrane permeability	$1.8 \times 10^{-18}$
Tortuosity	5
Electrode conductivity of membrane	$1 \times 10^{-20}$ (1/ohm m)
<b>Bipolar Plates</b>	
Electrical conductivity	Temperature dependence
Reference Temperature	293 (K)
Electrical conductivity at reference Temperature	$3.5 \times 10^{-18}$ (ohm m)
Temperature coefficient at reference Temperature	$5 \times 10^{-4}$

## 2.2 Model Assumptions

The following assumptions are utilized to simplify simulation conditions.

1. All fluids are treated as continuums.
2. Gases are ideal gases throughout the entire model.
3. The velocity and temperature of reactant species are distributed uniformly over the channel inlet.

4. The flows are incompressible and laminar due to small Reynolds number.
5. The gas diffusion layer (GDL), catalyst layers and membrane are all isotropic porous media with pores uniformly distributed.
6. Gravity is neglected.
7. No fuel crossover.
8. Evaporation and condensation of water is neglected.
9. Dissolution of gases in the liquid is neglected.
10. The phenomenon of double charge layer is not considered.

## 2.3 Governing Equations

The steady, two-phase and three-dimensional model is basically modified from the one proposed by Mazumder and Cole [11, 12]. The flow pattern has been developed from a single channel to a full-size serpentine channel with 25cm<sup>2</sup> reaction area. The membrane domain is built for Nafion 117, and the data is available from Springer et al. [5].

The PEMFC model consists of five volume-averaged conservation equations, which are mass, momentum, energy, species and electric current conservation equations. All the equations are applied in every domain of the model. In addition, fluxes across any two different domains are automatically continuous.

### 2.3.1 Continuity and Momentum Equations

The continuity equation and momentum conservation equations are as follows

$$\frac{\partial}{\partial t}(\epsilon_{\text{eff}}\rho) + \nabla \cdot (\epsilon_{\text{eff}}\rho\mathbf{U}) = 0 \quad (2-1)$$

$$\frac{\partial}{\partial t}(\varepsilon_{\text{eff}}\rho U) + \nabla \cdot (\varepsilon_{\text{eff}}\rho U U) = -\varepsilon_{\text{eff}}\nabla p + \nabla \cdot (\varepsilon_{\text{eff}}\tau) + \varepsilon_{\text{eff}}B + \frac{\varepsilon_{\text{eff}}^2\mu U}{\kappa} \quad (2-2)$$

where  $\rho$  is the fluid density,  $U$  is the fluid velocity,  $p$  is the pressure,  $\tau$  is the shear stress tensor,  $B$  is the body force,  $\mu$  is the dynamic viscosity of the fluid,  $\varepsilon_{\text{eff}}$  is the effective porosity of the medium, and represents the ratio of the volume occupied by the pores to the total volume of porous medium while the permeability  $\kappa$ , is the square of the effective volume to surface area ratio of porous medium. The last term in Eq. (2-2) represents Darcy's drag force imposed by pore walls on the fluid, and leads to a significant pressure drop across the porous medium. In a purely fluid region,  $\varepsilon_{\text{eff}} \rightarrow 1$  and  $\kappa \rightarrow \infty$ , and the standard Navier-Stokes equation is recovered.

For high accuracy, mix kinetic theory is chosen to estimate the viscosity value of mixture in this research, and is expressed as

$$\mu_{\text{mix}} = \frac{\sum_{i=1}^N x_i \mu_i}{\sum_j x_j \Phi_{ij}} \quad (2-3)$$

where  $x_i$  and  $x_j$  are the mass fraction of species  $i$  and  $j$ ,  $\mu_i$  is the dynamic viscosity of species  $i$  and  $\Phi_{ij}$  is the dimensionless quantity. The dynamic viscosity data input form [29] is linearly interpolated for each species. And the dimensionless quantity is given by

$$\Phi_{ij} = \frac{1}{\sqrt{8}} \left( 1 + \frac{M_i}{M_j} \right)^{-1/2} \left[ 1 + \left( \frac{\mu_i}{\mu_j} \right)^{1/2} \left( \frac{M_j}{M_i} \right) \right]^2 \quad (2-4)$$

where  $M_i$  is the molecular weight of species  $i$ ,  $T$  is the temperature in Kelvin,  $\sigma_i$  is the characteristic diameter of the molecular in Angstroms and  $\Omega_\mu$  is the collision integral and is given by

$$\Omega_{\mu} = \frac{1.16145}{T^{*0.14874}} + \frac{0.52487}{\exp(0.77320T^*)} + \frac{2.16178}{\exp(2.43787T^*)} \quad (2-5)$$

where  $T^*$  is the dimensionless temperature and is defined as

$$T^* = \frac{kT}{E} \quad (2-6)$$

where  $k$  is the Boltzmann's constant and  $E$  is the characteristic energy. The details are given by Incropera [30], Wilke [31] and Hirschfelder et al. [32].

### 2.3.2 Energy Equation

The temperature field of each domain can be obtained from solving the energy conservation equation. The energy conservation equation can be written as

$$\frac{\partial}{\partial t} [(1 - \varepsilon_{\text{eff}})\rho_s h_s + \varepsilon_{\text{eff}}\rho h] + \nabla \cdot (\varepsilon_{\text{eff}}\rho U h) = \nabla \cdot q + \varepsilon_{\text{eff}}\tau \cdot \nabla U + \varepsilon_{\text{eff}} \frac{dp}{dt} - j_T \left( \frac{S}{V} \right)_{\text{eff}} \eta + \frac{|j \cdot j|}{\sigma} + \dot{S}_h \quad (2-7)$$

where  $h$  and  $h_s$  are the gas mixture enthalpy and solid phase enthalpy, respectively.  $\rho_s$  is the solid phase density,  $j_T$  is the transfer current density which will be discussed further in the section below,  $(S/V)_{\text{eff}}$  is a direct representation of catalyst loading,  $\eta$  is the overpotential between solid phase and electrolyte phase of the electrode, and  $\dot{S}_h$  is the enthalpy source due to phase change. The heat flux,  $q$ , is comprised of contributions due to thermal conduction and species diffusion without considering radiation effect, and is written as

$$q = \lambda \nabla T + \sum_{i=1}^{N_G} J_i h_i \quad (2-8)$$

where  $N_G$  is the total number of gas phase species in the system,  $h_i$  are their enthalpies defined as sum of the enthalpy of formation and sensitive enthalpy,

and  $J_i$  is the diffusion flux of species  $i$ . The thermal conductivity,  $k_{\text{eff}}$ , of the porous medium is an effective thermal conductivity of the pores and solid combined region and is expressed as

$$k_{\text{eff}} = -2k_s + \frac{1}{\frac{\varepsilon_{\text{eff}}}{2k_s + k_f} + \frac{1 - \varepsilon_{\text{eff}}}{3k_s}} \quad (2-9)$$

where  $k_s$  and  $k_f$  are the thermal conductivities of the solid and fluid regions, respectively. The second term of on the right hand side (RHS) of Eq. (2-7) is the effect of viscous dissipation, the third term on the RHS is the work done by pressure, the last three terms in Eq. (2-7) represent electrical work, Joule heating and energy interactions due to phase change. The irreversible losses due to reaction (conversion of chemical energy to heat) manifest through the last term on the right hand side of Eq. (2-8) because the definition of enthalpy includes both the enthalpy of formation as well as sensitive enthalpy. Mix kinetic theory is also chosen for calculating the thermal conductivity across the whole domain. The data for evaluating the thermal conductivity is available from [33]. Mix Jannaf method is applied for calculating the specific heat and estimated as form:

$$\frac{C_p}{R} = a_0 + a_1 T + a_2 T^2 + a_3 T^3 + a_4 T^4 \quad (2-10)$$

where  $R$  is the value that the universal constant divided by each species' molecular weight, and  $a_0, a_1, a_2, a_3$  and  $a_4$  are constant vary with species kind.

### 2.3.3 Species Equation

The species conservation equation is estimated as form:

$$\frac{\partial}{\partial t} (\varepsilon_{\text{eff}} \rho Y_i) + \nabla \cdot (\varepsilon_{\text{eff}} \rho U Y_i) = \nabla \cdot J_i + \dot{\omega}_i \quad (2-11)$$

where  $Y_i$  are the mass fraction of  $i$ -th species,  $J_i$  are the mass diffusion flux of species  $i$  and  $\dot{\omega}_i$  are the mass production/destruction rates of  $i$ -th species in the gas phase. The species mass diffusion rate is expressed as

$$J_i = \rho D_i \nabla Y_i + \frac{\rho Y_i}{M} D_i \nabla M - \rho Y_i \sum_j D_j \nabla Y_j - \rho Y_i \frac{\Delta M}{M} \sum_j D_j Y_j \quad (2-12)$$

the first term represents Fickian diffusion due to concentration gradients, and the other three terms are correction terms necessary to satisfy the Stefan-Maxwell equations for multicomponent species study. In this case,  $D_i$  are the effective diffusion coefficient of species  $i$  within porous medium, and depend on the porosity and tortuosity,  $\tau$ , of the medium

$$D_{\text{eff}} = \varepsilon_{\text{eff}} \tau D \quad (2-13)$$

where the value of tortuosity is usually 1.5 in Eq. (2-13), resulting in the so-called Bruggeman model [11].

The volumetric production/destruction rate of a species  $i$ ,  $\dot{\omega}_i$ , due to heterogeneous surface reaction is treated by performing a diffusion flux at the interface of the GDL and catalysts, and is obtained from the surface flux in discrete form expressed as

$$\dot{\omega}_i = \rho D_i \frac{Y_i - Y_{p,i}}{\delta} \left( \frac{S}{V} \right)_{\text{eff}} \quad (2-14)$$

where  $Y_i$  denotes the mass fraction at the interface of GDL and catalyst layer, while  $Y_{p,i}$  denotes the species mass fraction in the catalyst layer and  $\delta$  is the diffusion length scale. Usually, the diffusion length scale cannot be obtained from grid in the case of porous media, because the region under consideration is already much smaller than the size of a control volume. Typically, the diffusion length scale varies locally from primary pores to secondary pores. With the consideration of continuum mechanism, Knudsen



effect is neglected in tiny pore region, and the diffusion length scale is assumed to be equal to the average pore size in this case.

However, in the case of electrochemical reactions, the volumetric production/destruction rate of a given species is expressed as

$$\dot{\omega}_i = (a_i^P - a_i^R) \frac{j_T}{F} \quad (2-15)$$

where  $a_i^P$  and  $a_i^R$  are the stoichiometric coefficients of the products and reactants, respectively.  $F$  is the Faraday constant. Therefore, reaction-diffusion balance is necessarily required to be written as

$$\rho D_i \frac{Y_i - Y_{P,i}}{\delta} \left( \frac{S}{V} \right)_{\text{eff}} = (a_i^P - a_i^R) \frac{j_T}{F} \quad (2-16)$$

Eq. (2-16) clearly states that the reactants/products flowing through the interface where chemical reaction takes place by diffusion is equal to the volumetric production/destruction rate of a specific species from chemical reaction.

Maxwell-Stefan Model is applied for multi-species diffusion when over and above three species are involved in a diffusion process. At low density, multi-component gas diffusion can be approximated by the Maxwell-Stefan equation:

$$\frac{dx_i}{dz} = RT \sum_{j \neq i}^{N_G} \frac{x_i J_j - x_j J_i}{\rho D_{ij}} \quad (2-17)$$

### 2.3.4 Electrochemical Reaction

At the electrode catalyst layers, current is supplied from electrochemical reactions that reactant species participate at anode and cathode. Hydrogen is oxidized at the anode and oxygen is reduced at the cathode. These two reactions are driven by the potential difference between the solid phase and electrolyte phase, called the activation overpotential. The Butler-Volmer

equation describes this phenomenon and is expressed as

$$j_{T,j} = \frac{j_{0,j}}{\prod_{k=1}^N [\Lambda_{k,ref}]^{\alpha_{k,j}}} \left[ \exp\left(\frac{\alpha_{a,j}F}{RT} \eta\right) - \exp\left(-\frac{\alpha_{c,j}F}{RT} \eta\right) \right] \times \prod_{k=1}^N [\Lambda_k]^{\alpha_{k,j}} \quad (2-18)$$

where  $\alpha_{a,j}$  and  $\alpha_{c,j}$  are kinetic constants determined from experimentally generated Tafel plots,  $\alpha_{k,j}$  are the concentration exponents of the k-th species for the j-th step.  $[\Lambda_k]$  represents the average interfacial molar concentration of the k-th species, and the subscript ref refers to concentration values at the reference state at which the reference current density is prescribed. The electrode potential,  $\eta$ , is the potential difference between the solid phase ( $\Phi_S$ ) and the ionic phase ( $\Phi_F$ ) of the electrode.

The term  $j_{0,j}$  in Eq. (2-18) is the reference current density with units of  $A/m^3$ . As a matter of fact, the reference current density at the cathode is several orders of magnitude smaller than the value at the anode. Both the reference current densities at anode and cathode are expressed as [34]

$$\text{Anode: } j_0 = 1 \times 10^9 \quad (2-19)$$

$$\text{Cathode: } j_0 = 3 \times 10^5 \exp[0.014189(T-353)] \quad (2-20)$$

### 2.3.5 Current Equation

The continuity equation of current in any material leads to:

$$\nabla \cdot \mathbf{i} = 0 \quad (2-21)$$

where  $\mathbf{i}$  is the current density vector. When the material is a porous electrode, the current density is split into two parts: one flowing through the polymer electrolyte (ionic phase) denoted as  $i_F$  and the other flowing through the solid parts (electronic phase) of the porous matrix denoted as  $i_S$ . Fig. 2.3 simply shows the transfer of current within porous media. Eq. (2-18) can be written as

$$\nabla \cdot \mathbf{i}_F + \nabla \cdot \mathbf{i}_S = 0 \quad (2-22)$$

During the electrochemical reactions, electrons are either transferred from ionic phase to solid phase or vice versa shown in figure 2.3. Thus, Eq. (2-19) can be rewritten as

$$-\nabla \cdot \mathbf{i}_F = \nabla \cdot \mathbf{i}_S = j_T \left( \frac{S}{V} \right)_{\text{eff}} \quad (2-23)$$

It is generally assumed that each phase has its own electrical potential. In the ionic phase, the electrical current is denoted as electrolytic term while the current is denoted as electronic term in solid phase. Chemical reaction can only occur at the interface of electrolyte and solid when there's interaction between these two current components. Under this assumption, application of ohm's law to Eq. (2-23) yields

$$\nabla \cdot (\sigma_F \nabla \Phi_F) = -\nabla \cdot (\sigma_S \nabla \Phi_S) = j_T \left( \frac{S}{V} \right)_{\text{eff}} \quad (2-24)$$

where  $\Phi_S$  and  $\Phi_F$  are the electrical potentials of the ionic and solid phases, respectively.

### 2.3.6 Liquid Water Transport

The foundation of this two-phase model is an additional governing equation for the transport and formation of liquid water, given by

$$\begin{aligned} \frac{\partial}{\partial t} (\varepsilon_d \rho_l s) + \nabla \cdot (\varepsilon_d \rho U_l \zeta) + \nabla \cdot \left( \frac{\alpha M_l}{F} \mathbf{i}_F \right) = \\ \nabla \cdot (\varepsilon_d \rho_l D_\lambda \nabla_s) - \nabla \cdot \left( \frac{\zeta(1-\zeta)\kappa(\rho_l - \rho_g)}{v} \mathbf{g} \right) + \dot{m}_l \end{aligned} \quad (2-25)$$

where  $s$  is the saturation of liquid water, and is defined as the ratio of liquid volume to the volume of pores.  $\rho_l$  is the density of liquid water and  $\zeta$  is the relative mobility of liquid water.  $\varepsilon_d$  is the dry porosity which represents the porosity of the medium in the dry state. In this model where liquid water effect

is considered, pores in porous media are occupied by liquid, and the value of effective porosity decreases as the amount of liquid water in the medium increases. Therefore,  $\epsilon_{\text{eff}}$  has the form

$$\epsilon_{\text{eff}} = \epsilon_d(1 - s) \quad (2-26)$$

The first term in Eq. (2-25) represents the storage of liquid water in a certain domain. And the second term represents transport of liquid water by pressure-driven advection.

Membrane water content,  $\lambda$ , is given as the ratio of the number of water molecules to the number of charge ( $\text{SO}_3^-\text{H}^+$ ) sites. It shows how intense the electrochemical reaction is, and dictates the electrical conductivity of membrane. The value of membrane water content is determined by the activity of water vapor at the catalyst/membrane interface. The activity in the water phase,  $a$ , is  $x_w P/P_{\text{sat}}$ .  $x_w$  is the mole fraction of water vapor and the saturation pressure of water is denoted by  $P_{\text{sat}}$  in units of atm, which can be computed from the curve-fitted expressions provided by Springer et al. [5]

$$\log_{10} P_{\text{sat}} = -2.1794 + 0.02953T - 9.1837 \cdot 10^{-5} T^2 + 1.4454 \cdot 10^{-7} T^3 \quad (2-27)$$

Membrane water content is function of water activity for the Nafion 117 membrane by weighing membranes equilibrated above aqueous solutions of various lithium chloride concentrations, and the experimental relationship of water content versus water activity,  $a$ , used in this model is

$$\lambda = \begin{cases} 0.043 + 17.18a - 39.85a^2 + 36.0a^3 & 0 < a \leq 1 \\ 14 + 1.4(a - 1) & 1 < a \leq 3 \\ 16.8 & 3 < a \end{cases} \quad (2-28)$$

Eq. (2-28) is employed to calculate the value of  $\lambda$  based on solution of water vapor outside the membrane domain.

When water profile in the membrane has been determined, the membrane electrical resistance and the potential drop across it can easily be obtained. The electrical conductivity of Nafion 117 was proposed by Springer et al. [5], and is given by

$$\begin{aligned}\sigma_{303K} &= 0.005193\lambda - 0.00326 & \lambda > 1 \\ \sigma(T) &= \sigma_{303K} \exp\left[1268\left(\frac{1}{303} - \frac{1}{273 + T}\right)\right]\end{aligned}\quad (2-29)$$

Once the value of water content drops less than one, the membrane conductivity is assumed to be constant.

In a PEMFC, electro-osmotic water drag moves liquid water from anode to cathode. As this water built up at cathode, back diffusion occurs, resulting in the transport of water from cathode back to anode. This phenomenon is strongly dominated by capillary diffusivity. Capillary diffusivity depends on factors like the contact angle and saturation, and can be written in terms of the capillary pressure head as

$$D_{\lambda} = -\frac{\kappa_l}{\mu_l} \frac{dp_c}{ds} \quad (2-30)$$

where  $p_c$  is the capillary pressure head,  $\kappa_l$  is the permeability of the liquid and  $\mu_l$  is the dynamic viscosity of the liquid. Based on the correlation that Springer et al. [5] proposed, capillary diffusivity is function of water content and temperature, and is expressed as [5]

$$D_{\lambda}' = \begin{cases} \lambda / 4 & \lambda \leq 2 \\ 0.5 + 3.25(\lambda - 2) / 4 & \lambda \leq 6 \\ 3.75 + 4(\lambda - 26) / 15 & \text{otherwise} \end{cases} \quad (2-31)$$

$$D_{\lambda}(303K) = 10^{-10} \frac{\lambda}{(1 + s\lambda^2)a(17.81 - 79.7a + 108a^2)D_{\lambda}'} \quad (2-32)$$

$$D_{\lambda} = D_{\lambda}(303\text{K}) \exp\left[2416\left(\frac{1}{303} - \frac{1}{T}\right)\right] \quad (2-33)$$

In Eq. (2-32),  $s$  is considered as a constant with value of 0.0126.

### 2.3.7 Concentration Loss

During the electrochemical reaction, performance drops when reactant species concentrations are deficient on the reaction surfaces, especially when operating a PEMFC at low operating voltage due to high formation of water that causes clogging. The total concentration loss is expressed as

$$\eta_{\text{con}}^{\text{tot}} = \frac{RT}{2F} \left(1 + \frac{1}{\alpha}\right) \ln \frac{c_{\text{C}}^{\text{R}}}{c_{\text{L}}^{\text{R}}} \quad (2-34)$$

where  $c_{\text{C}}^{\text{R}}$  is the reactant molar concentration in flow channels,  $c_{\text{L}}^{\text{R}}$  is the reactant molar concentration in catalyst layers and  $\alpha$  is the mass transfer coefficient expressing how variations in electrical potential across reaction interfaces changes the reaction rate. The value of  $\alpha$  depends on the reaction and electrode material.

One of concentration loss is due to reactant species depletion in the catalyst layers called Nerst potential changes, and it has the form

$$\eta_{\text{con}}^{\text{N}} = \frac{RT}{2F} \ln \frac{c_{\text{C}}^{\text{R}}}{c_{\text{L}}^{\text{R}}} \quad (2-35)$$

The second way that concentration contributes to concentration loss is due to reaction kinetics, and it has the form

$$\eta_{\text{con}}^{\text{K}} = \frac{RT}{2\alpha F} \ln \frac{c_{\text{C}}^{\text{R}}}{c_{\text{L}}^{\text{R}}} \quad (2-36)$$

Different bend angles and widths of a channel lead to different minor losses; therefore, fluid velocity through bend decreases. Figure 2.4 illustrates a schematic of the PEMFC mass transport model, indicating that the reactant

concentration on the reaction surface is dominated by fluid velocity in the flow channel. The correlation between gas velocity in the flow channel and gas density on reaction surfaces is expressed as [3]

$$\rho_{B,L} = \rho_{A,C} - M \frac{j}{2F} \left[ \frac{H_C}{Sh \cdot D} + \frac{H_G}{D_{eff}} + \frac{B-A}{u_{in} H_G} \right] \quad (2-37)$$

where  $H_C$  is the height of the flow channel,  $H_E$  is the height of the GDL,  $Sh$  is the Sherwood number. According to the Eq. (2-37), the geometry of flow patterns is one of the parameters that dictate the performance of PEMFC. Hence, high performance can be achieved from flow pattern design.

## 2.4 Boundary Conditions

The governing equations for the current PEMFC model are elliptic, partial differential equations. Hence, boundary conditions are required for all boundaries in the computational domain.

The boundary conditions are presented as follows:

Anodic inlet of the channel:

$$u=u_{in}, T=T_{operating}, Y= Y_{H_2}+ Y_{H_2O}=1, j=0 \quad (2-38)$$

Anodic outlet of the channel:

$$P=P_{atm}, j=0 \quad (2-39)$$

Cathodic inlet of the channel:

$$u=u_{in}, T=T_{operating}, Y= Y_{O_2}+Y_{H_2O}=1, j=0 \quad (2-40)$$

Cathodic outlet of the channel:

$$P=P_{atm}, j=0 \quad (2-41)$$

Outer surface of bipolar plate at Anode:

$$T=T_{operating}, V=0 \quad (2-42)$$

Outer surface of bipolar plate at Cathode:

$$T=T_{\text{operating}}, V=\eta_{\text{tot}}=V_{\text{re}}+V_{\text{cell}} \quad (2-43)$$

where  $\eta_{\text{tot}}$  is the total overpotential and  $V_{\text{re}}$  is the reversible voltage given by reference [33]:

$$V_{\text{re}}=0.2329+0.0025T \quad (2-44)$$

Walls:

$$T=T_{\text{operating}}, j=0 \quad (2-45)$$





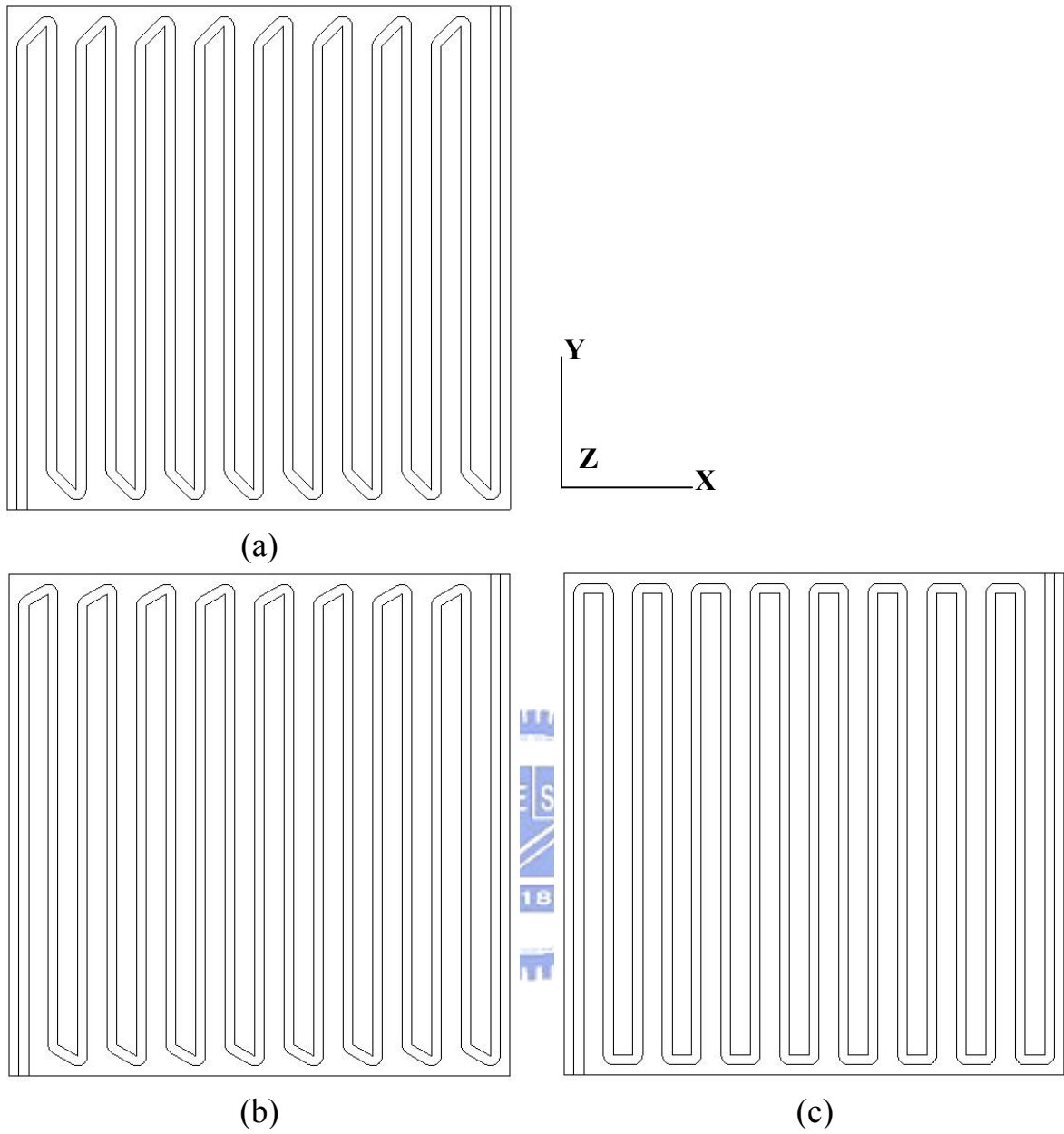


Fig. 2.1 Flow field pattern in PEMFC (a) 45-135; (b) 60-120; (c) 90-90, respectively.

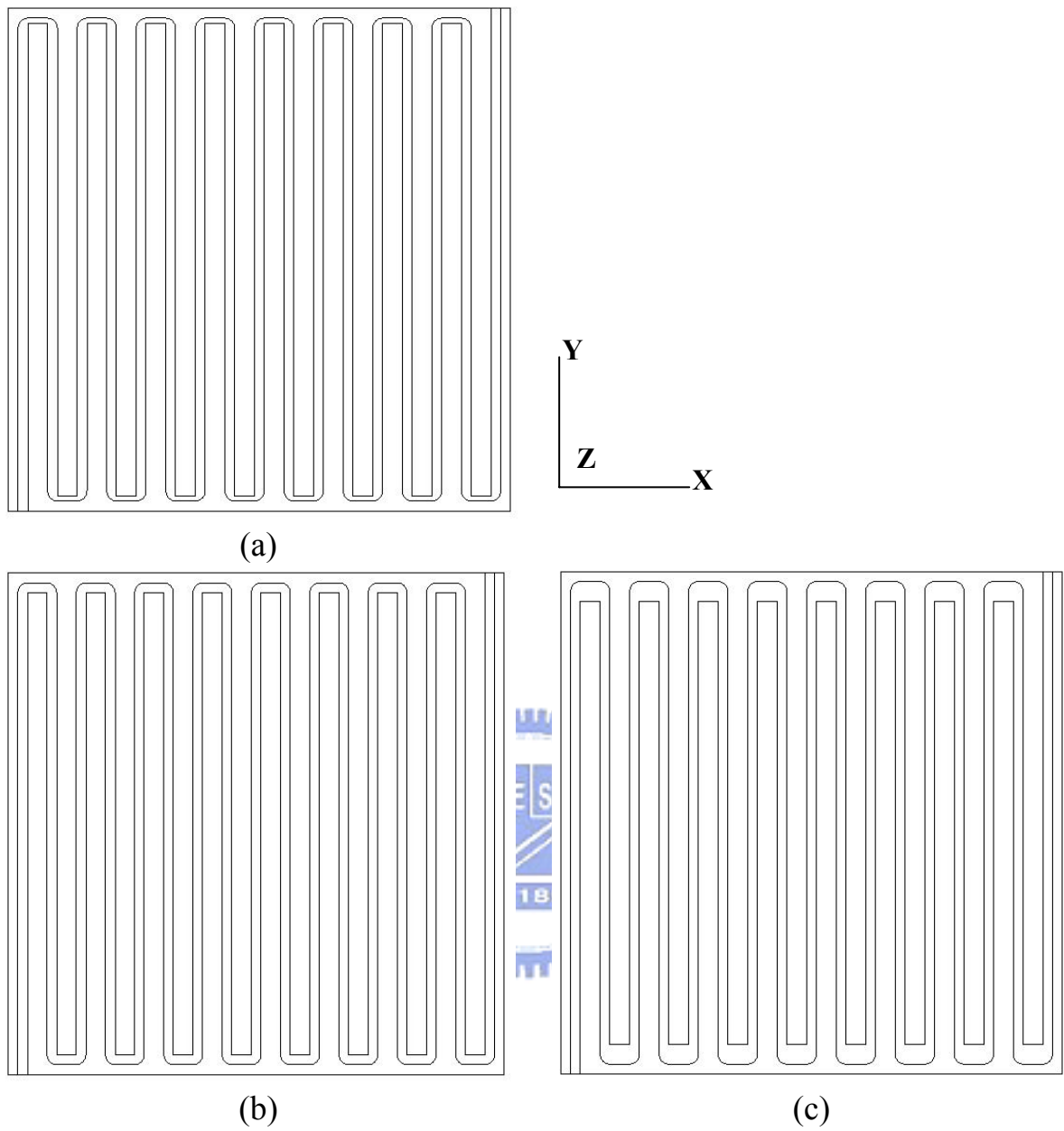


Fig. 2.2 Flow field pattern in PEMFC (a) 1007; (b) 1010; (c) 1020, respectively.

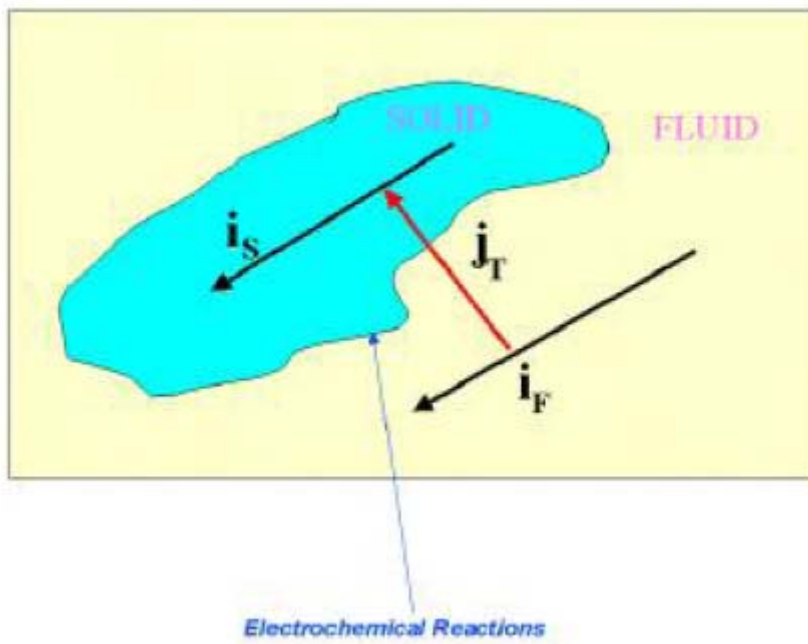


Fig. 2.3 Schematic of electrochemical reaction and the transfer current within a porous catalyst-containing conductor [33].



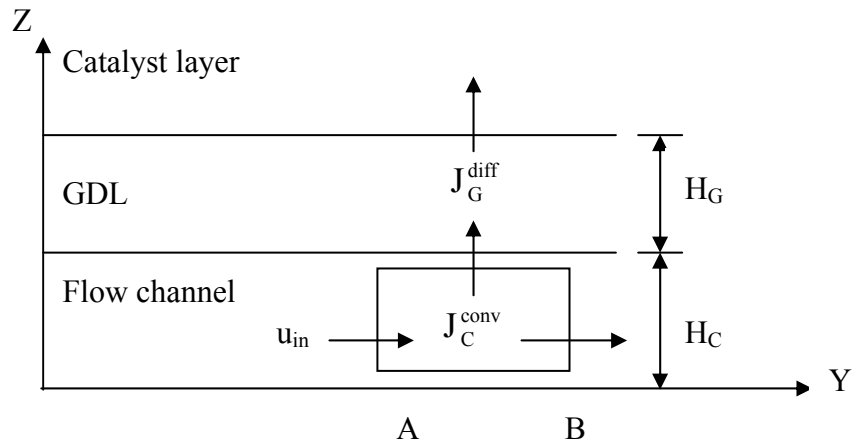


Fig. 2. 4 Schematic of the PEMFC mass transport model [3].



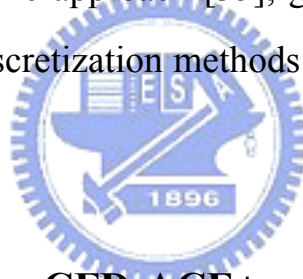
# Chapter 3

## Numerical Methods

### 3.1 Introduction to CFD-ACE+ software

CFD-ACE+ is a set of computer applications for multi-physics computational analyses. The programs provide integrated geometry and grid generation software, a graphical user interface for preparing the model, a computational solver for performing the simulation, and an interactive visualization software for examining and analyzing the simulation results.

Based on the finite-volume approach [35], governing equations mentioned in chapter 2 are solved by discretization methods which will be described in the following sections.



### 3.2 Numerical Method for CFD-ACE+

The CFD-ACE+ employs the finite-volume method to discretize the partial differential equations and utilize SIMPLEC scheme to obtain the pressure and velocity fields by solving mass and momentum conservation equations. After that, use the pressure and velocity fields to substitute into the rest governing equations to have results calculated in sequence.

#### 3.2.1 Finite-volume method

The geometric center of the control volume denoted by P is referred to as the cell center. CFD-ACE+ employs a co-located cell-center variable arrangement that means that all dependent variables and material properties are stored at the cell center P. In other words, the average value of any quantity

within a control volume is given by its cell-center value.

The conservation equations illustrated in chapter 2 can be consisted of four terms which are the unsteady, the convection, the diffusion, and the source terms, respectively. The form of a generalized transport equation is expressed as

$$\frac{\partial \rho \phi}{\partial t} + \nabla \cdot (\rho \bar{U} \phi) = \nabla \cdot (D \nabla \phi) + S_{\phi} \quad (3-1)$$

where  $\phi$  is a specific variable to be solved,  $\rho$  the density,  $\bar{U}$  is the velocity vector,  $D$  is the diffusion coefficient, and  $S_{\phi}$  is the source term which contains all terms that can't be included in the previous terms.

Eq. (3-1) is also known as the generic conservation equation for quantity  $\phi$ . Integrating this equation over a control-volume cell, yields Eq. (3-2)

$$\int_{\forall} \frac{\partial \rho \phi}{\partial t} d\forall + \int_{\forall} \nabla \cdot (\rho \bar{U} \phi) d\forall = \int_{\forall} \nabla \cdot (D \nabla \phi) d\forall + \int_{\forall} S_{\phi} d\forall \quad (3-2)$$

where  $\forall$  represents the volume. According to the Divergence theorem of Gauss, Eq. (3-2) can be further written as

$$\int_{\forall} \frac{\partial \rho \phi}{\partial t} d\forall + \oint_A (\rho \bar{U} \phi) \cdot \bar{n} dA = \oint_A (D \nabla \phi) \cdot \bar{n} dA + \int_{\forall} S_{\phi} d\forall \quad (3-3)$$

where  $A$  represents each surface of the control volume  $P$ .

The discretized equation can be expressed as

$$\frac{(\rho \phi \forall)^n - (\rho \phi \forall)^{n+1}}{\Delta t} + \sum_P (\rho \phi V)_P A_P = \sum_P (D \frac{\Delta \phi_{\perp}}{\delta_{\perp}}) A_P + (S_U + S_P \phi_P) \forall \quad (3-4)$$

With assembly of transient, convection, diffusion and source terms from numerical integration, governing equations are resulted in the following linear equation.

$$a_P \phi_P = \sum_{nb} a_{nb} \phi_{nb} + S_U + S_P \phi_P + a_P I \phi_P^* \quad (3-5)$$

where  $\phi_p^*$  is the previous value from last iteration, the subscript P denotes the value of dependent variable that represent the control volume P, I is inertial relaxation factor, and  $a_{nb}$  are known as the link coefficients. In general, both  $S_P$  and  $S_U$  represent the source term linearized and can be function of  $\phi$ . They are evaluated using the latest available value of  $\phi$ , which is the value at the end of previous iteration. The neighboring-cell term is dominated by the kind of spatial difference scheme.

The integral conservation Eq. (3-2) is applied to each control volume contained in the computational domain, so is Eq. (3-5). Eq. (3-5), the finite difference equation (FDE), is the discrete equivalent of the continuous flow transport equation we discussed before. And the FDE is considered linear by evaluating the  $a_{nb}$  with the values of  $\phi$  from the end of previous iteration.

### 3.2.2 SIMPLEC scheme

Solutions of the three momentum equations yield the three Cartesian components of velocity. Even though pressure is an important flow variable. No governing PDE for pressure is presented. Pressure-based methods utilize the continuity equation to formulate an equation for pressure, and that's what SIMPLEC is for.

SIMPLEC stands for Semi-Implicit Method for Pressure-Linked Equations Consistent, and is an enhancement to the well-known SIMPLE algorithm. In SIMPLEC, originally proposed by Van Doormal and Raithby [36], an equation for pressure-correction is derived from the continuity equation.

The finite-difference form of the x-momentum equation can be written as

$$a_P u_P = \left( \sum_{nb} a_{nb} u_{nb} + S_U \right)_P - \left( \sum_e p_e A_{x,e} \right)_P \quad (3-6)$$

where  $e$  denotes the value is dependent on the flow direction. The pressure field should be provided to solve for  $u$ . If the preceding equation is solved with a guessed pressure  $P^*$ , it will yield  $x$ -component velocity  $u^*$  which satisfies the following equation

$$a_p u_p^* = \left( \sum_{nb} a_{nb} u_{nb}^* + S_U \right)_p - \left( \sum_e p_e^* A_{x,e} \right)_p \quad (3-7)$$

Nevertheless,  $u^*$  won't generally satisfy continuity. The strategy is to find corrections to  $u^*$  and  $P^*$  so that an improved solution can be obtained. Consider  $u'$  and  $P'$  as the correction terms

$$u = u^* + u' \quad (3-8)$$

$$P = P^* + P' \quad (3-9)$$

An expression for  $u'_p$  can be obtained by subtracting Eq. (3-6) from Eq. (3-5)

$$a_p u'_p = \left( \sum_{nb} a_{nb} u'_{nb} \right)_p - \left( \sum_e p'_e A_{x,e} \right)_p \quad (3-10)$$

For pursuing incrementally more accurate solutions, approximation for  $u'_p$  is given as

$$u'_p = \left( \sum_e p'_e A_{x,e} \right)_p dp \quad (3-11)$$

where  $dp$  is expressed as

$$dp = \frac{-1}{a_p - \sum a_{nb}} \quad (3-12)$$

Moreover, an expression for  $u'_e$ , the velocity correction at the face, is obtained by averaging from the cell-centre values and of the form



$$u'_e = \gamma_e u'_p + (1 - \gamma_e) u'_E \quad (3-13)$$

where  $\gamma$  is the geometrical weighting function at surface  $e$  and  $u'_E$  is the neighboring-cell value. Besides, the continuity equation is written in discretization as

$$\frac{\rho \nabla - \rho^0 \nabla^0}{\Delta t} + \sum_e C_e = \dot{m} \nabla \quad (3-14)$$

where  $C_e$  is the mass flux and written as correction form

$$C_e = C_e^* + C'_e \quad (3-15)$$

Therefore, Eq. (3-13) can be recast as:

$$\frac{\rho'_p \nabla}{\Delta t} + \sum_e C'_e = S_m \quad (3-16)$$

where  $S_m$  represents the mass source in a control volume:

$$S_m = \left( \frac{\rho_p^0 \nabla^0 - \rho_p^* \nabla}{\Delta t} \right) + \dot{m} \nabla - \sum_e C_e^* \quad (3-17)$$

From Eq. (3-14), the correction term of mass flux is written as

$$C'_e = (\rho^* V'_n A)_e + (\rho' V_n^* A)_e \quad (3-18)$$

In consideration of incompressible flow such as current situation,  $\rho'$  is zero which means that no correction term is referred to density. In the case that the ideal gas assumption is considered, an equation of state is used to estimate the first-order partial derivative of density with respect to pressure, and is written as followings:

$$\frac{\partial \rho}{\partial P} = \frac{1}{RT} \quad (3-19)$$

The correction to face-normal velocity is obtained as:

$$V'_{n,e} = u'_{x,e} + v'_{y,e} + w'_{z,e} \quad (3-20)$$

With the face-normal velocity correction and the density correction thus expressed in terms of pressure correction, a pressure correction equation can be obtained from Eq. (3-15):

$$a_p p'_p = \sum_{nb} a_{nb} p'_{nb} + S_m \quad (3-21)$$

The sequence of operation for SIMPLEC scheme is summarized as follows:

1. Guess the pressure field  $p^*$ .
2. Solve the discretized momentum equations to obtain  $u^*$ ,  $v^*$  and  $w^*$ .
3. Evaluate  $C^*$  from  $\rho^*$  and  $u^*$ , using the procedure outlined before.
4. Evaluate mass source term.
5. Obtain  $p'$  by solving Eq. (3-20).
6. Use  $p'$  to correct the pressure and velocity fields using Eq. (3-8) and (3-9).
7. Solve the discretized equations for other flow variables such as enthalpy, species etc.
8. Repeat the procedure from step 2 until convergence is acquired.

### 3.3 Computational procedure of PEMFC simulation

The model presented in this investigation was starting at the construction of structured grids by pre-processing software CFD-GEOM from CFD-ACE+. Fig. 3-1 shows the model with structured grids. After the grids were built, the model was submitted to the solver, CFD-ACE-GUI, for properties and conditions assignments, simulation running included. The model was sequentially assigned to post-processing software called CFD-View for results visualization and extraction.

CFD-ACE+ uses an iterative, segregated solution method wherein the

equation sets for each variable are solved sequentially and repeatedly until a converged solution is obtained. The overall procedure is shown in Fig. 3-2. At the each iteration, the program calculates residual for each variable, which is the sum of the absolute value of the residual for that variable at each computational node. And the calculation is regarded to be converged as each variable's normalized residual is less than  $10^{-4}$  [28].

Numerical calculations are performed on a Pentium Core™2 2.67GHz PC with 4G RAM. After a series of grid independent tests, whose results are listed in Table 3.1, the 729,375 grid system is adopted with a 0.878% error. **Detailed information of grid for different components is listed in Table 3.2.** In addition, for model validation, based on the reported operating conditions, Fig. 3.3 shows a good agreement between the predicted data of present model and the experimental results from Santaralli and Torchio [37].

Table 3.1 Grid independence test

Grid	Operating Voltage	Current density (A/cm <sup>2</sup> )	Relative error
641,850	0.4V	631.6254414	2.886%
729,375	0.4V	618.9385131	0.878%
1,503,534	0.4V	613.3949275	

Table 3.2 Grid for different components

Grid	Components				
	Bipolar Plates	Channels	GDLS	Catalyst Layers	Membrane
641,850	116,700	155,600	194,500	58,350	116,700
729,375	136,150	175,050	213,950	77,800	126,425
1,503,534	241,948	345,640	414,768	207,384	293,794

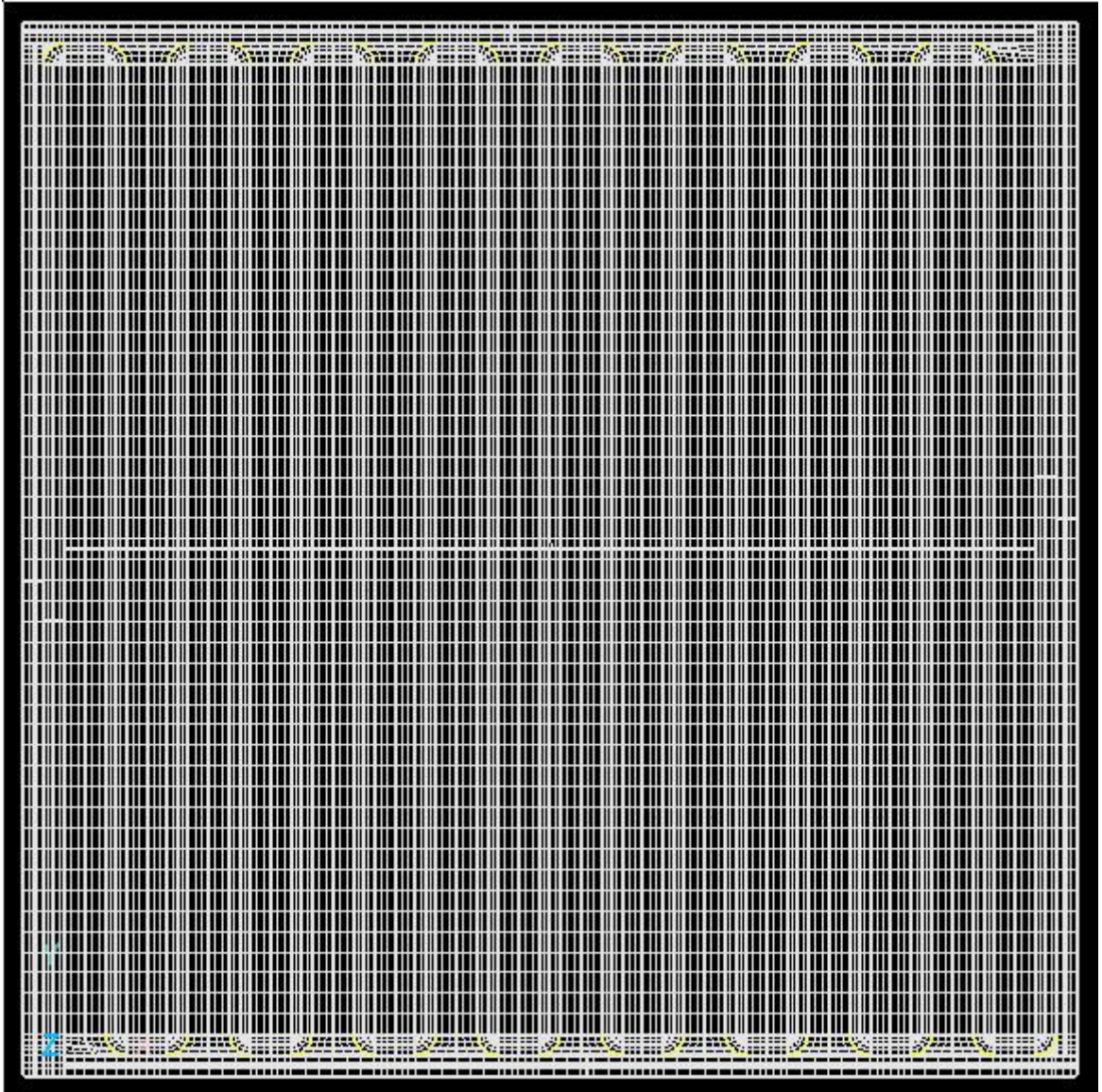


Fig. 3.1 Grid structure of current model.

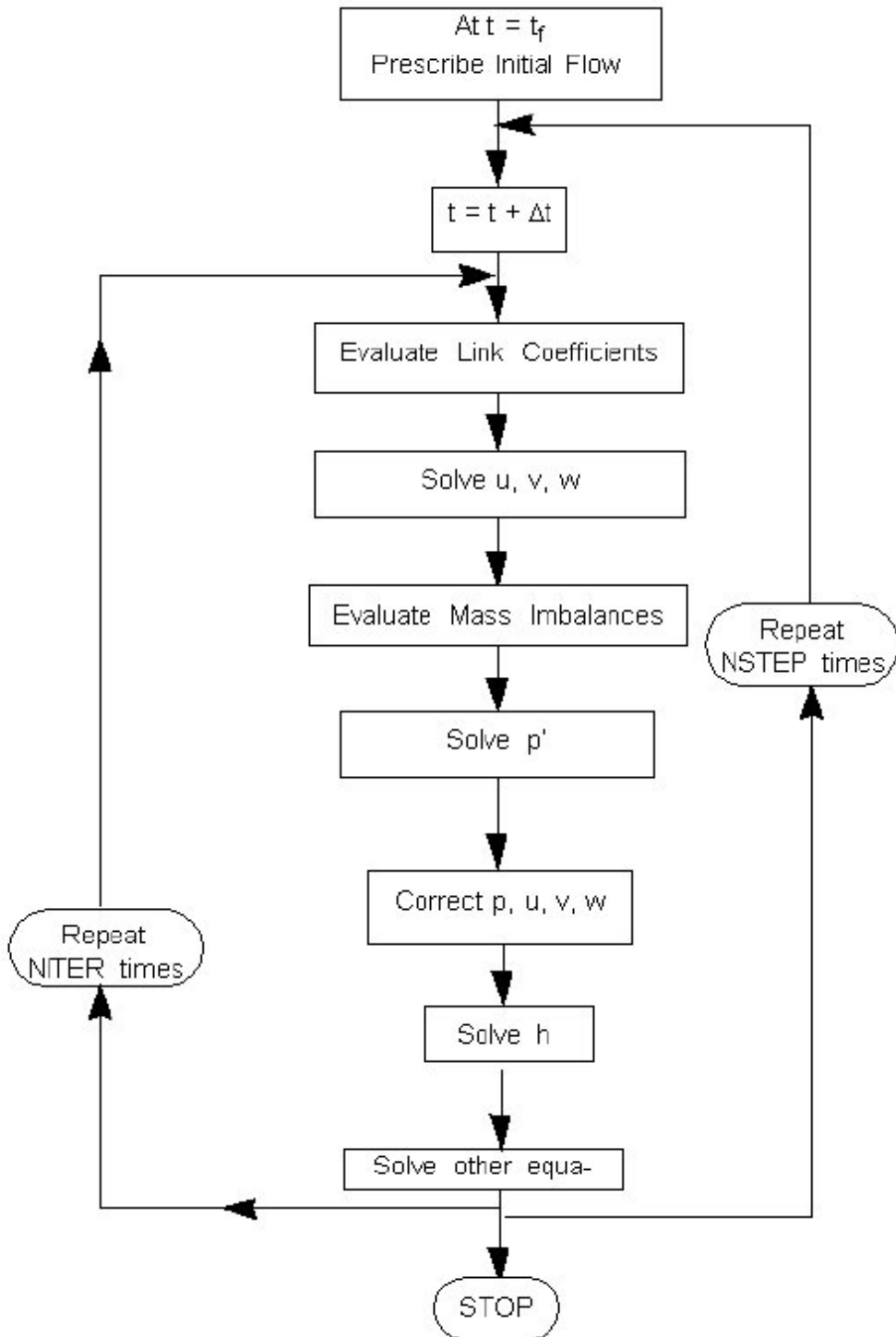


Fig. 3.2 Numerical flow chart of current study [33].

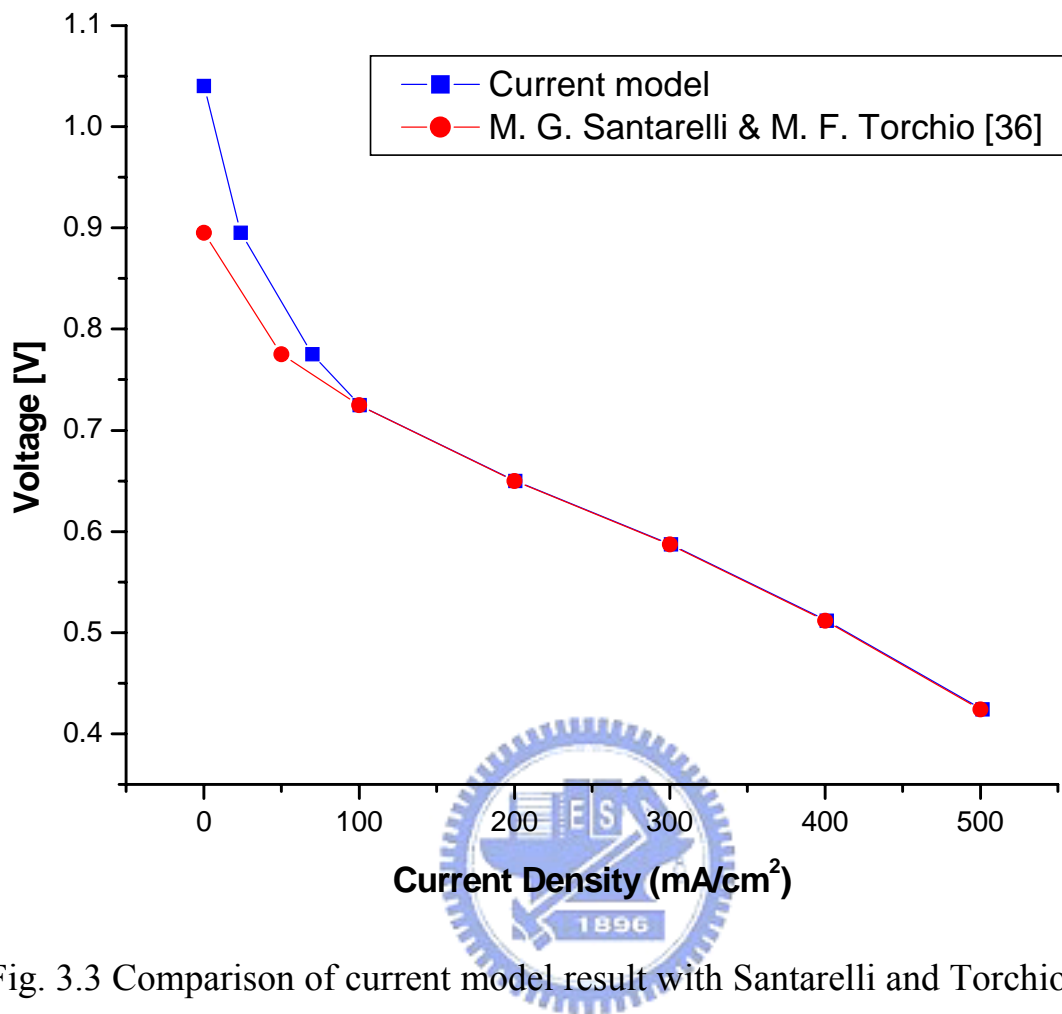


Fig. 3.3 Comparison of current model result with Santarelli and Torchio at 323K.

# Chapter 4

## Results and Discussion

In this chapter, the numerical results are presented. The effects of bend angle and width on the PEMFC performance at different operating temperatures are analyzed and discussed with the measurable dimensionless variable, Peclet number. Finally, the comparisons for several reactant species distributions are made. Since a series of parametric studies is carried out, a reference case, served as the comparison base, is chosen in advance. The reference case is selects as 90–90 flow pattern since it is the most common channel configuration studied in the majority of researches. The cell temperature is 353K because it can achieve the best performance. The other detailed operating conditions for this reference case are listed in Table 4.1.

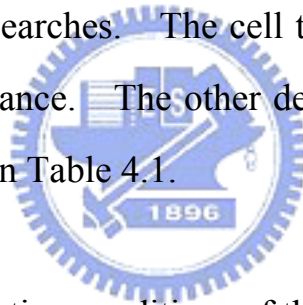


Table 4.1 Operating conditions of the reference case.

Parameter	Values
Reversible voltage	1.1154 (V)
Operating Temperature	353 (K)
Atmosphere Pressure	101.3 (kPa)
Outlet Pressure	101.3 (kPa)
Flow direction	Counter current
<b>Anode inlet conditions</b>	
Gas	H <sub>2</sub>
Relative humidity	100%
Mass fraction of H <sub>2</sub> /H <sub>2</sub> O	8.868/91.132
Temperature	353 (K)

Flow rate	796.08 (ml/min)
<b>Cathode inlet conditions</b>	
Cathode Gas	O <sub>2</sub>
Relative humidity	100%
Mass fraction of O <sub>2</sub> /H <sub>2</sub> O	60.89/39.11
Temperature	353 (K)
Flow rate	658.992 (ml/min)

#### 4.1 Fundamental Behaviors of Reference Case

The flow field, mass transfer and distributions of temperature and current density characteristics inside a PEMFC are analyzed in this section in order to obtain a basic understanding of how three-dimensional flow and transport phenomena influence the electrochemical process and investigate the interdependence between variables.

Figure 4.1 shows the polarization curve of the reference case. With cell temperature of 353K, the reversible voltage is set to be 1.1154V by the equation obtained from reference [33]. The corresponding output current densities are collected for every 0.1V for the operating voltage ranged from 0.4 to 1.0V. In the high operating voltage regime, the current density drops substantially due to activation losses. Activation overpotential caused by these losses represents the voltage sacrificed to overcome the activation barrier associated with the electrochemical reaction. In the middle of such curve where performance is dominated by ohmic losses, the current density increases linearly with the decrease of voltage because the ohmic overpotential is linearly proportional to the current production. Reactant gases depletion and products accumulation would adversely affect the performance at high current densities. Such voltage



drop is referred to concentration losses. However, performance in this case does not drop considerably around the end of this curve, indicating that liquid water does not contribute to the voltage drop that will be discussed later.

The mass diffusion, which is the main gas transport mechanism within porous media, is crucial to PEMFC performance since reactants must pass through GDL to reach catalyst layer for electrochemical reaction. However, in flow channels, insufficient mass convection may cause fuel depletion in downstream areas. Therefore, the performance improvement correlates closely with the mass diffusion and convection rate within the channels. In fluid dynamics, the Peclet number, a dimensionless group relating the rate of mass convection of a flow to its rate of mass diffusion, is defined as  $Pe = VL/D$ , where  $V$  is the flow velocity,  $L$  the characteristic length, and  $D$  the mass diffusivity. Therefore, flows with smaller Peclet number are having higher mass diffusion rate that is favorable for gas transport in porous media. Figure 4.2 shows the specified number for each bend entrance along anodic flow channel where the corresponding values of Peclet number are determined. The inverse of local Peclet number ( $Pe^{-1}$ ) in streamwise direction at each anodic bend entrance is shown in Fig. 4.3. It shows that the inverse of Peclet number ( $Pe^{-1}$ ) increases along the anodic channel from the inlet toward the outlet because of the decrease of gas velocity and the increase of gas temperature caused by the electrochemical reaction.  $Pe^{-1}$  at the first bend is 0.0113 and then increases to 0.0151 at the last bend, implying a significant enhancement of mass diffusion. With the increase of mass diffusion rate, local uniformity of variables would be improved in the downstream channel. For further analyses, the distributions of current density, velocity and other variables at operating voltage of 0.4 will be discussed below.

Figure 4.4 shows the distribution of current density in the membrane. It shows that the current density decreases slightly from anodic inlet toward the outlet, implying that the current density distribution is principally dictated by the hydrogen concentration rather than the oxygen's. This is because under fuel-rich supply, hydrogen becomes dominant due to considerably higher reference current density compared to oxygen. For reference case, the maximum current density is  $1050 \text{ mA/cm}^2$  located near the anodic inlet and minimum is  $502 \text{ mA/cm}^2$  occurred in the vicinity of anodic exit, and that presents a difference of  $548 \text{ mA/cm}^2$  in current density on global views. However, the local current variation occurred at the marginal rib with a value of  $185 \text{ mA/cm}^2$  is much larger than that at channels with a value of  $36 \text{ mA/cm}^2$ . It implies that there exists a higher non-uniformity current distribution at the rib. Also, the non-uniformity in local distribution appears to be significant near the first bend and becomes less non-uniform as the current density decreases along the channel. Moreover, the marginal region of the membrane, where large variation of current density is observed, non-uniformity of temperature and water content would exist correspondingly and that will be discussed later.

Figure 4.5 shows the distributions of velocity in both anodic and cathodic channels. In the anodic channel, it can be noticed generally that the velocity magnitude decreases slightly along their flow directions from inlet toward outlet due to the water back-diffusion. A close look at the figure reveals that the channels give rise to the additional minor losses due to the presence of secondary flows at the bending areas. The losses would cause energy dissipation within the cell. However, it is desirable for the mass transfer point of view for enhancement.

The change in the current density can cause local variation in the cell

temperature, and the distribution uniformity of temperature is important for minimizing the thermal stress on the membrane so that its lifetime would be extended. The temperature distributions at anodic and cathodic channels and in the membrane are shown in Fig. 4.6. The uniformity appears to be good at anodic and cathodic channels with the total variations of 1.5K and 2.2K, respectively, indicating that the local thermal stress is not significant. From the comparison of temperature variation at both channels, it indicates that the variation of temperature on the cathode is slightly higher than on the anode since cathode is the place where most heat is produced. As shown in Fig. 4.6(b), the overall temperature distribution in the membrane basically follows the current density distribution shown in Fig. 4.4. This is because heat production and current generation are positively correlated. However, a small discrepancy still exists at the marginal region, where temperature is relatively low but current density is considerably high. This is because the isothermal conditions are imposed on the energy equation rather than zero-flux conditions. This figure also shows that the temperature reaches 356K at the second, third and fourth channels, then, decrease slowly to the exit region. The good uniform distributions of reactant gases are important to the improvement of PEMFC performance, since they can effectively alleviate the flooding effect, leading to the high consumptions of reactant gases.

Figure 4.7 shows the distribution of hydrogen concentration on the interface between anodic GDL and catalyst layer. It shows that the hydrogen concentration increases along the flow direction, indicating that its concentration increases with decreasing current density. The concentration is maintained at 0.4 in the area above the first one third of the anodic channel, and slowly increases to 0.51 near the anodic exit region. Similar phenomenon also was

predicted by [38].

The distribution of oxygen concentration on the interface between cathodic GDL and catalyst layer is shown in Fig. 4.8. Unlike the hydrogen one, the oxygen concentration decreases along its flow direction with a highest value of 0.92 near the inlet region and the lowest one of 0.2 at the outlet region. From these results, it indicates that the property variations in the area above the cathodic channels are greater than that of anodic ones. From Figs. 4.4, 4.7 and 4.8, it indicates that the distribution of current density is inversely proportional to both the hydrogen and oxygen local concentrations.

Water generated in cathode catalyst layer may back-diffuse from cathode to anode, if the cathode is well-hydrated. However, protons moving from the anode to cathode would drag water with them, and this force is called electro-osmotic drag force. This phenomenon implies that, especially at high current densities, the electrolyte at the anode would become dried out—even if the cathode is fully hydrated. Therefore, a uniform distribution of water in both vapor and liquid states is necessary to maintain both the anode and cathode in well-humidified conditions. Figure 4.9(a) presents the distribution of water vapor on the interface between cathodic GDL and catalyst layer. It shows that the water vapor concentration increases positively with current density since both are the products of reaction, and the highest value of water vapor concentration, 0.8, is observed near the anodic inlet where local current density is high. Also, the lowest value of water vapor concentration, 0.1, is located in the last one third of the anodic channel. The flux of water vapor in the membrane from anode to cathode is shown in Fig. 4.9(b). Along the anodic channel, flux of water vapor from anode to cathode increases, implying that back-diffusion becomes insignificant in anodic downstream areas due to low

water vapor concentration. Therefore, it is noticed that in the anode, an amount of water is consumed by penetrating to the cathode due to osmotic drag, resulting a decrease of water vapor concentration. Correspondingly, hydrogen concentration increases from anodic inlet toward the outlet for species conservation.

The distribution of liquid water on the interface of cathodic GDL and catalyst layer is illustrated in Fig. 4.10. As mentioned earlier, saturation of liquid water is defined as a ratio of liquid volume to the pores' one. This figure shows that liquid water only occurs at the first rib on the left-hand side where the local current density is relatively high comparing to other areas. According to the results from reference [39], liquid water formulation is inversely proportional to the cell temperature, and, once the cell temperature is increased beyond 348K, most of the water vapor is removed out of the channels with the gas flow without liquid water formation and droplet accumulation. Therefore, only small amount of liquid water exists in the PEMFC as shown in Fig. 4.10. From the comparison of liquid water profile with the distributions of other variables, it shows no similarity between them, indicating that flooding effect is not significant within the cell.

Water content is given as the ratio of the number of water molecules to the one of charge ( $\text{SO}_3^-\text{H}^+$ ) sites. This ratio indicates how well the membrane is hydrated and is the key to reduce membrane electrical resistance. Water content also affects other membrane properties, such as water diffusivity and ion conductivity, thus influencing the performance. These imply that water content is the dominant factor in water management rather than the water vapor or liquid water. Therefore, maintaining a uniform distribution of membrane water

content can extend PEMFC lifetime because the uniformity can reduce the formation of local hot spots and flooding that stresses and damages the membrane electrode assembly (MEA). The distribution of water content in the membrane is shown in Fig. 4.11. Basically, the water content is decreasing from anodic inlet toward the outlet. This trend is consistent with the distributions of current density and temperature shown previously, indicating a strong positive correlation between these three variables. Water content near anodic inlet reaches the highest value of 6.3, then drops gradually to 2.2 near the sixth bend from the anodic inlet and maintains that value up to the anodic exit. With low water content, flooding effect and back diffusion are not as strong, suggesting that electro-osmotic force dominates over back diffusion in the membrane.

After a qualitative correlation is revealed between the distributions of current density, temperature and water content, Figure 4.12 shows the average values of temperature and water content in the membrane at each corresponding current density. The average temperature in the membrane is approximately equal to 353K when the current density is 24 mA/cm<sup>2</sup> since current production is small. Afterward the average temperature increases exponentially with the current density, and then reaches a maximum value of 356K corresponding to the maximum current density, 750 mA/cm<sup>2</sup>. The average value of water content is about 2.81 with current density of 24 mA/cm<sup>2</sup>, and 3.37 with current density of 750 mA/cm<sup>2</sup>. A slight decrease after current density increases beyond 620 mA/cm<sup>2</sup> is resulted from the electro-osmotic effect that leads to membrane dehydration. With a specified cell temperature of 353K, the increase of water content is considerably small due to low formulation of liquid water as discussed above.

From the analyses of fundamental behavior inside a PEMFC, it is discovered that there is a close and positive correlation between the distributions of current density, temperature and water content, and these distributions are mainly dictated by the hydrogen concentration. However, the distributions of reactant gases, hydrogen and oxygen, are inversely proportional to the current density. Moreover, flooding effect does not occur in the cell nor affect other variables distributions at a cell temperature of 353K. With the fundamental understanding, the effects of bend angle and width on PEMFC performance will be analyzed and discussed subsequently at the cell temperatures of 323K and 353K.

## 4.2 Effects of Bend Angle

Figure 4.13 shows the resultant polarization curves for three flow patterns (45–135, 60–120 and 90–90) with different bend angles at the conditions specified in Table 4.2. The first number in each flow pattern represents the first angle of the channels, and the second one represents the second angle. These two are combined to generate a complete U-turn flow channel. The reversible voltage is 1.0404V with cell temperature of 323K and 1.1154V with cell temperature of 353K that are obtained by the equation from reference [33]. As mentioned previously, the pattern of 90–90 is the most conventional one applied in most researches such that it is considered as the reference case.

Table 4.2 Operating conditions

Parameter	Value
Operating temperatures	323 and 353 (K)



Reversible voltages	1.0404 and 1.1154 (V)
Atmosphere pressure	101.3 (kPa)
Outlet pressure	101.3 (kPa)
Flow direction	Counter current
<b>Anode inlet conditions</b>	
Gas	H <sub>2</sub>
Relative humidity	100%
Temperature	323 and 353 (K)
Flow rate	796.08 (ml/min)
<b>Cathode inlet conditions</b>	
Gas	O <sub>2</sub>
Relative humidity	100%
Temperature	323 and 353 (K)
Flow rate	658.992 (ml/min)

From the comparison of polarization curves, it indicates that the performances are higher at 353K due to the enhanced reaction rates and the increase of reference current densities. The figure also shows that 60–120 pattern achieves the highest performance at low operating voltages ranged from 0.4V to 0.6V. Comparing to 90–90 pattern, this pattern's performance gives around 5% higher current density with cell temperature of 323K and around 4% higher with temperature of 353K at 0.4V. It is resulted from the higher Peclet number in the flow channel that will be discussed below. Note that the results show that the performance difference between 45–135 and 90–90 can be ignored because of only about 1% disagreement between these two patterns.

The inverse of local Peclet number ( $Pe^{-1}$ ) in streamwise direction at each anodic bend entrance is shown in Fig. 4.14. The operating voltage is 0.4V



because it can achieve the highest power density. This figure indicates that 60–120 pattern has higher mass diffusion rate compared to the ones of 45–135 and 90–90. Comparing to 90–90 pattern, this pattern gives around 3% higher value of  $Pe^{-1}$  in the bends from the third one to the tenth with cell temperature of 323K and around 2% higher from the third one to the eighth with the temperature of 353K. From the results of [40], the transition of transport mechanism from the diffusive regime to the forced one is situated around  $Pe^{-1}=0.04$ . In convection regime, the higher mass diffusion rate will thus intensify the electrochemical reaction. As the cell temperature is increased from 323K to 353K, the difference of  $Pe^{-1}$  between 60–120 and 90–90 patterns decreases, indicating that the influence of bend angle on flow mechanism decreases with an increase of cell temperature. However, at the locations near inlets and outlets,  $Pe^{-1}$ 's from different patterns are approximately equal because of the same boundary conditions. For further analyses, the distributions of current density, temperature and water content will be compared.

Figures 4.15 and 4.16 show the distributions of current density in the membrane at an operating voltage of 0.4V with cell temperatures of 323K and 353K, respectively. It can be seen that the current density decreases from anodic inlet toward anodic outlet due to the consumption of hydrogen as discussed before. These figures also indicate that 60–120 pattern has the considerably highest local current density at bending areas than those of other patterns at both cell temperatures, which result in the improvement of performance. With cell temperature of 323K, the variation of 45–135 is 663 mA/cm<sup>2</sup>, the one of 60–120 is 658 mA/cm<sup>2</sup>, and that of 90–90 is 645 mA/cm<sup>2</sup>. With temperature of 353K, the variation of 45–135 is 548 mA/cm<sup>2</sup>, the one of 60–120 is 514 mA/cm<sup>2</sup>, and that of 90–90 is 502 mA/cm<sup>2</sup>. Comparing to

90–90 flow pattern, even though 60–120 pattern achieves the highest performance, it does not effectively decrease the variation of current density as the change of bend angle.

Figures 4.17 and 4.18 show the distributions of temperature in the membrane. From Fig. 4.17, it indicates that the temperature reaches the highest value, 326K, in the area above the second anodic channel for all cases and then slowly decreases toward anodic outlet. Figure 4.18 shows that the temperature reaches the highest value, 356K, in the area above the second, third and fourth anodic channels, then, decrease slowly to the exit region. The simulations reveal that the three patterns have similar temperature distributions, implying that the change of bend angle does not significantly improve the temperature uniformity. This also indicates that there exists a limit to how much the improvement of temperature uniformity can be obtained from the change of bend angle.

Figure 4.19 shows the average temperature in the membrane as a function of the current density. It shows that the average temperature increases positively with the current density because of the increasing chemical reaction rate. The average temperature of 60–120 is comparatively higher than that of the other patterns, especially at the higher current densities, due to the higher performance. This figure also indicates that the difference between the average temperatures of 45–135 and 90–90 is very small with both cell temperatures that are consistent with their performances.

Figure 4.20 and 4.21 present the distributions of water content in the membrane. From the comparison of these two figures, it indicates that overall water content decreases as the operating temperature is increased from 323K to 353K because liquid water formation is inversely proportional to the cell

temperature as mentioned before. Both figures show that 45–135 and 90–90 patterns with different bend angles have similar water content distributions at the same cell temperature. With cell temperature of 323K, the local water content can reach around 9 near the area above the inlet region, then drops gradually toward the exit region. For the temperature of 353K, the local water content can only reach around 6 in the area above the marginal rib and drop to 4 at the one third of the anodic channel, then maintain this value through the exit region. Moreover, both Figs. 4.20 and 4.21 show high water content uniformity in the membrane with only about 5 for the variation that is beneficial for flooding prevention.

Figure 4.22 and 4.23 show the average water content in the membrane and the corresponding electrical resistance at each current density in this study. The figures reveal that all the three patterns have approximately equal water content under the same cell temperature since the difference between their performances are not great. Also, Fig. 4.22 shows that as current density increases, the membrane water content decreases with cell temperature of 323K. The decrease in water content at increasing current density is because of an increase in net proton flux that drags water from the anode to the cathode with increasing current density, and therefore, dehydration happens in the membrane. The intensified water transport from anode to cathode results in membrane dehydration because the hydration state of membrane is a stronger function of anode water activity rather than cathode one. However, with the cell temperature of 353K, the average water contents of the three patterns slowly increase with their current densities, indicating that water content is dictated by reaction intensity rather than proton flux within the membrane. It is resulted from insufficient liquid water formation when cell temperature goes beyond

348K that reduces the electro-osmotic drag force. Usually, the value of water content can reach as high as 22 when at water boiling temperature and current density of 2000 mA/cm<sup>2</sup> mentioned in reference [5]. However, in this study, the water content is much lower than 22 because the cell temperatures are below boiling point and the current density is comparatively lower than 2000 mA/cm<sup>2</sup>. With such small water content, flooding effect does not appear or cause a substantial voltage drop near the end of the polarization curves. Moreover, it is indicated that higher water content leads to lower membrane electrical resistance since the proton conductivity is proportional to the water content inside the membrane.

Figure 4.24 and 25 show the distributions of saturation on the interface between cathodic GDL and catalyst layer. Patterns with cell temperature of 323K are clearly having higher saturation level compared to the temperature of 353K, since the temperature below 348K is favorable for liquid water formation. Also, the first rib from the left is considered as dead-end zone where saturation level is high because of limited convection in the region. However, the distributions between different patterns are similar under the same operating temperature, since the flooding effect is not significant.

From above comparisons, it is noted that 60–120 pattern has the highest performance compared to 45–135 and 90–90 patterns due to the increase of mass diffusion rate. The local uniformities of current density, temperature and water content are improved incrementally along the anodic channel with the increase of mass diffusion rate. However, the improvement for the overall uniformity of current density distribution owing to the change of bend angle is limited. Also, the results between 45–135 and 90–90 are more or less similar for the performances and all variable distributions.

### 4.3 Effects of Bend Width

Figure 4.26 shows the polarization curves of the three flow patterns (1007, 90–90 and 1020) with different bend widths at the operating conditions specified in Table 4.3. The first two numbers, 10's, represent the channel width of 1 mm, and the last two numbers, 07 and 20, represent the bend width of 0.7 mm and 2.0 mm, respectively. Also, 90–90 pattern with both channel and bend of 1 mm, is considered as the reference case.

Table 4.3 Operating conditions

Parameter	Value
Operating temperatures	323 and 353 (K)
Reversible voltages	1.0404 and 1.1154 (V)
Atmosphere pressure	101.3 (kPa)
Outlet pressure	101.3 (kPa)
Flow direction	Counter current
<b>Anode inlet conditions</b>	
Gas	H <sub>2</sub>
Relative humidity	100%
Temperature	323 and 353 (K)
Flow rate	796.08 (ml/min)
<b>Cathode inlet conditions</b>	
Gas	O <sub>2</sub>
Relative humidity	100%
Temperature	323 and 353 (K)
Flow rate	658.992 (ml/min)

From the comparison of these polarization curves, it indicates that 1020

pattern achieves the highest performance ranged from 0.7V to 0.4V at both cell temperatures of 323K and 353K. Comparing to the 90–90, this pattern's performance gives around 6.1% higher current density with cell temperature of 323K and around 7.7% higher with the temperature of 353K at 0.4V. It is resulted from the higher Peclet number in the flow channel that will be discussed below. Additionally, the results show that 1007 and 90–90 patterns have similar performance because their differences are small that is less than 10 mA/cm<sup>2</sup> at 323K (0.4V) and 28 mA/cm<sup>2</sup> at 353K (0.4V).

The inverse of local Peclet number ( $Pe^{-1}$ ) in streamwise direction at each anodic bend entrance is shown in Fig. 4.27. The results indicate that 1020 pattern has a considerably higher mass diffusion rate compared to 1007 and 90–90, respectively, since there exist sudden expansions in the channel that sufficiently reduce mass convection rate, and therefore, relatively enhance mass diffusion rate. Comparing to 90–90, this pattern gives around 7.5% higher value of  $Pe^{-1}$  with cell temperature of 323K and around 11% higher with the temperature of 353K in all bends. The increase of mass diffusion rate will consequently intensify the electrochemical reaction and then result in performance improvement. As the cell temperature is increased from 323K to 353K, the difference in  $Pe^{-1}$  between 1020 pattern and the others increases, indicating that the influence of bend width is positively impacted by the increase of cell temperature. To further discuss the effect of bend width on PEMFC, the plots of variable distributions in membrane will be compared below.

Figures 4.28 and 4.29 show the distributions of current density in the membrane. The figures indicate that the 1020 pattern has a higher local current density than 1007 and 90-90, separately, especially with cell temperature of 353K. With cell temperature of 323K, 1007, 90–90 and 1020 flow patterns

have the variations in current densities of 648, 645 and 668 mA/cm<sup>2</sup>, the largest among the patterns,. With the temperature of 353K, the variation of 1007 is 514 mA/cm<sup>2</sup>, the one of 90–90 is 502 mA/cm<sup>2</sup>, and that of 1020 is 530 mA/cm<sup>2</sup>. From the comparison of current density variation, it indicates that the variation is neither reduced from the change of bend width, especially in the case with wider bend.

Figure 4.30 and 4.31 show the temperature distributions in the membrane. They show that 1020 pattern has considerably highest temperature compared to the others. By looking at the distributions in Fig. 4.30, it can be observed that the temperature reaches the highest value, 326K, in the area above the first anodic bend in the 1020 flow channel. The temperature then slowly decreases toward anodic outlet. Figure 4.31 reveals that the temperature reaches the highest value, 358K, in the area above the second anodic bend for all the patterns, then, decrease slowly to the exit region. The simulations also reveal that the 1007 and 90–90 patterns have similar temperature distributions, which consists with their performances. Though the performance of PEMFC is improved by the wider bend width, hot spots still exist in the membrane that is crucial to membrane lifetime, and this is consistent with the non-uniformity of current density distribution discussed previously.

Figure 4.32 shows the average temperatures in the membrane with cell temperatures of 323 and 353K. The figure reveals that 1020 pattern has the highest average temperature for all current densities. Also, as current density increases, the differences between 1020 and other patterns increase under both cell temperatures. This trend is consistent with the polarization curves. Additionally, there is an only small discrepancy in the average temperature of membrane between 1007 and 90–90 patterns since their performances are more



or less similar.

Figure 4.33 and 4.34 show the distributions of water content in the membrane. With cell temperature of 323K, higher water content occurs near the area above anodic inlet region with a value of 8 for all patterns. However, high water content occurs at the marginal rib with the value of 5.5 under cell temperature of 353K. Additionally, high water content uniformities are presented in both Figs. 4.33 and 4.34 with only about 3 for the variation, which can effectively alleviate mechanical stresses and water flooding effect.

Figures 4.35 and 4.36 present the curves of average water content in the membrane versus current density. For all patterns with cell temperature of 323K, when current density increases, the water content decreases because of the electro-osmotic effect as already shown in Fig.4.22. However, with the temperature of 353K, average water content slightly increases with the increase of current density. These phenomena apply to all configurations in this study. These figures show that average water contents from different patterns are all under 14, thus the flooding effect is insignificant for these flow patterns. The membrane at low currents maintains water content near 14 water molecules per charge site, and the electrical resistance approaches  $0.27 (\Omega \text{ cm}^2)$  with cell temperature of 323K. With the temperature of 353K, water content is maintained at 2.8 with the resistance around  $1.58 (\Omega \text{ cm}^2)$ .

Figure 4.36 and 4.37 show the distributions of saturation on the interface between cathodic GDL and catalyst layer. The figures indicate that the discrepancy only exists between different operating temperatures as discussed before. In addition, it also indicates that saturation level is high at the edges of GDL due to dead-end effect.

The effects of bend width have been discussed. The results reveal that



1020 pattern with wider bend has the highest performance compared to other patterns because of the enhanced mass diffusion rate. However, 90–90 pattern shows the lowest variation in current density and temperature that is beneficial for thermal stress reduction. Additionally, from the comparison of the polarization curves of 60–120 and 1020 flow patterns, it indicates that the performance is higher for the latter one, but with lower uniformities of current density and temperature existing in the membrane.



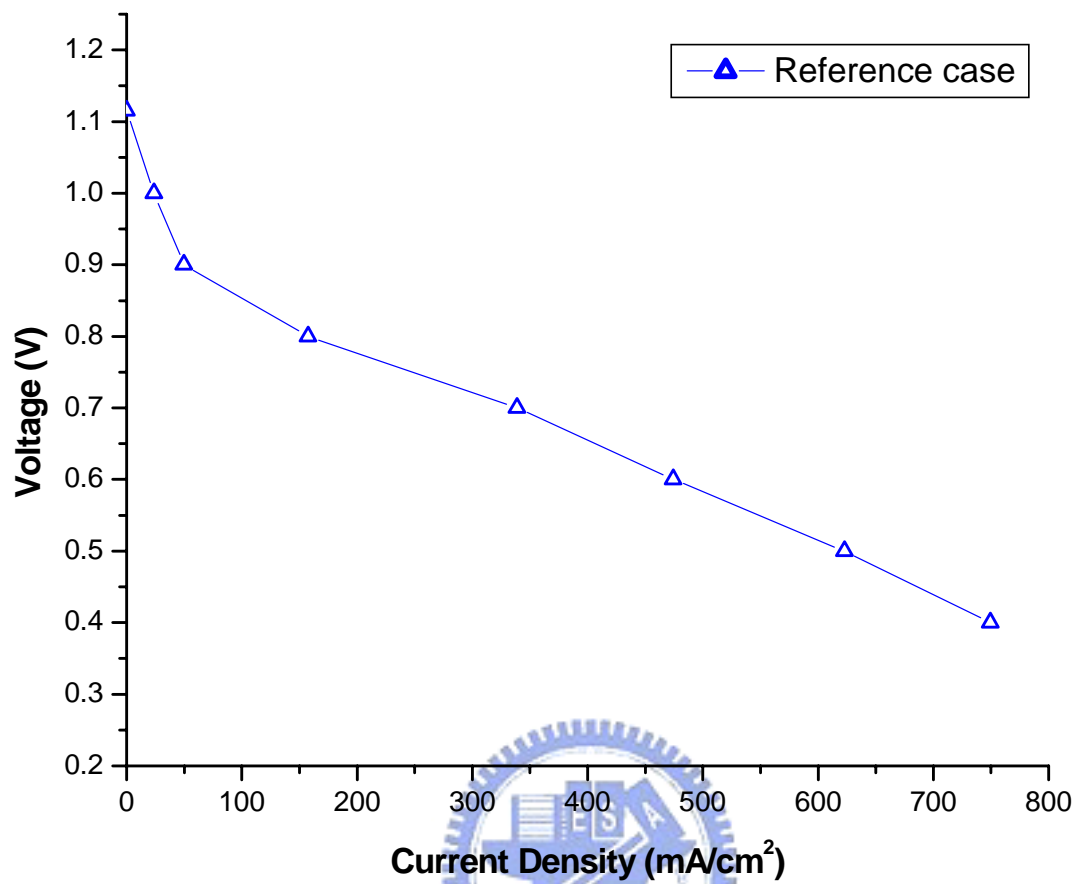


Fig. 4.1 Polarization curve of reference case.

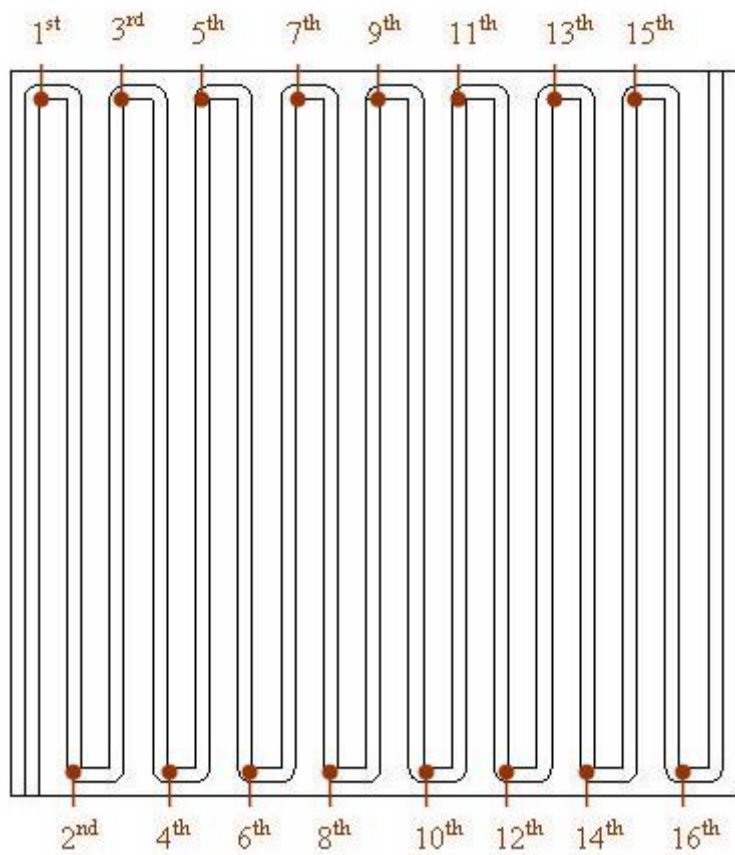


Fig. 4.2 The specified number for each bend entrance along anodic flow channel where the corresponding values of Pe number are obtained.

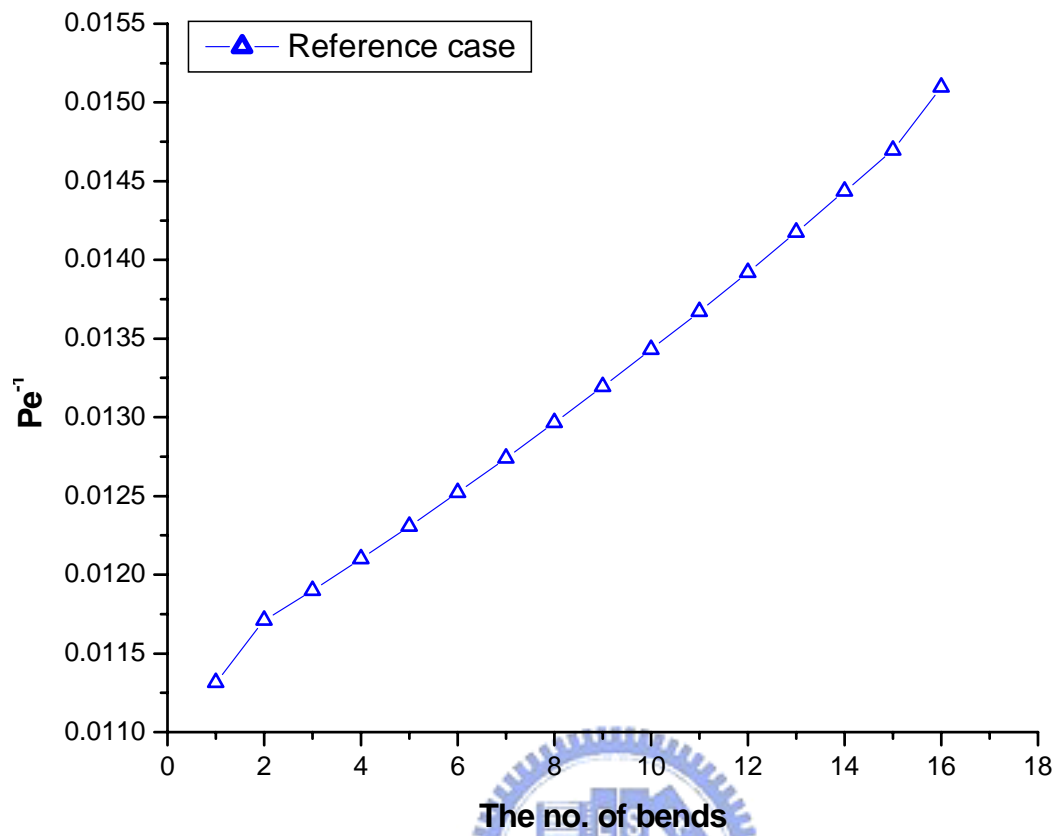


Fig. 4.3 The inverse of local Peclet number at each bend entrance (0.4V).

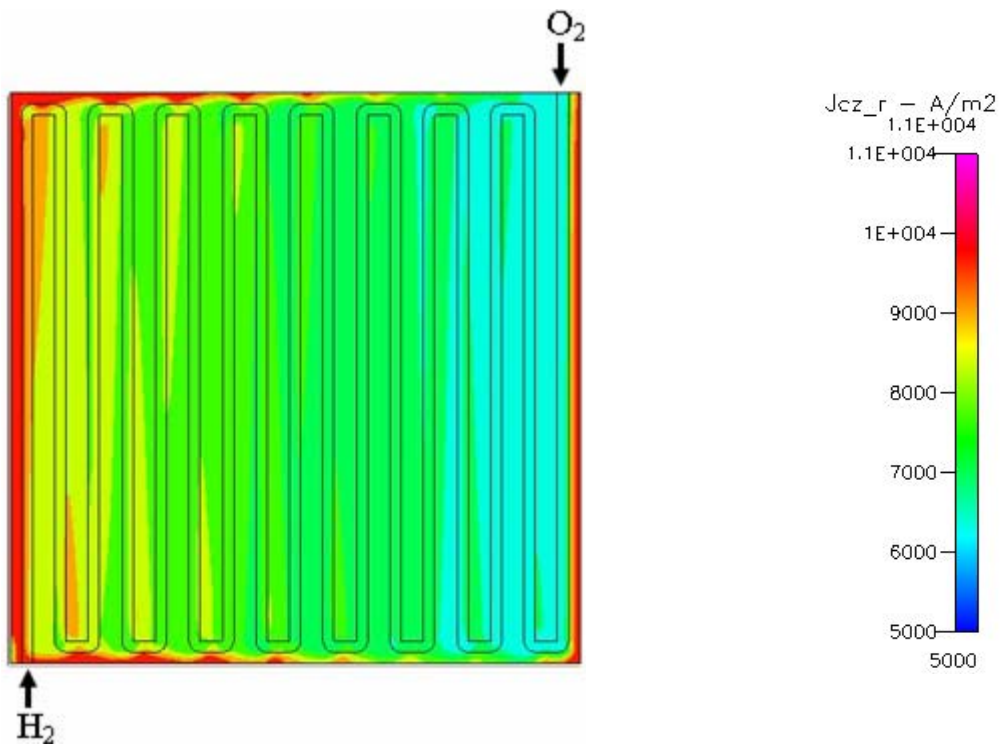
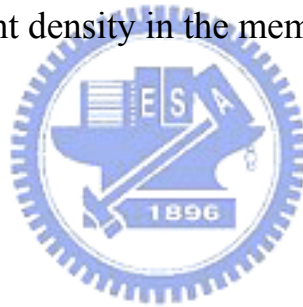


Fig. 4.4 Distribution of current density in the membrane at 0.4V.



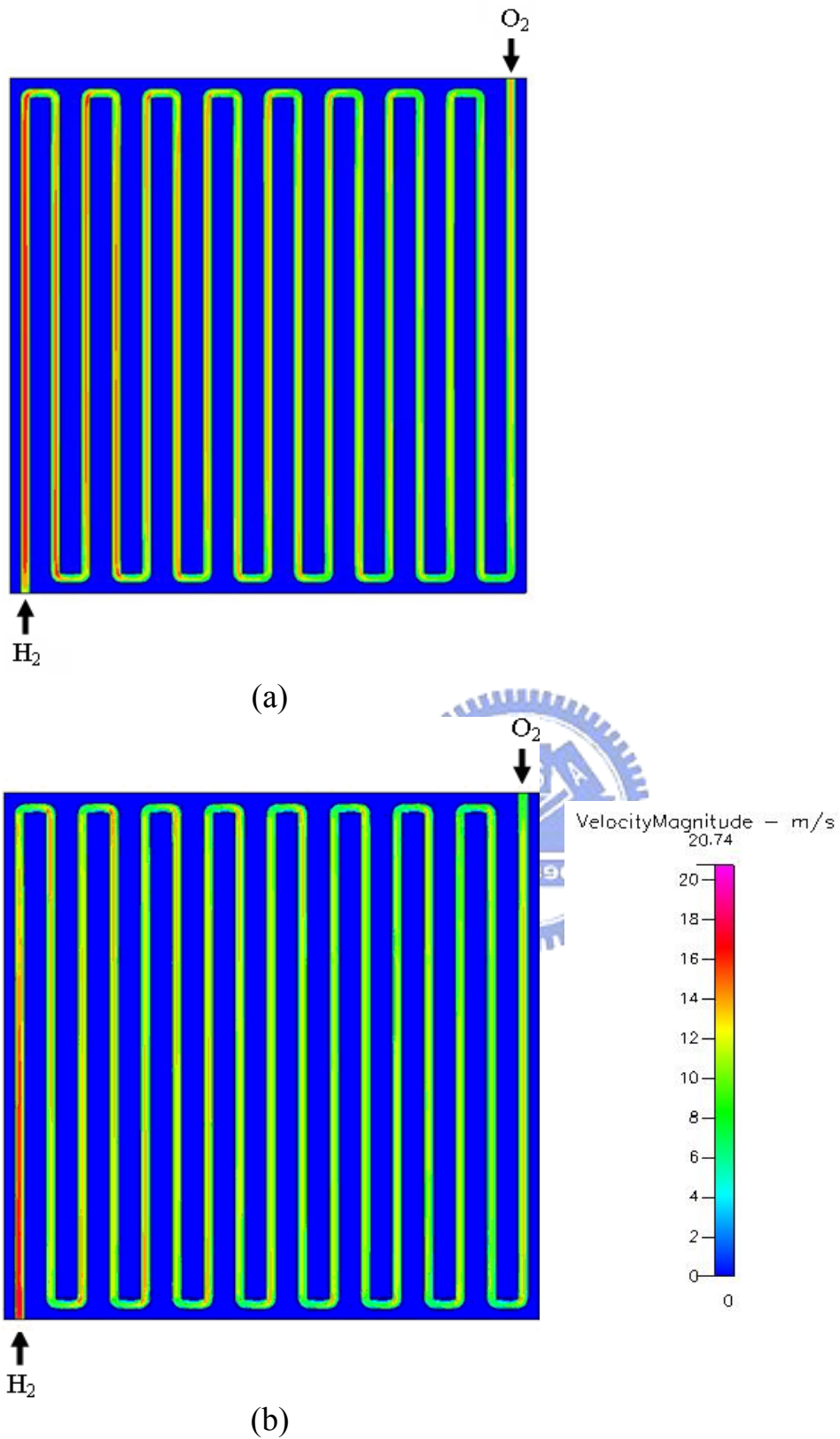


Fig. 4.5 Distributions of flow velocity in PEMFC at 0.4V: (a) anodic channel; (b) cathodic channel.

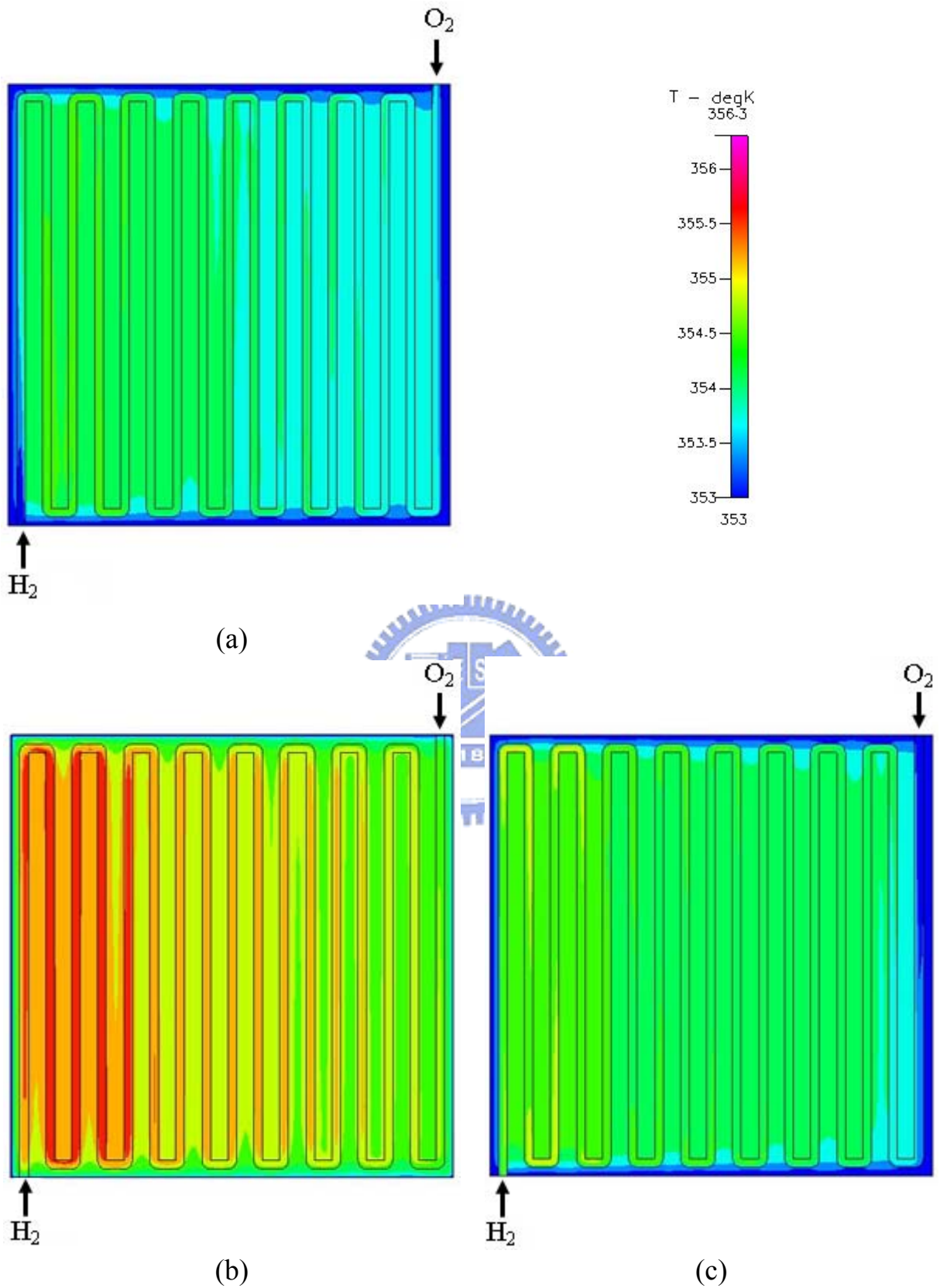


Fig. 4.6 Distributions of temperature: (a) at anodic channel; (b) in the membrane; (c) at cathodic channel.

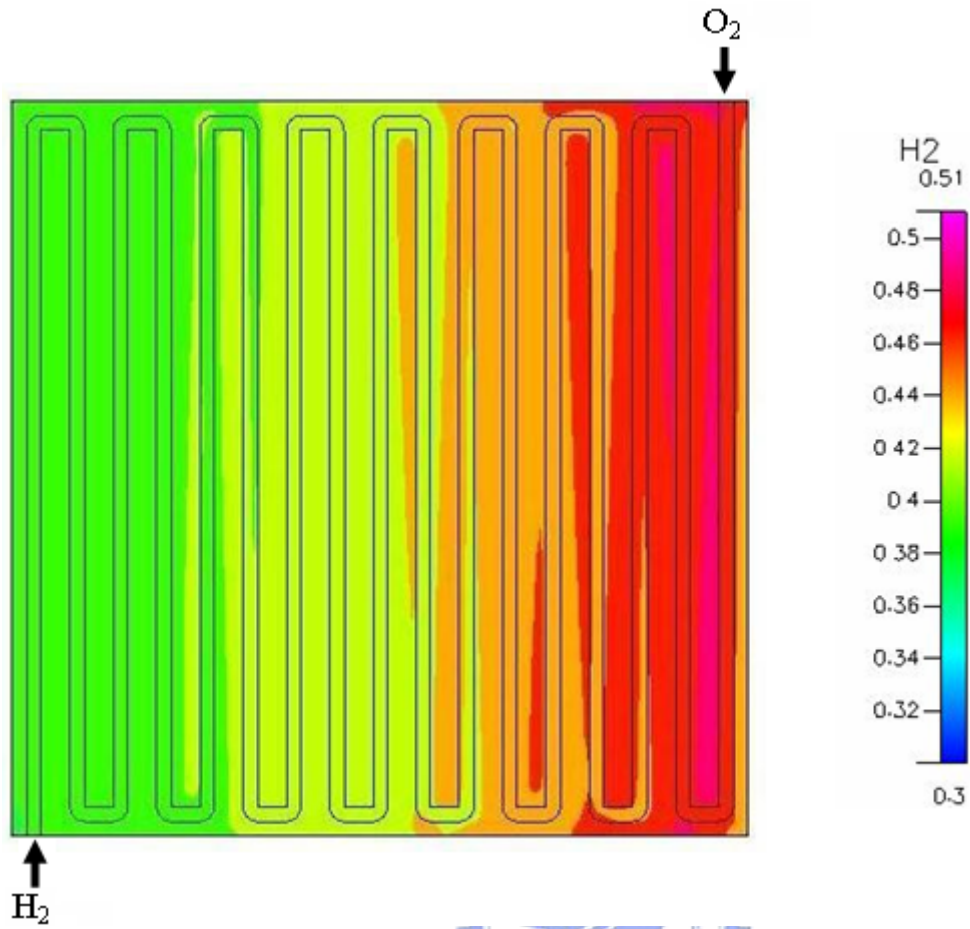


Fig. 4.7 Distribution of hydrogen concentration on the interface between anodic GDL and catalyst layer at operating voltage of 0.4V.



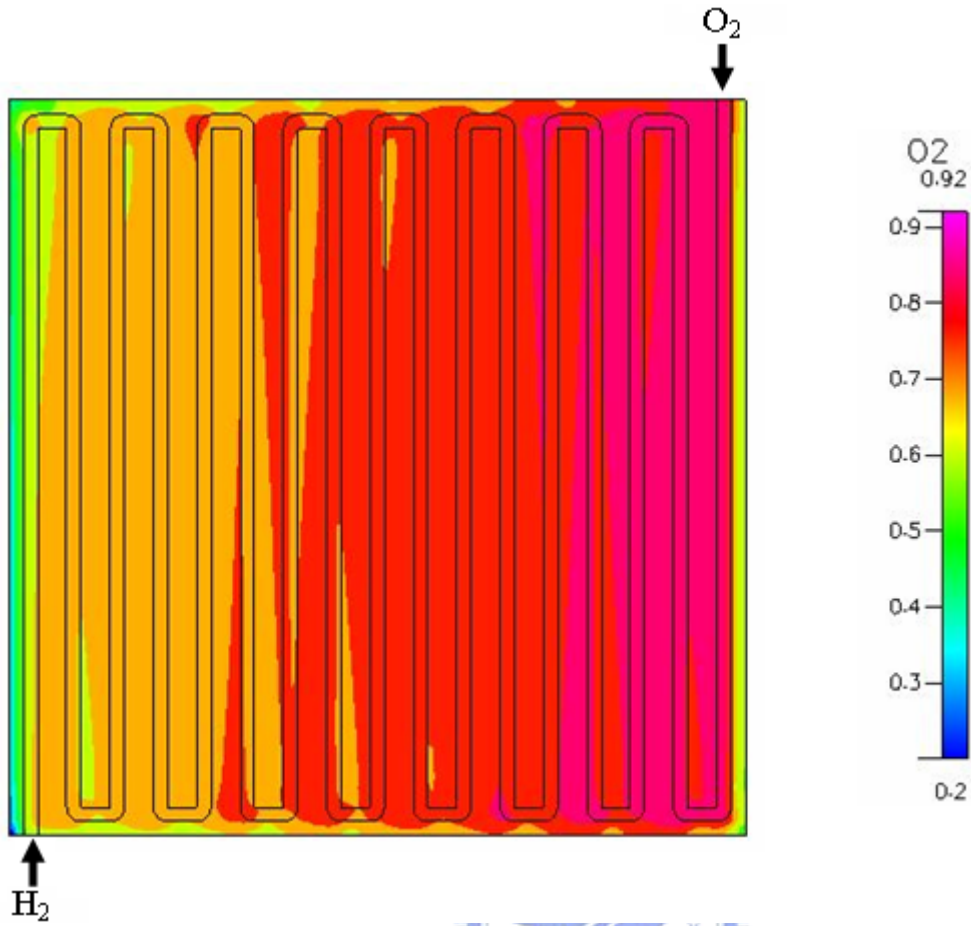


Fig. 4.8 Distribution of oxygen concentration on the interface between cathodic GDL and catalyst layer at operating voltage of 0.4V.

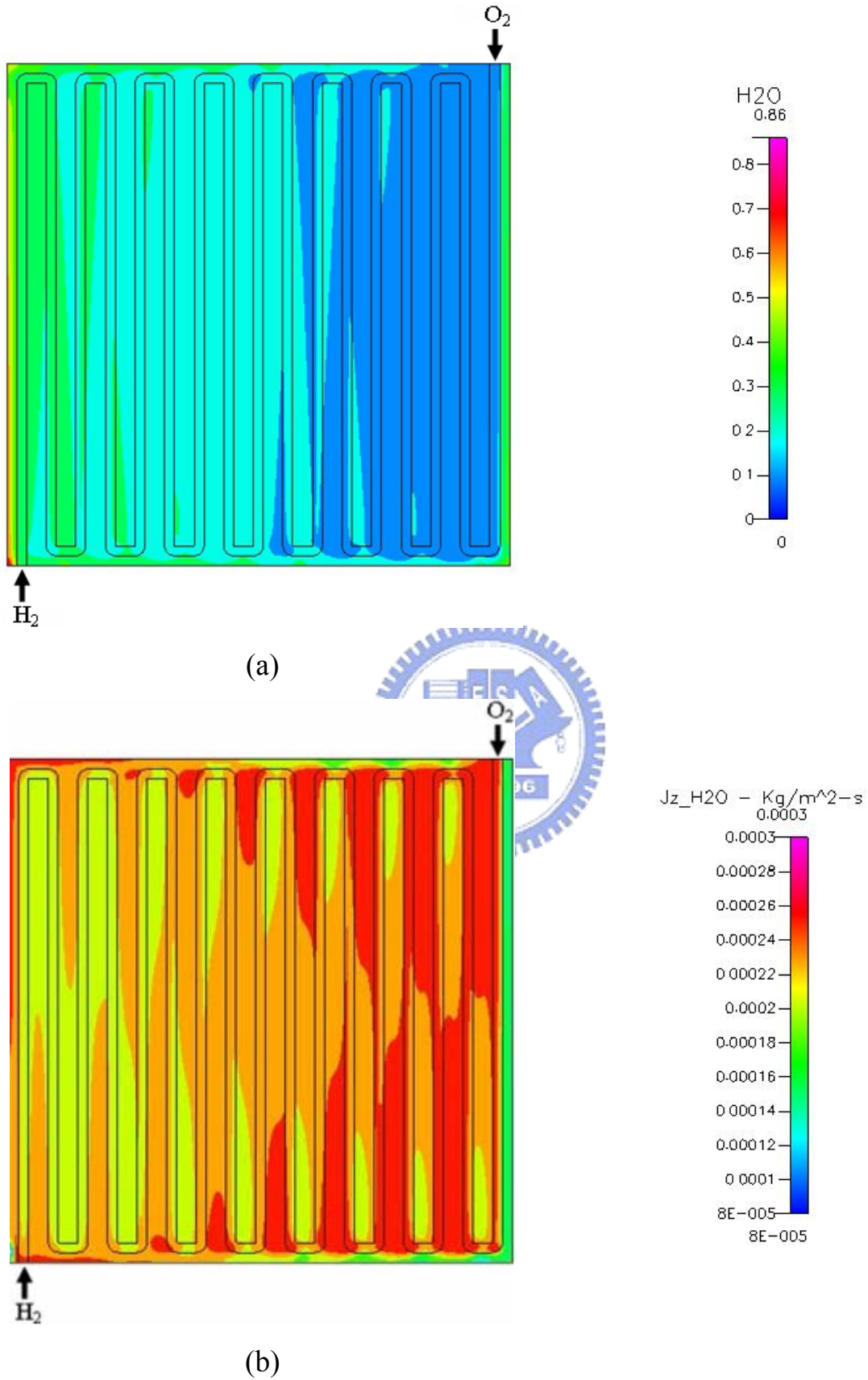


Fig. 4.9 Distribution of water gas on the interface between cathodic GDL and catalyst layer and water flux in the membrane at operating voltage of 0.4V.

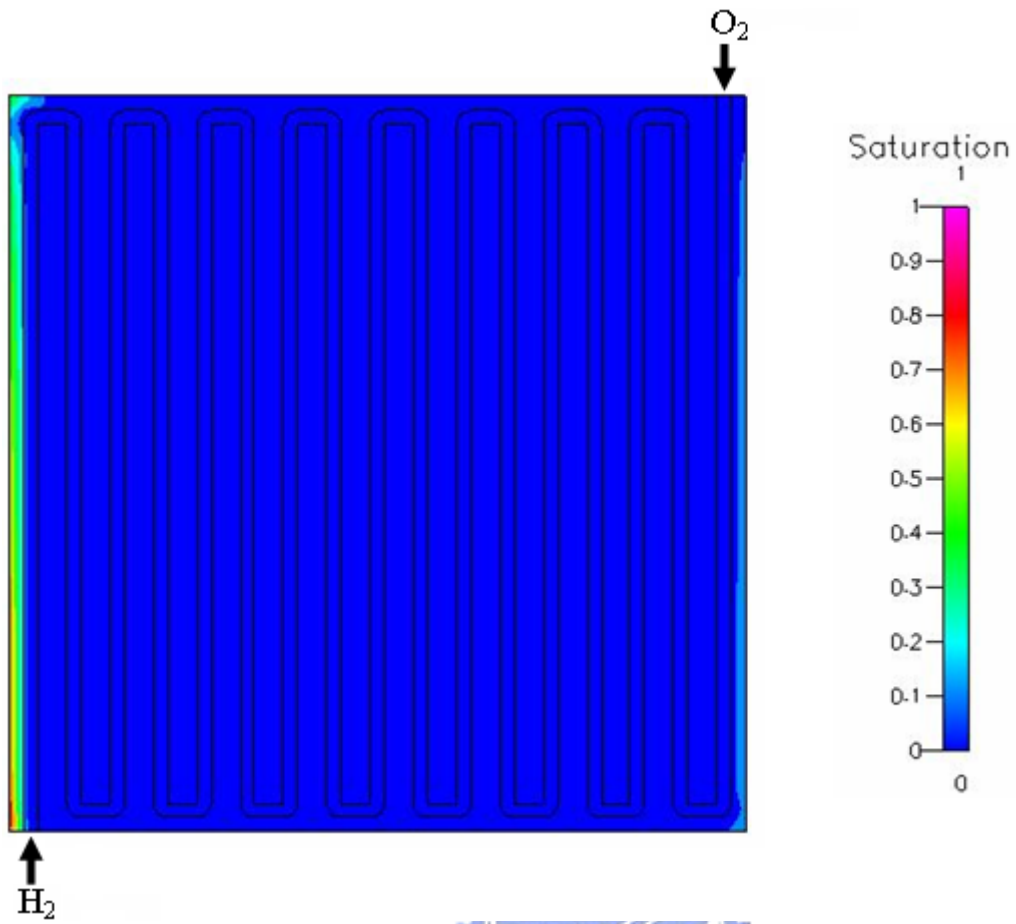


Fig. 4.10 Distribution of liquid water on the interface between cathodic GDL and catalyst layer at operating voltage of 0.4V

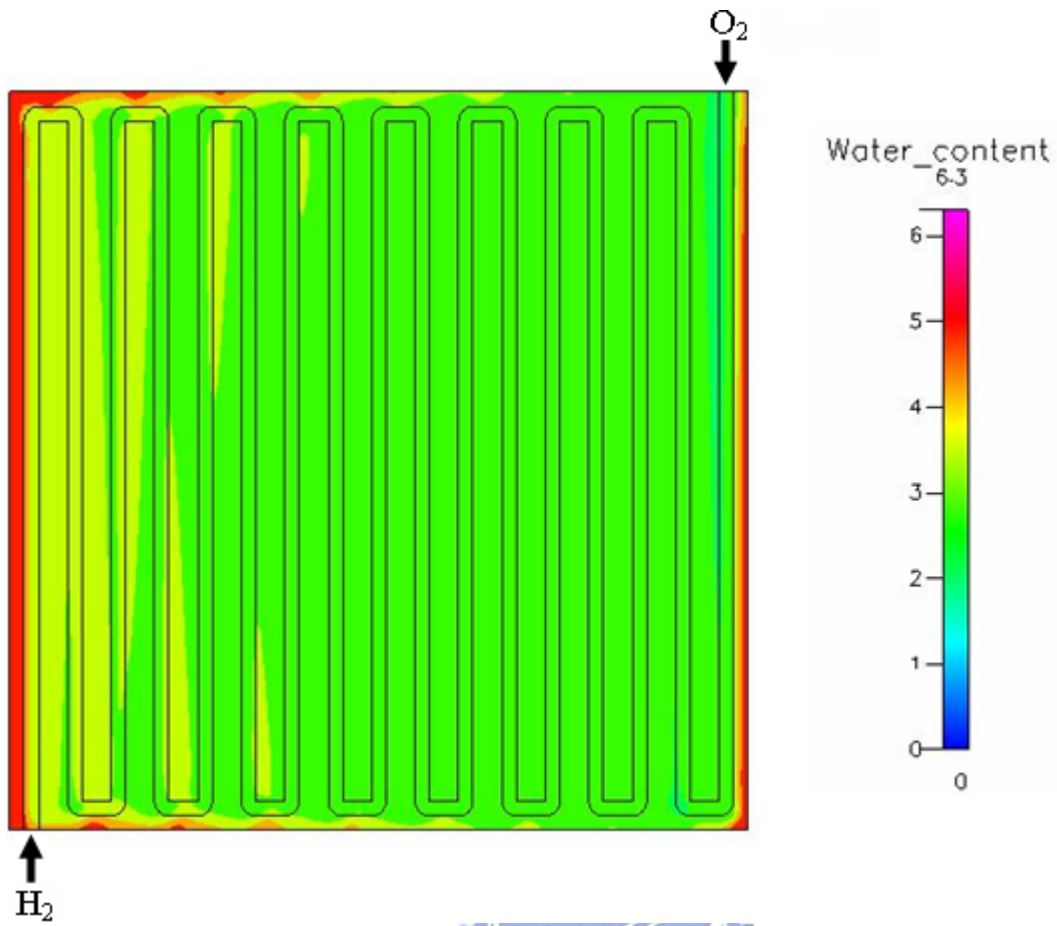


Fig. 4.11 Distribution of water content in the membrane at 0.4V.



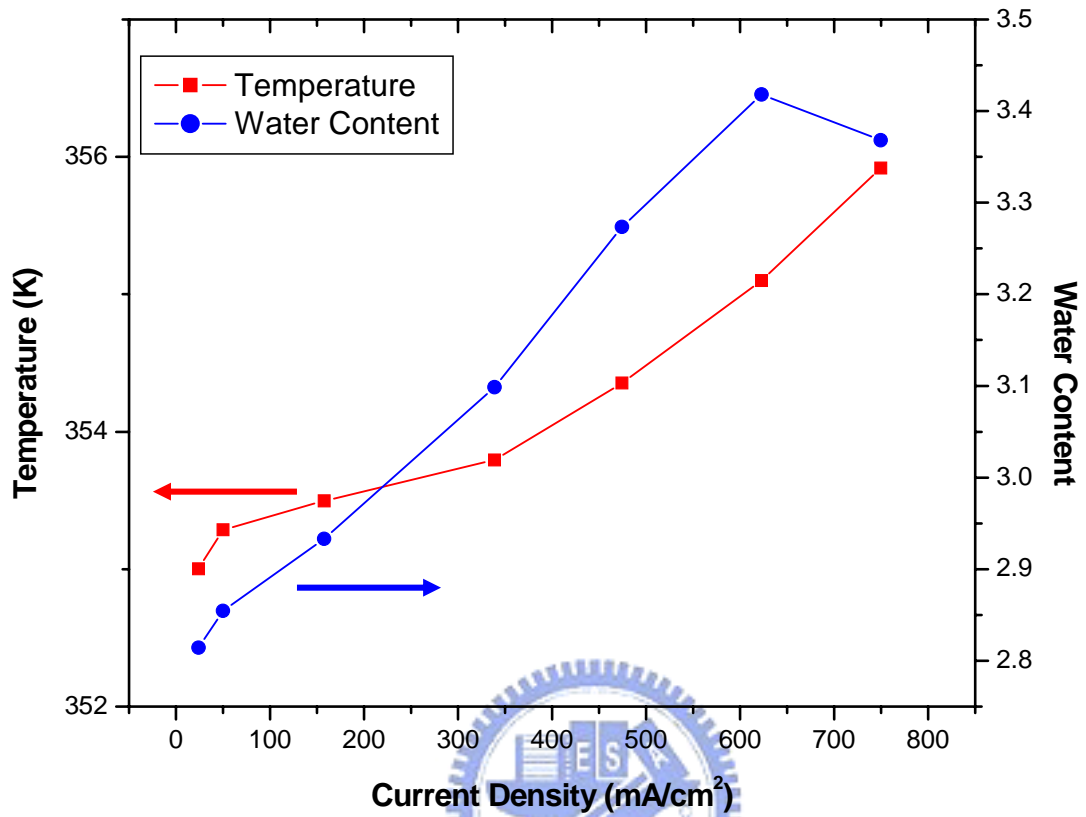


Fig. 4.12 Average values of temperature and water content for each current density.

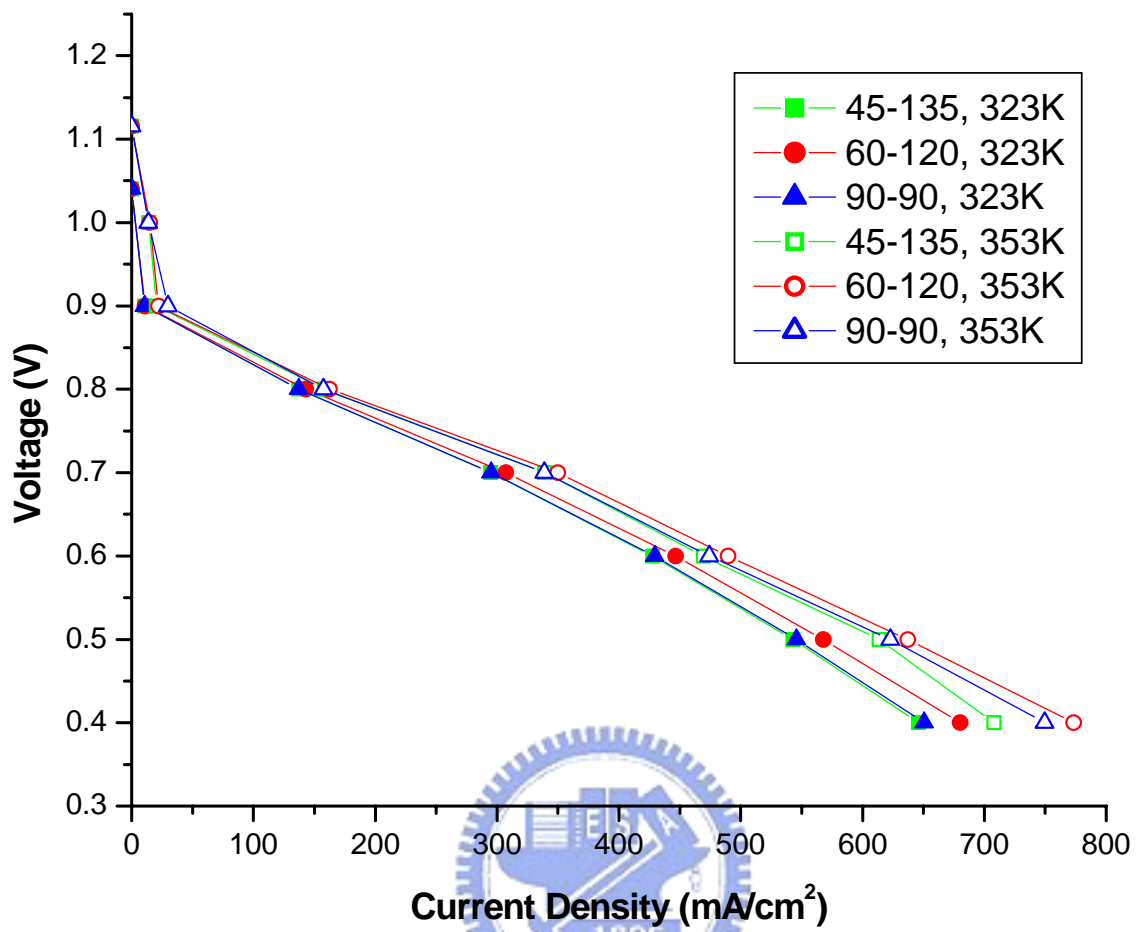


Fig. 4.13 Polarization curves of flow patterns with three different bend angles at 323K and 353K.

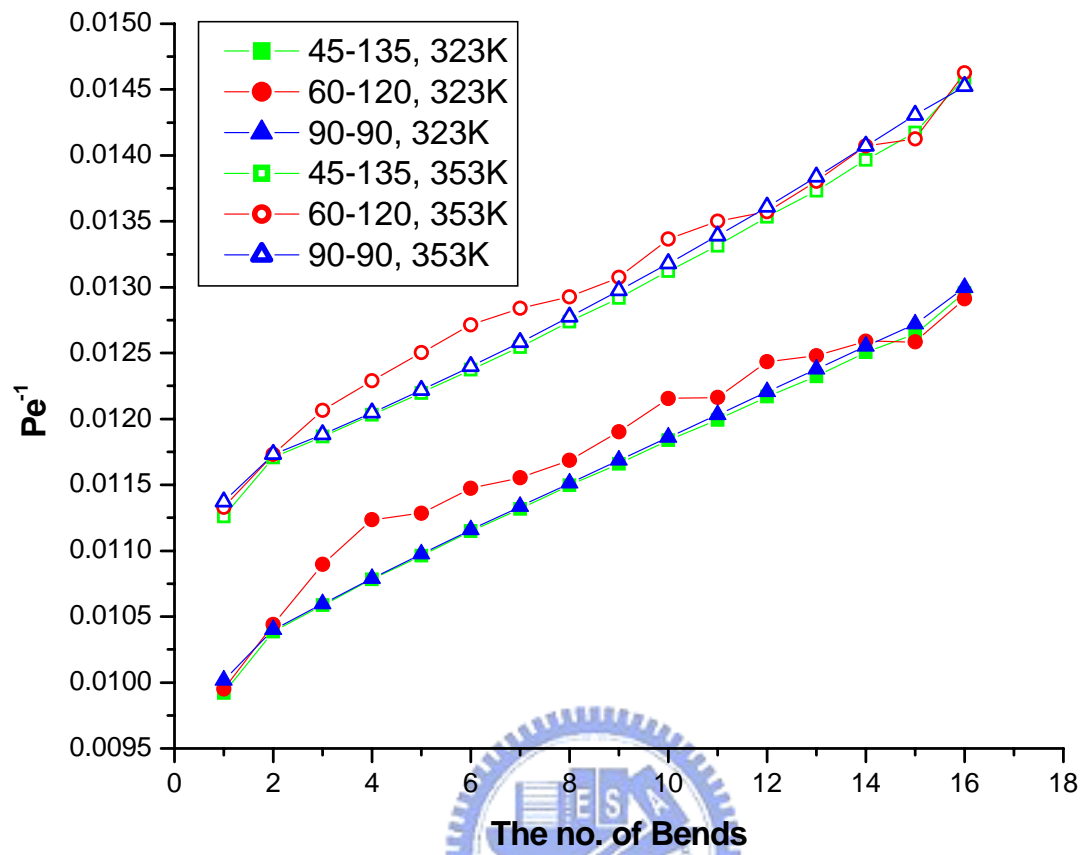


Fig. 4.14 The inverse of Peclet number at each bend entrance.

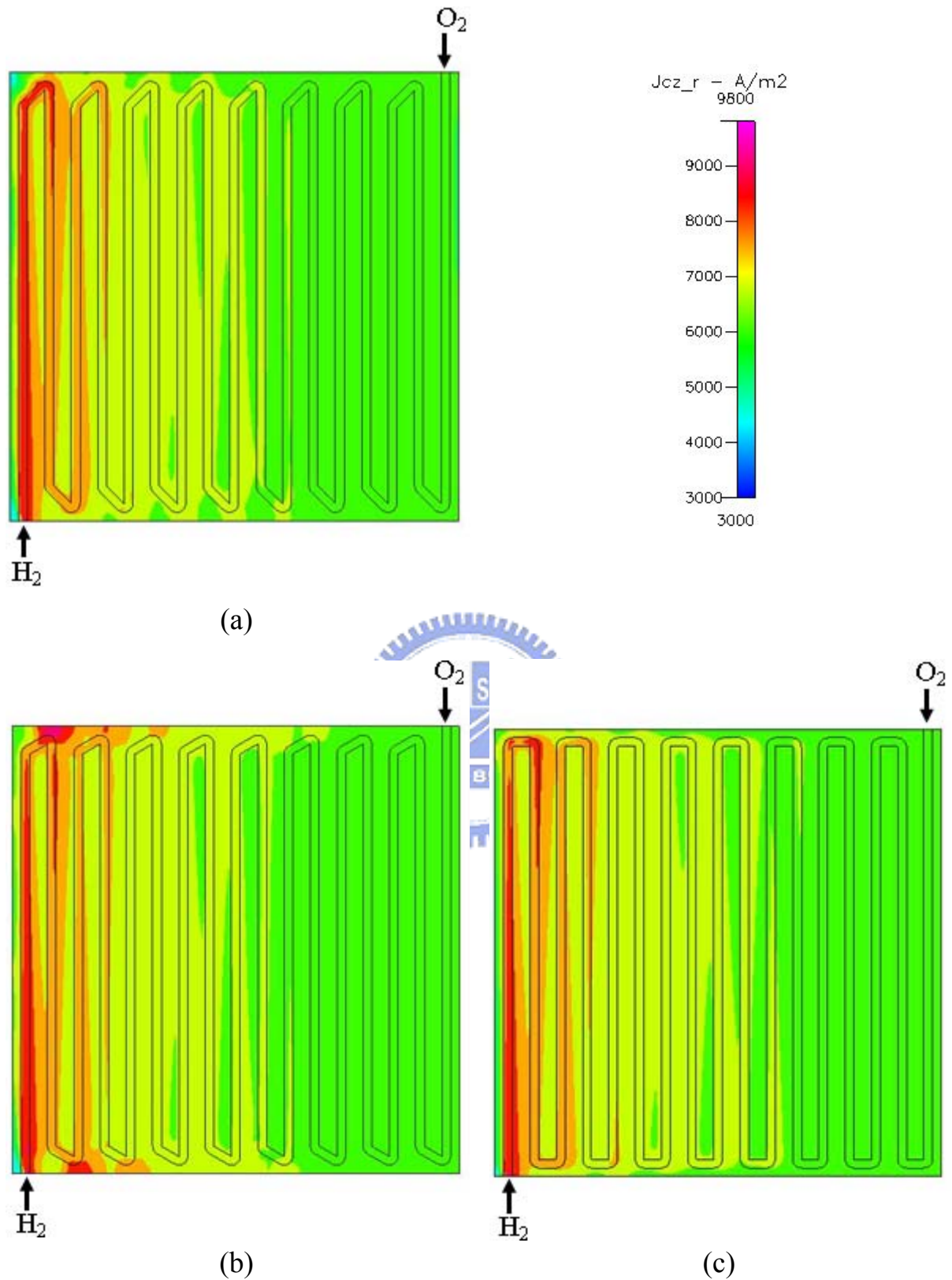


Fig. 4.15 Distributions of current density in the membrane at 323K (0.4V): (a) 45-135 flow pattern; (b) 60-120 flow pattern; (c) 90-90 flow pattern.



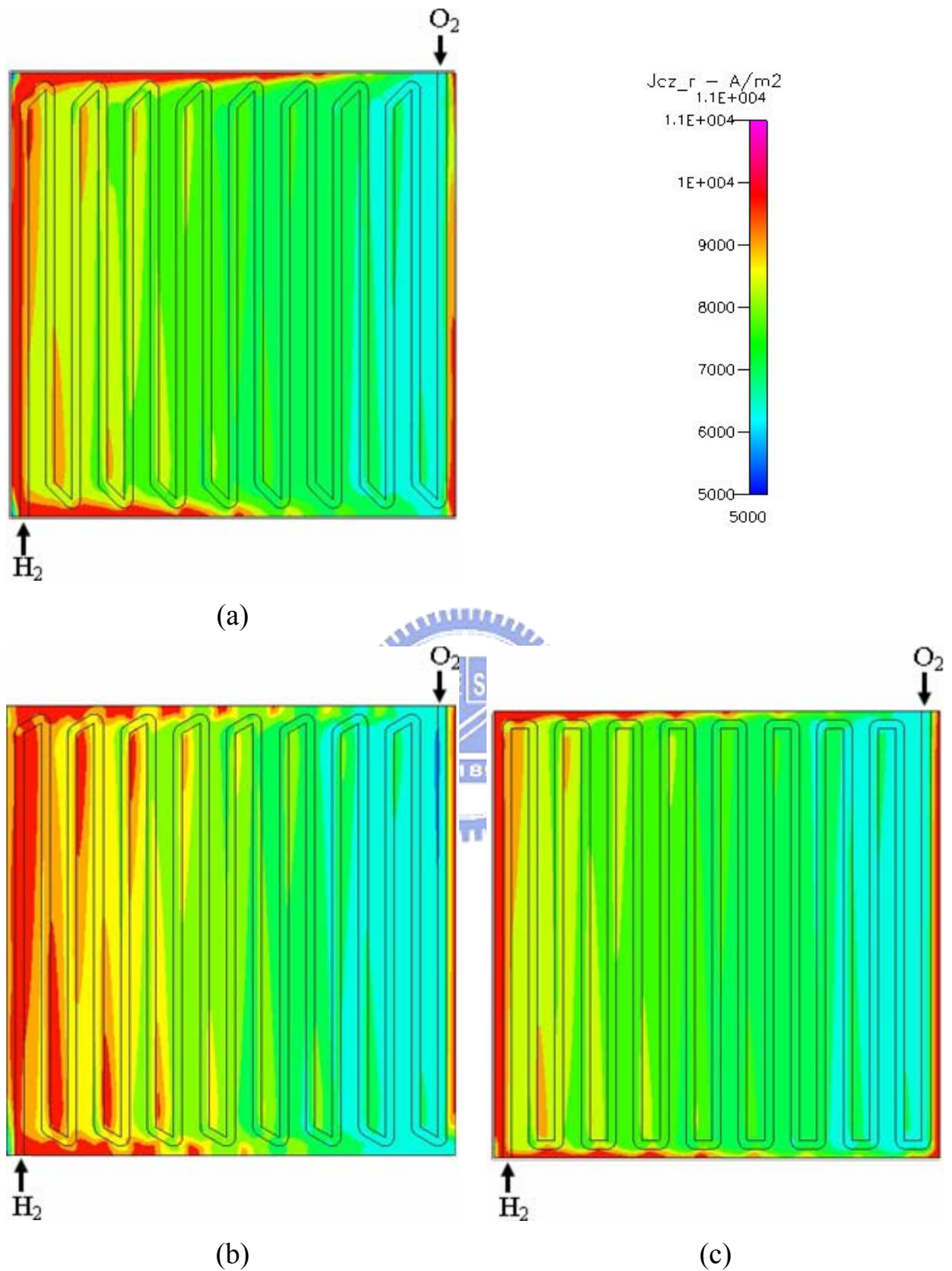


Fig. 4.16 Distributions of current density in the membrane at 353K (0.4V): (a) 45-135 flow pattern; (b) 60-120 flow pattern; (c) 90-90 flow pattern.

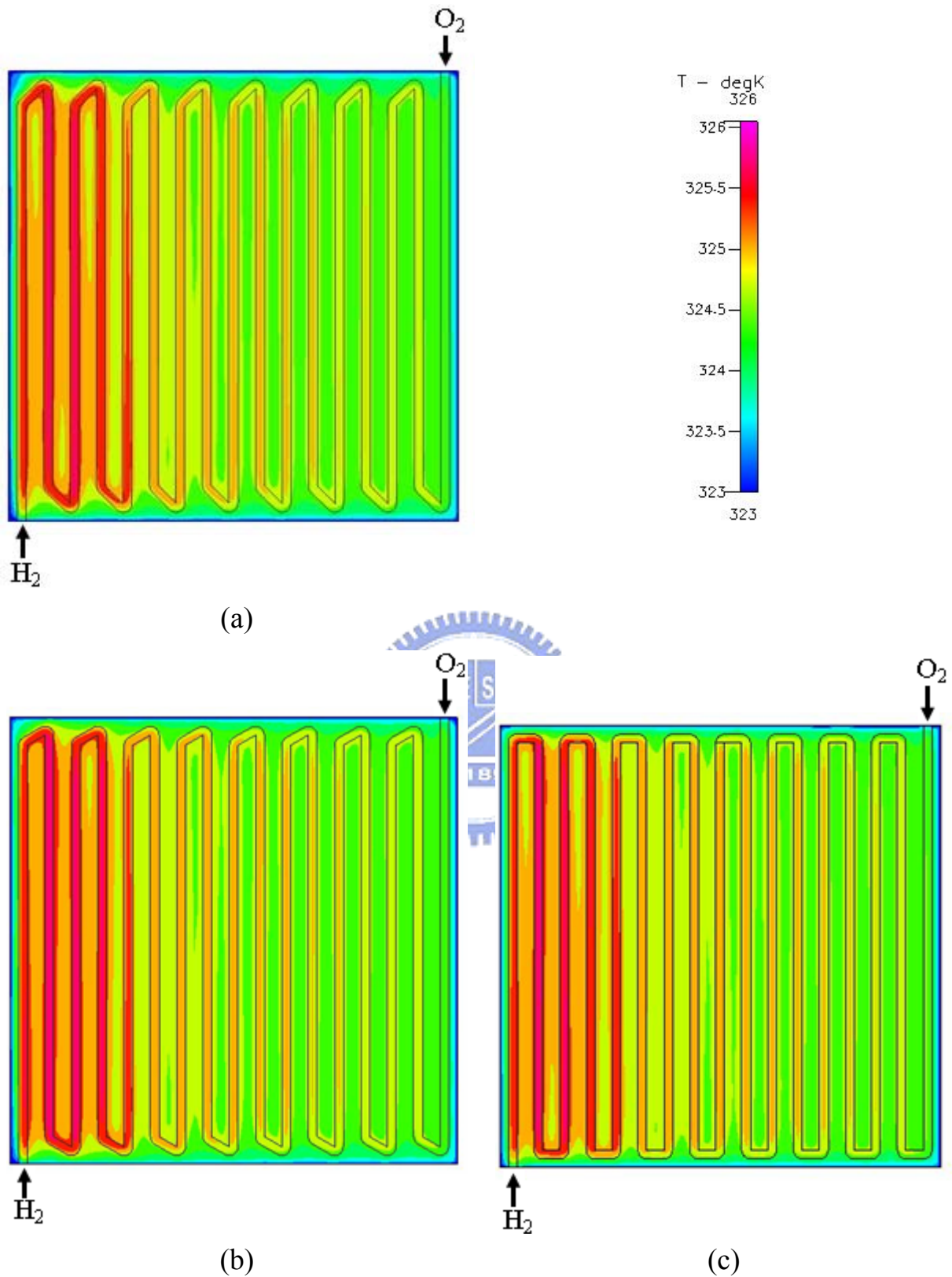


Fig. 4.17 Distributions of temperature in the membrane at 323K (0.4V): (a) 45-135 flow pattern; (b) 60-120 flow pattern; (c) 90-90 flow pattern.

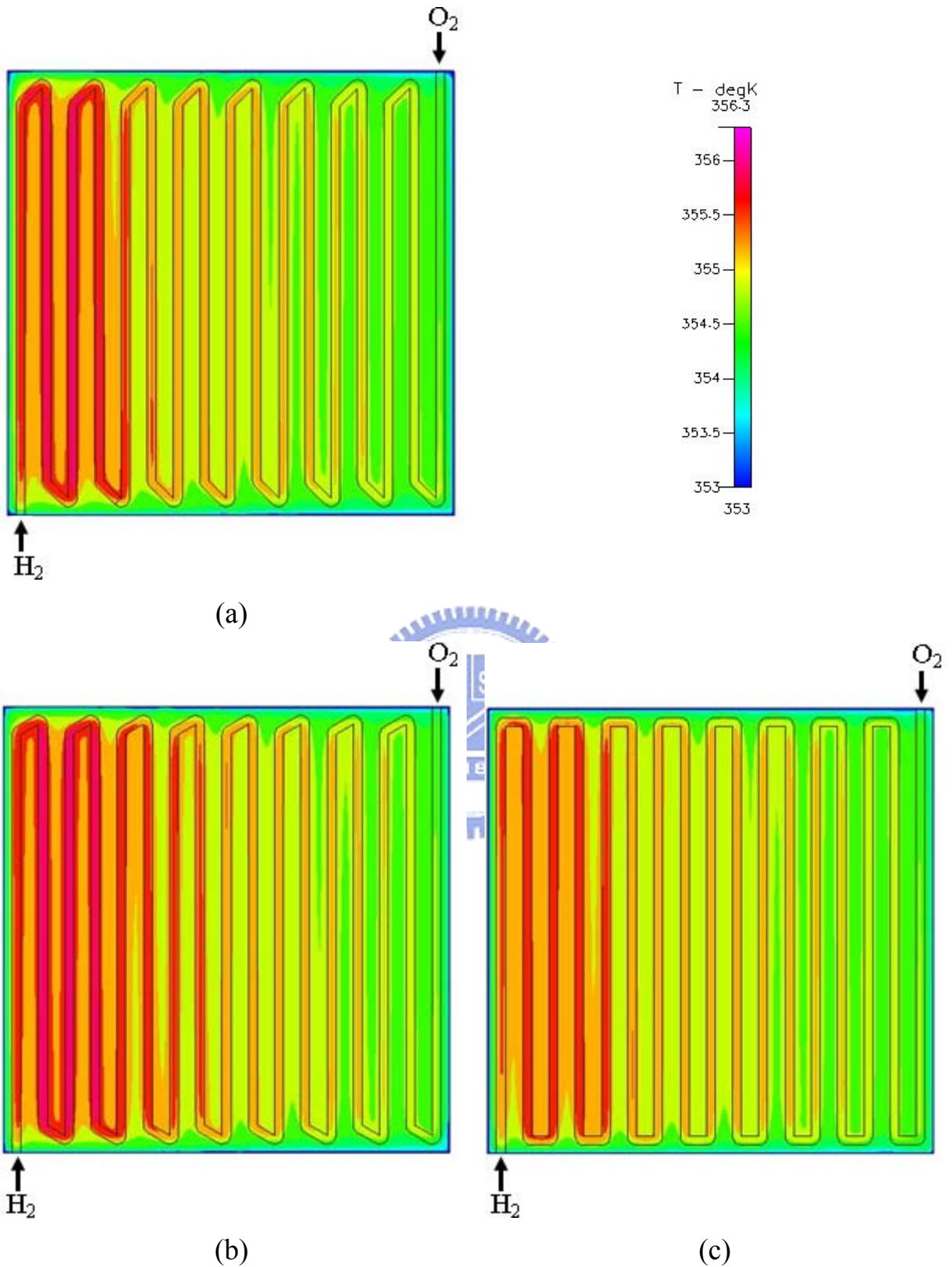


Fig. 4.18 Distributions of temperature in the membrane at 353K (0.4V): (a) 45-135 flow pattern; (b) 60-120 flow pattern; (c) 90-90 flow pattern.

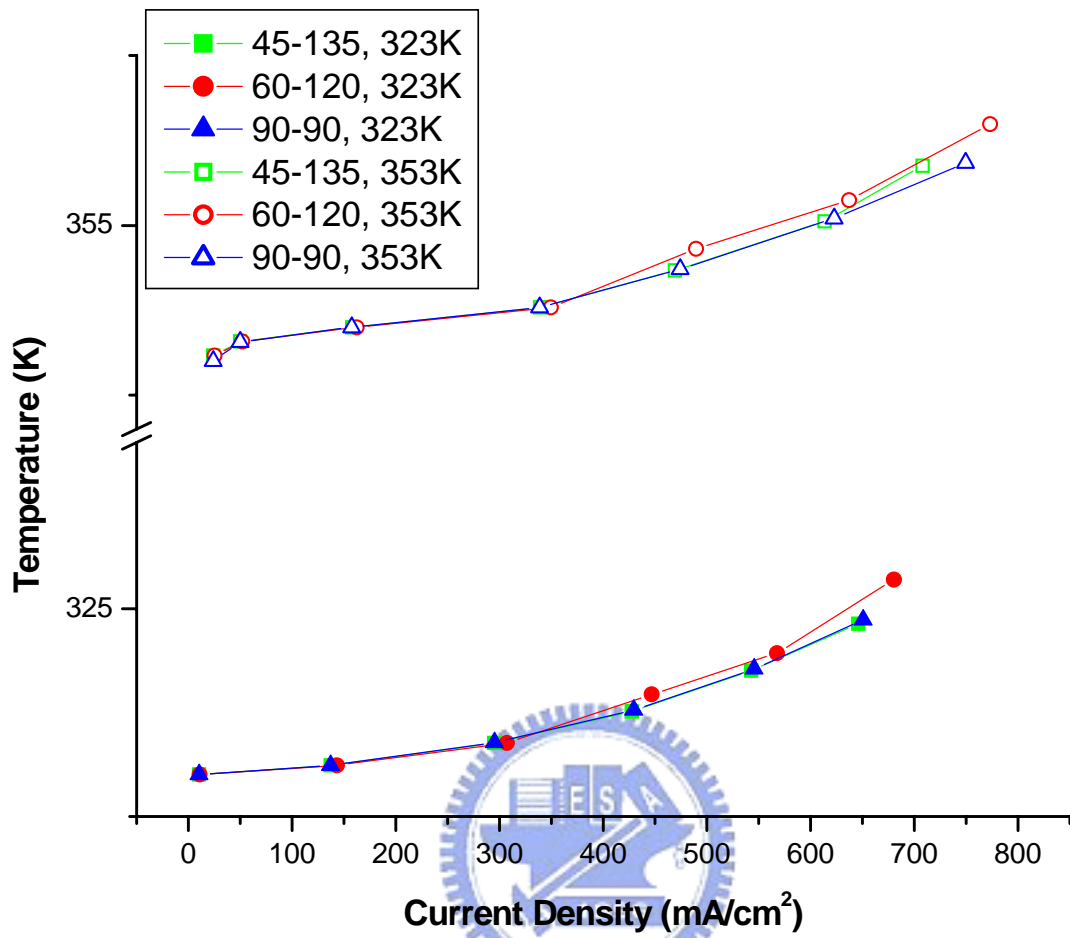


Fig. 4.19 Average value of temperature in the membrane at 323K and 353K.

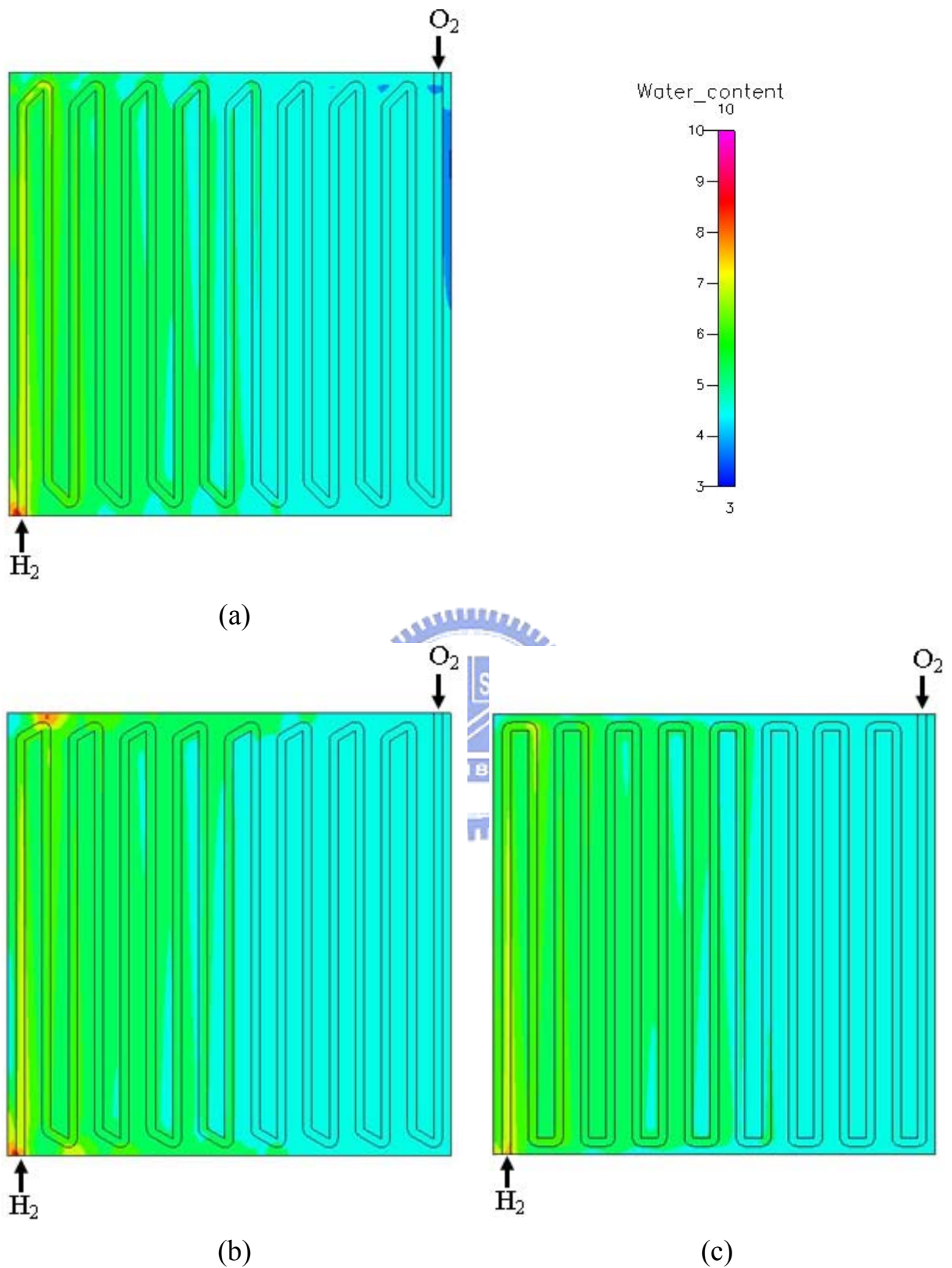


Fig. 4.20 Distributions of water content in membrane at 323K (0.4V): (a) 45-135 flow pattern; (b) 60-120 flow pattern; (c) 90-90 flow pattern.

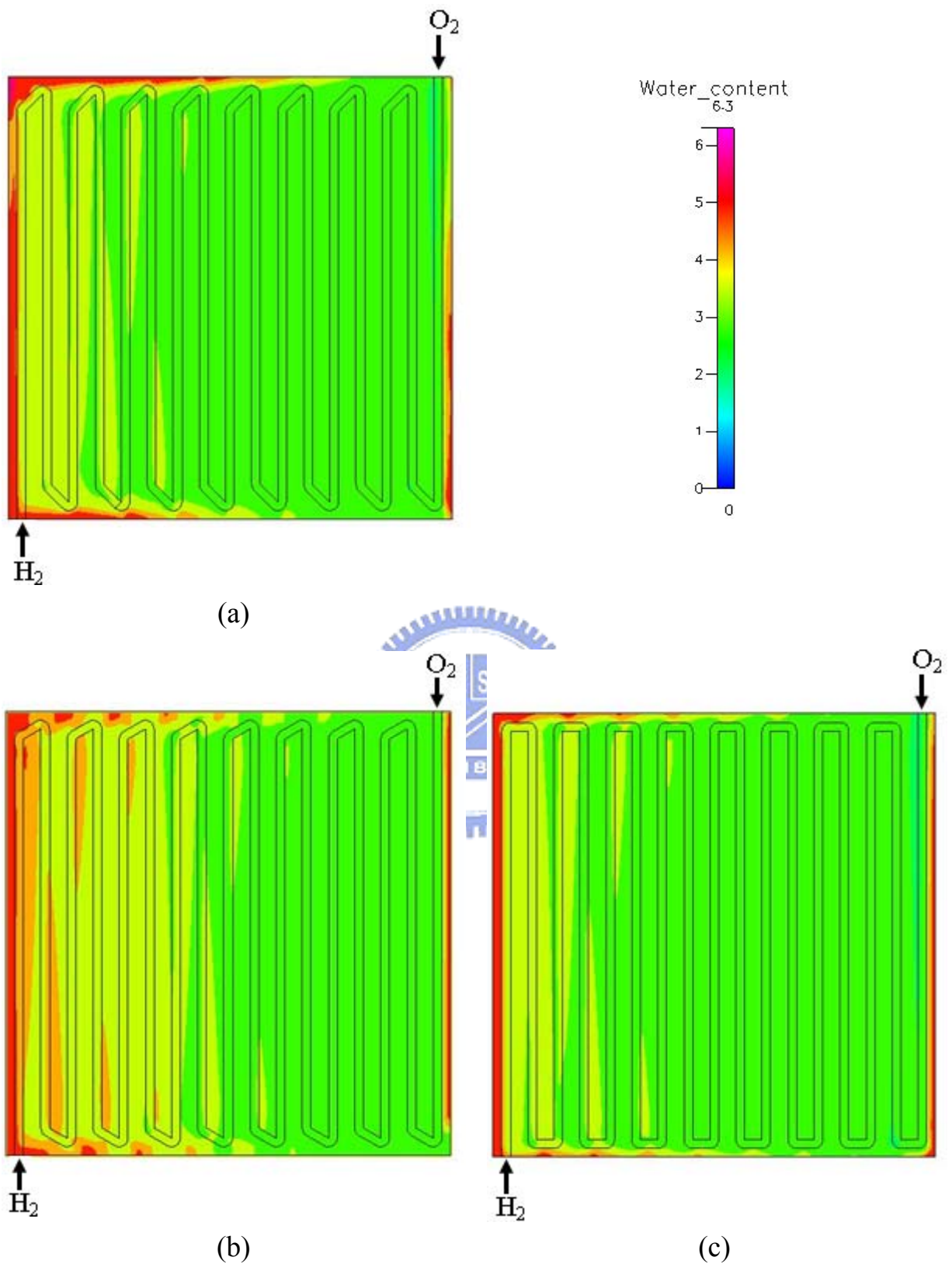


Fig. 4.21 Distributions of water content in membrane at 353K (0.4V): (a) 45-135 flow pattern; (b) 60-120 flow pattern; (c) 90-90 flow pattern.

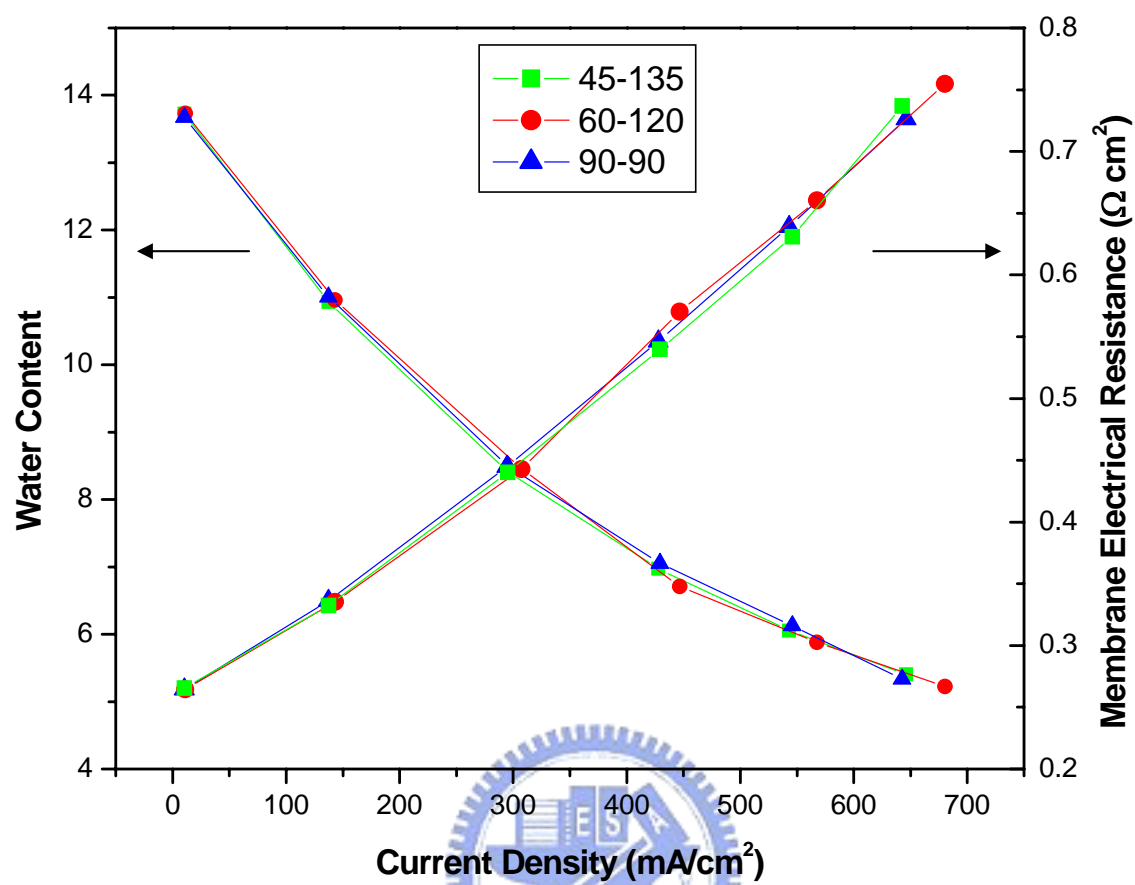


Fig. 4.22 Average value of membrane water content at 323K.

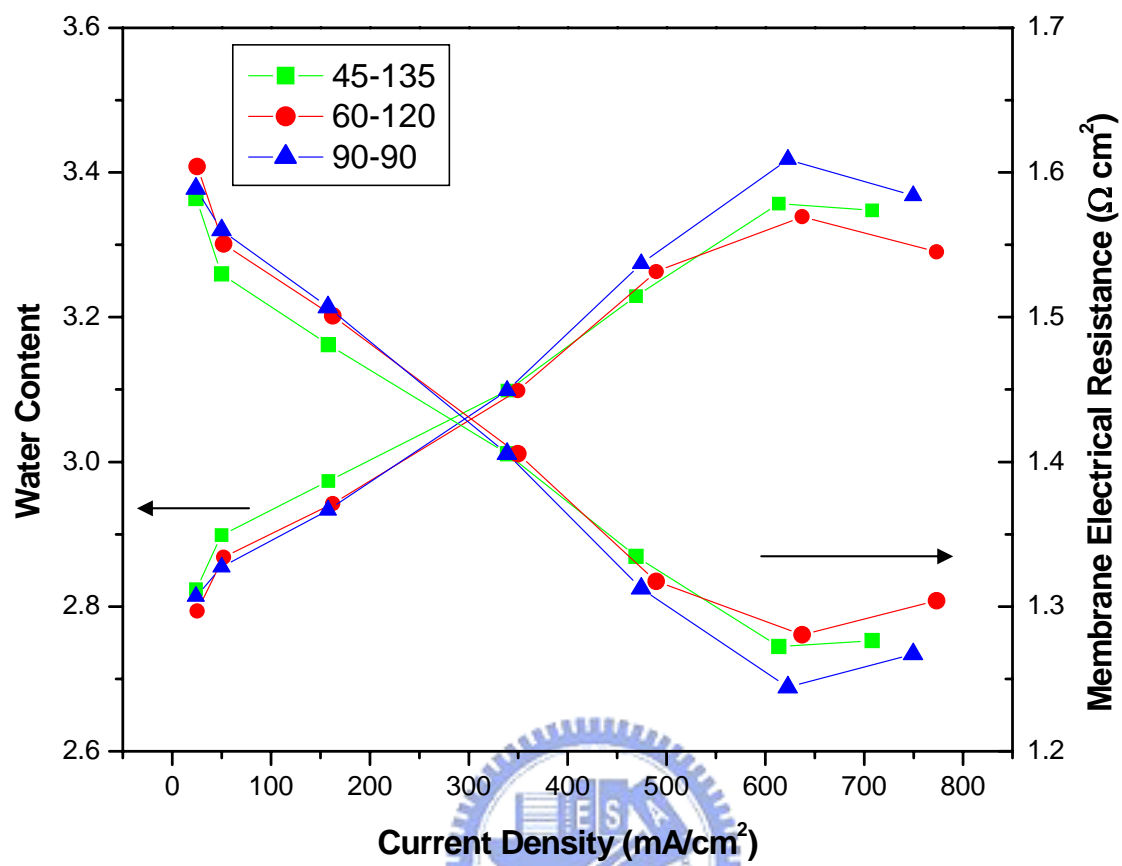


Fig. 4.23 Average value of membrane water content at 353K.



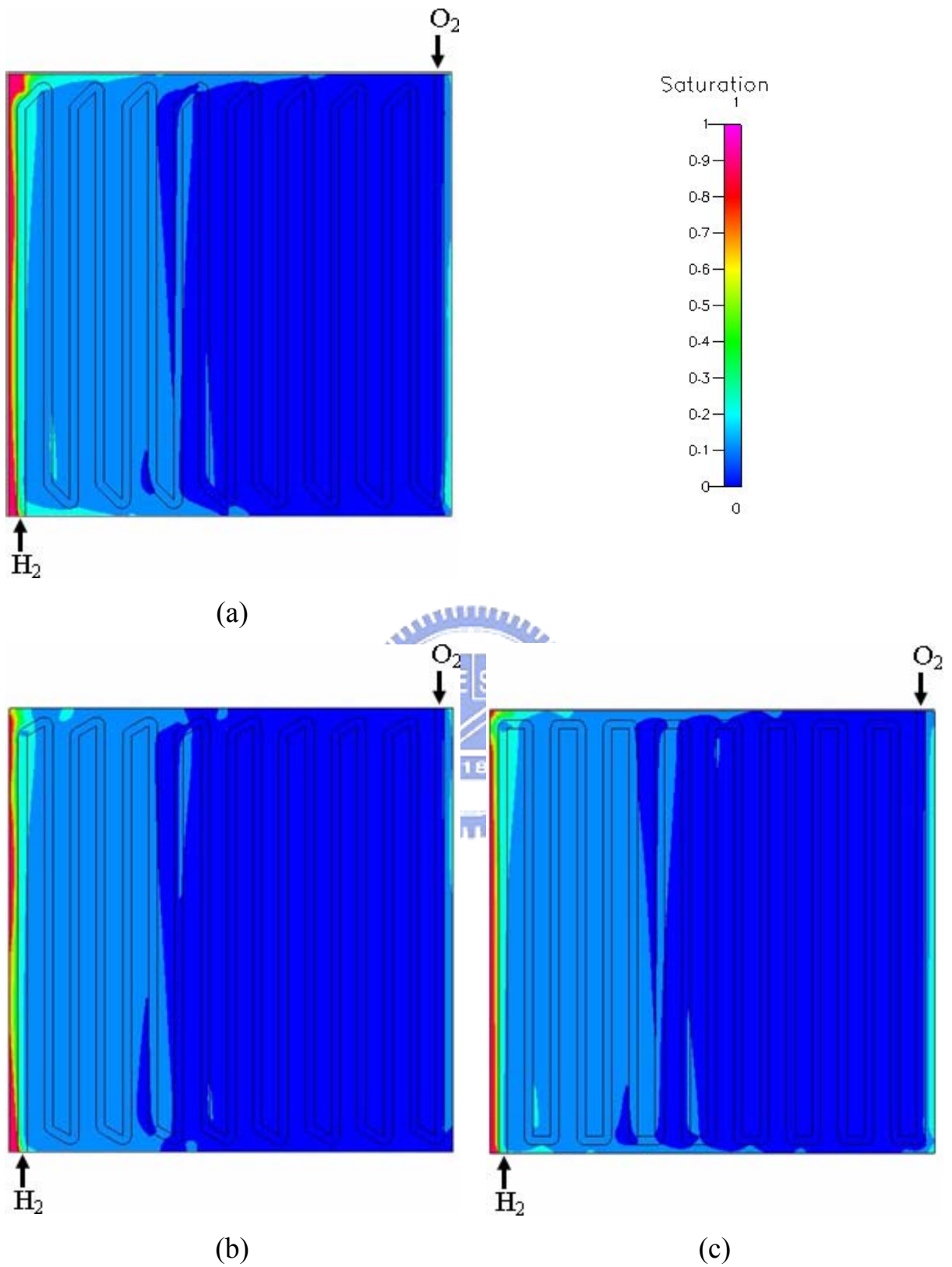


Fig. 4.24 Distributions of saturation on the interface between cathodic GDL and catalyst layer at 323K.

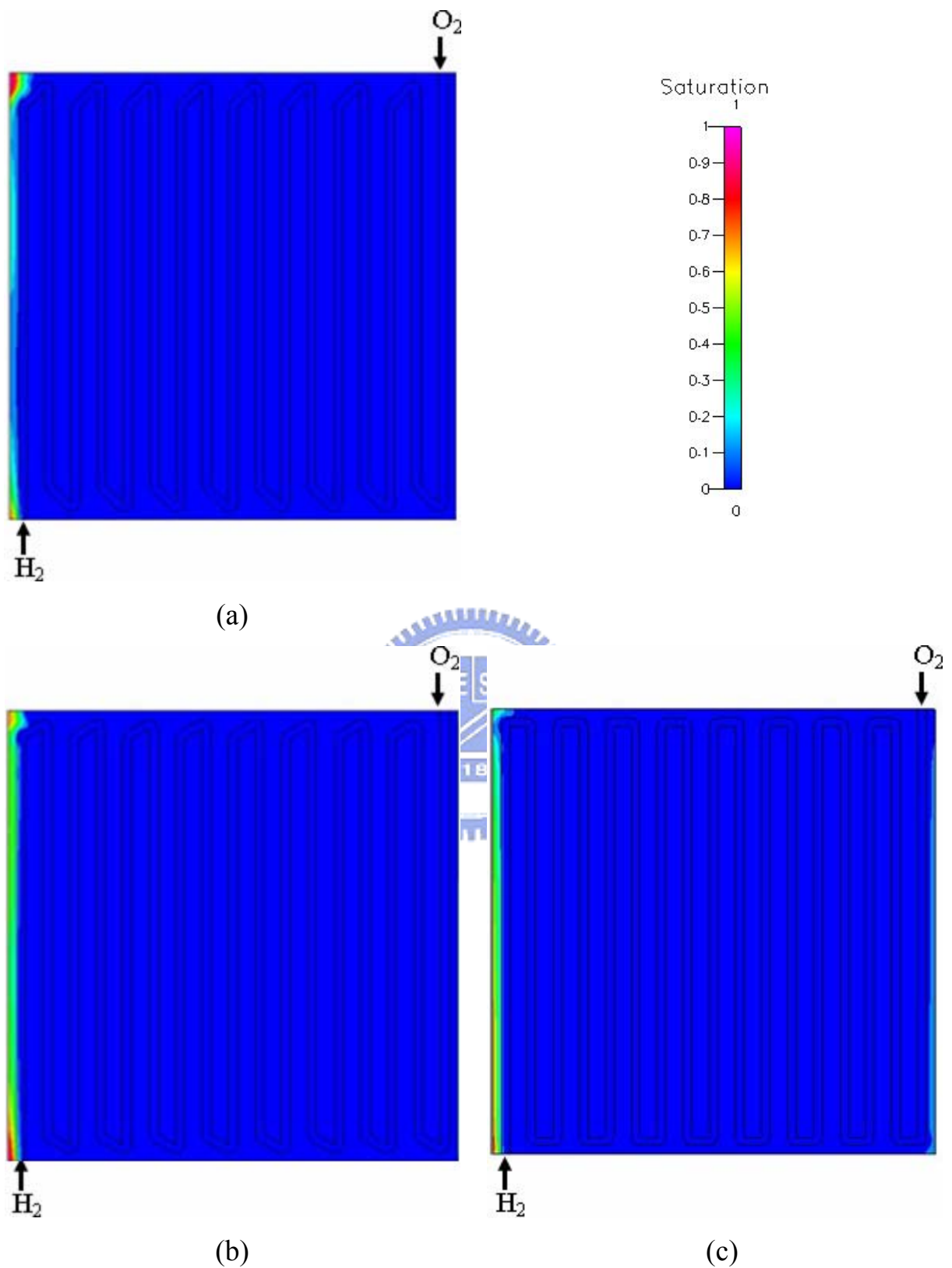


Fig. 4.25 Distributions of saturation on the interface between cathodic GDL and catalyst layer at 353K.

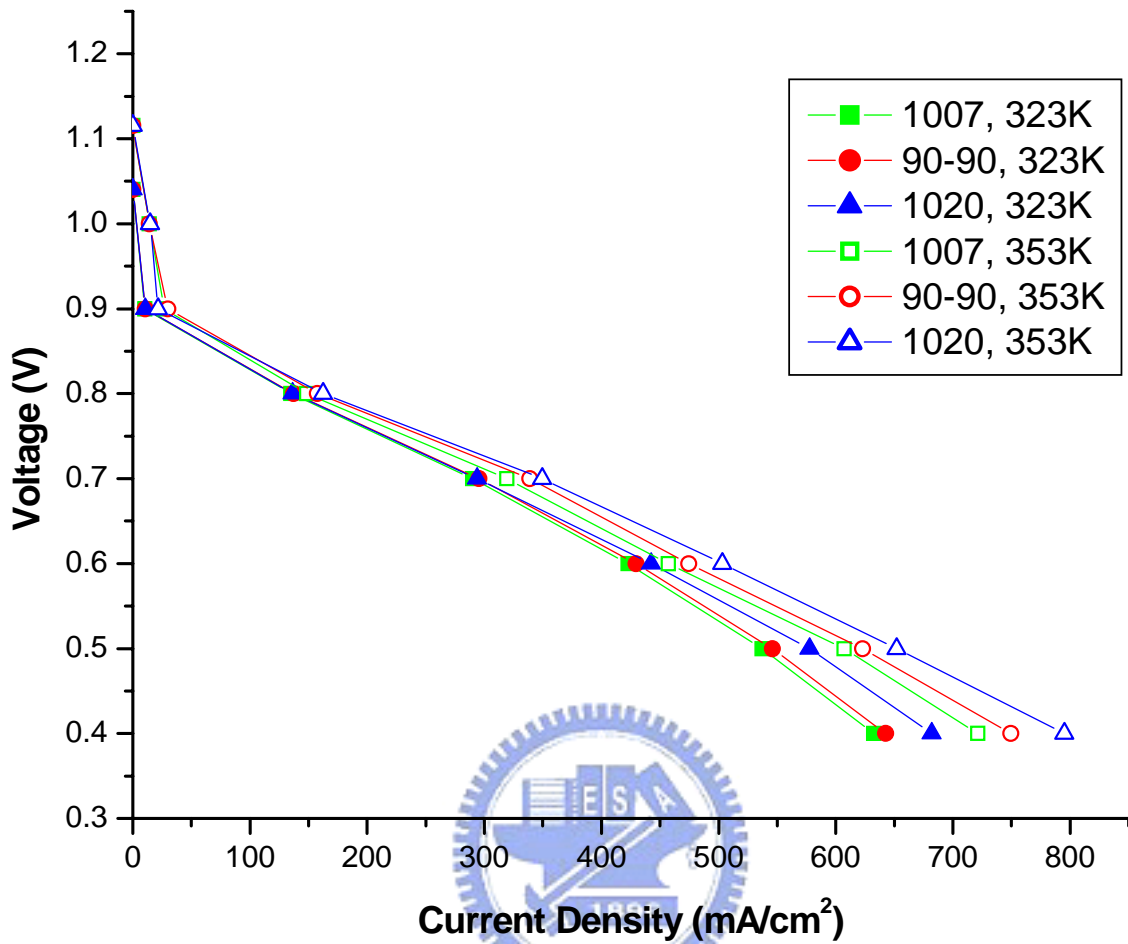


Fig. 4.26 Polarization curves of flow patterns with three different bend widths at 323K and 353K.

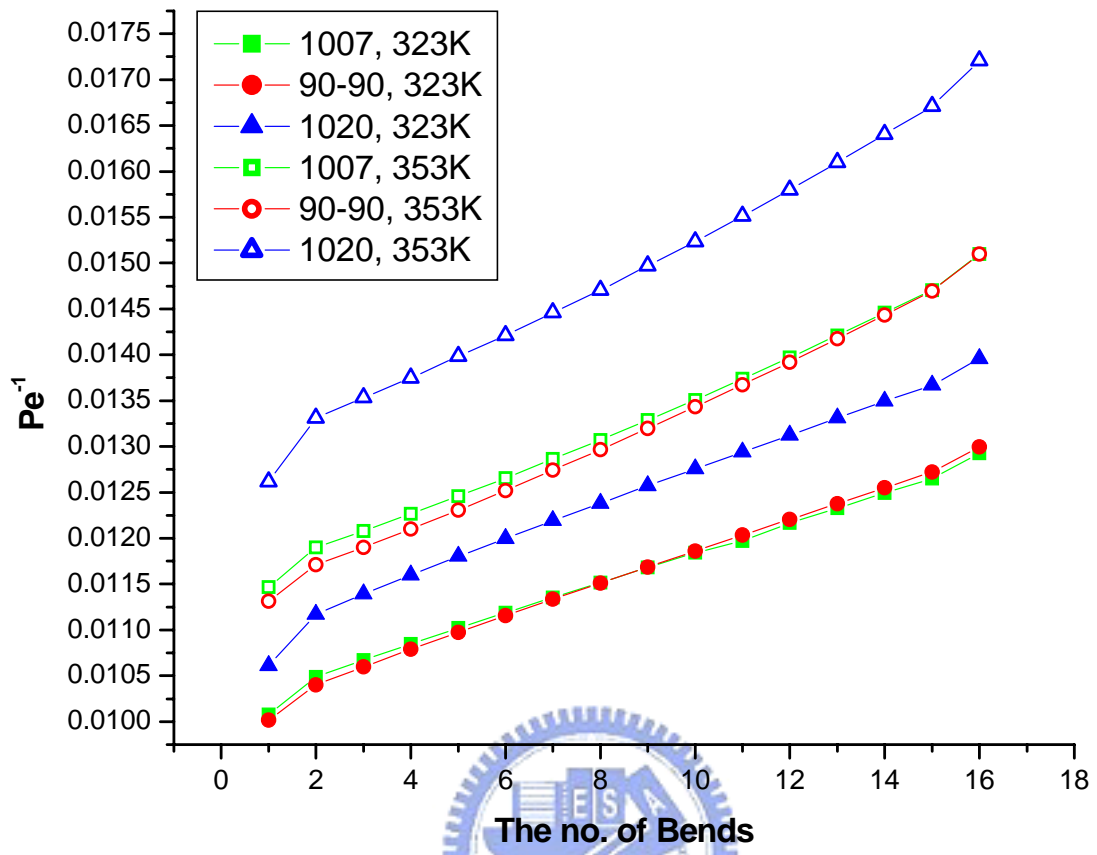


Fig. 4.27 The inverse of Peclet number at each bend entrance.

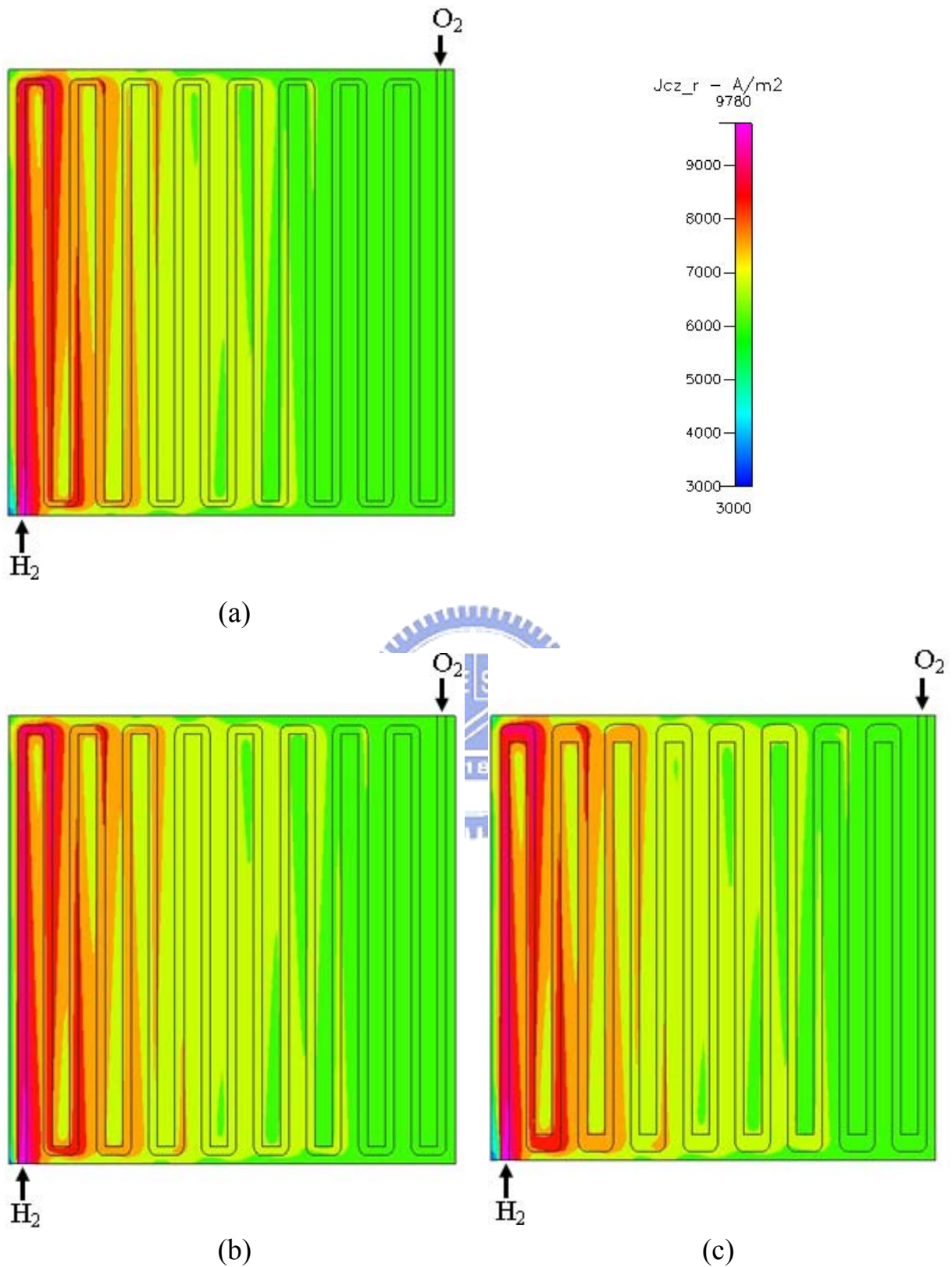


Fig. 4.28 Distributions of current density in membrane at 323K (0.4V): (a) 1007 flow pattern; (b) 90-90 flow pattern; (c) 1020 flow pattern.

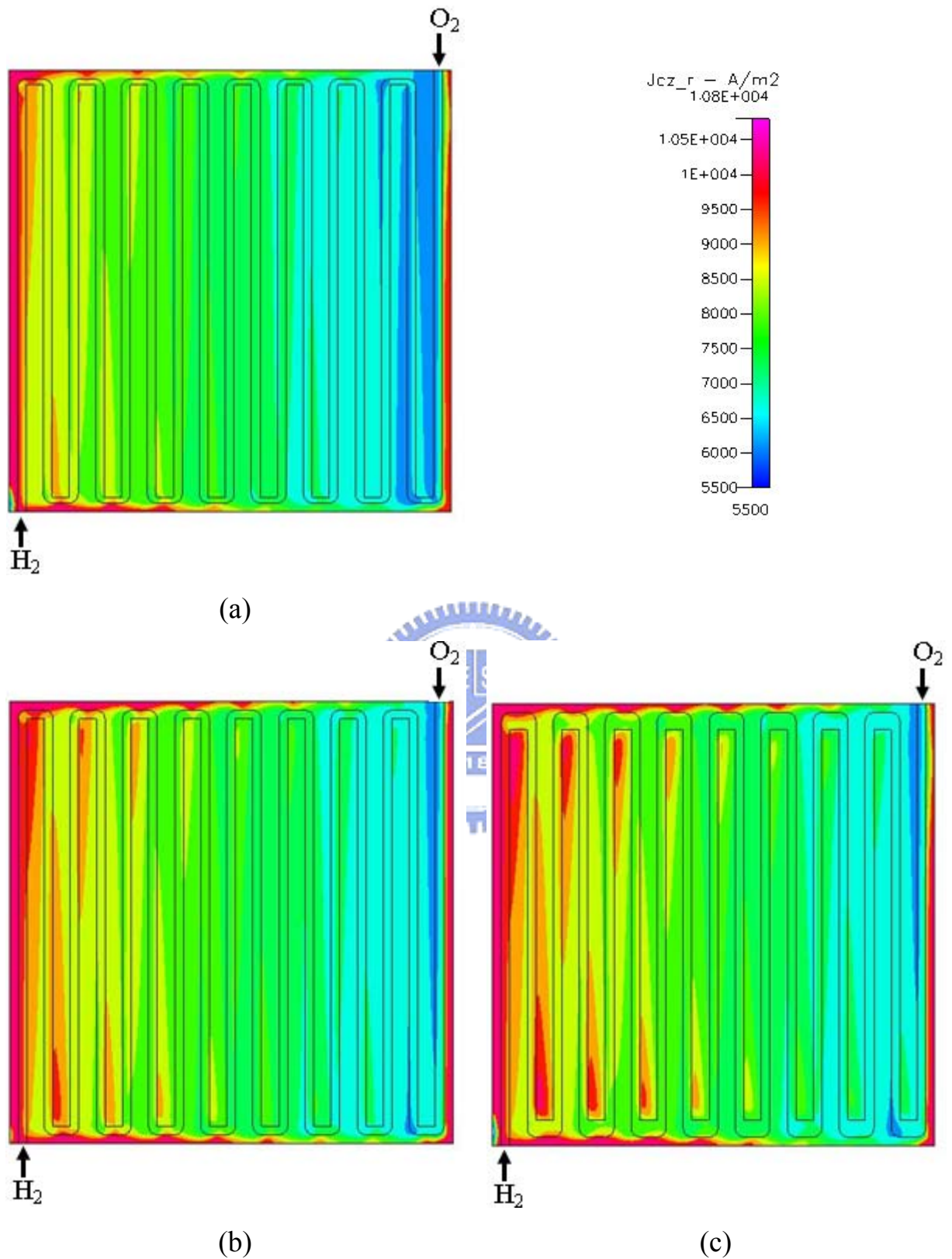


Fig. 4.29 Distributions of current density in membrane at 353K (0.4V): (a) 1007 flow pattern; (b) 90-90 flow pattern; (c) 1020 flow pattern.

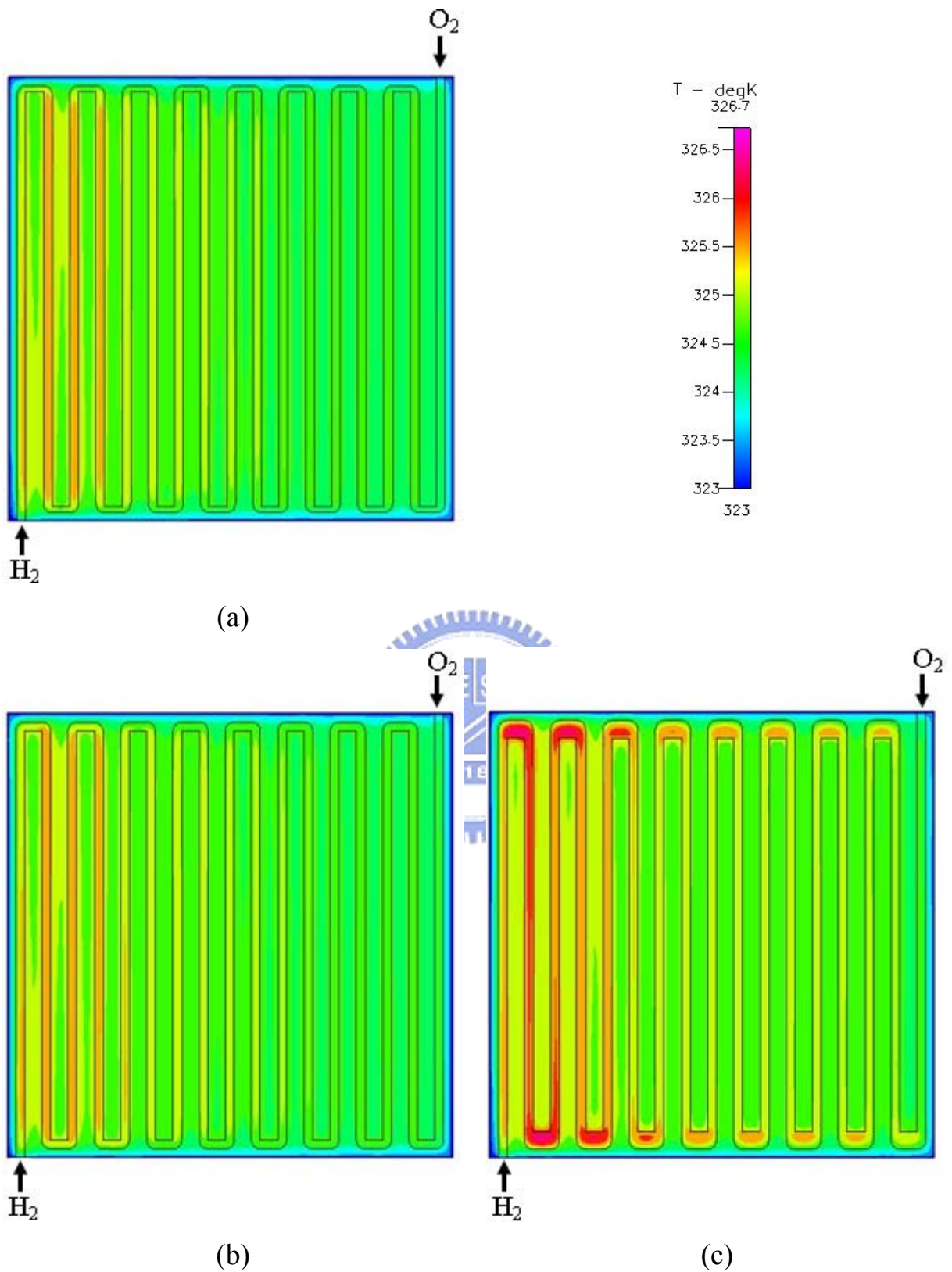


Fig. 4.30 Distributions of temperature in membrane at 323K (0.4V): (a) 1007 flow pattern; (b) 90-90 flow pattern; (c) 1020 flow pattern.

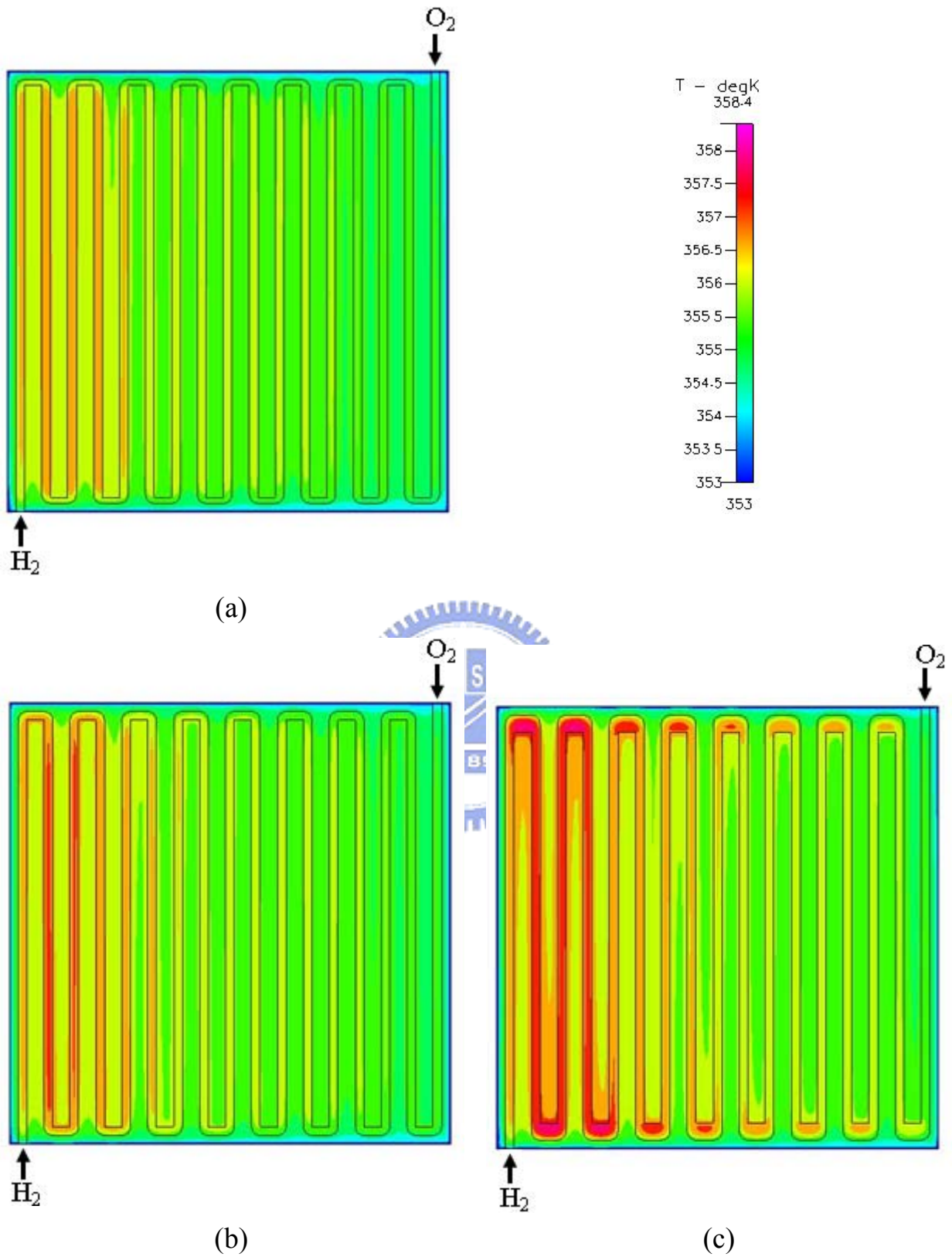


Fig. 4.31 Distributions of temperature in membrane at 353K (0.4V): (a) 1007 flow pattern; (b) 90-90 flow pattern; (c) 1020 flow pattern.



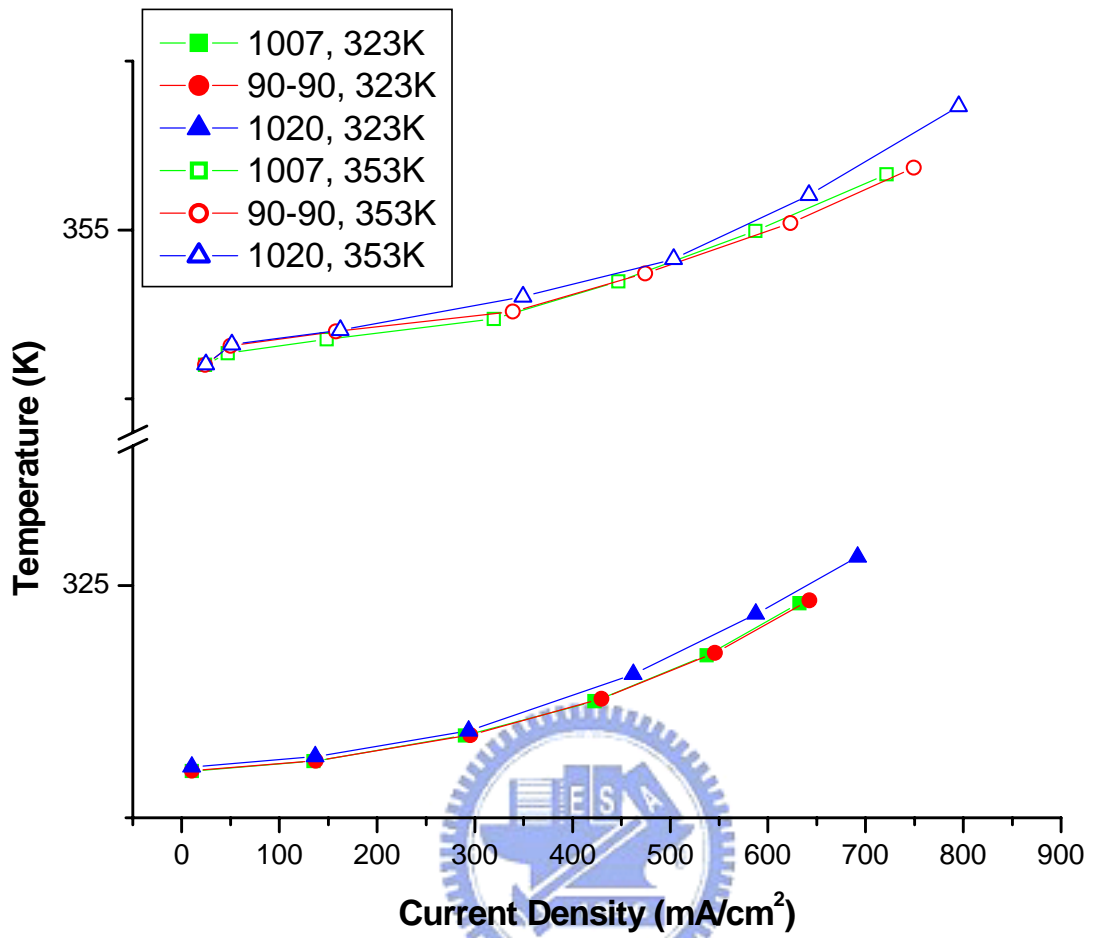


Fig. 4.32 Average value of temperature in membrane at 323K and 353K.

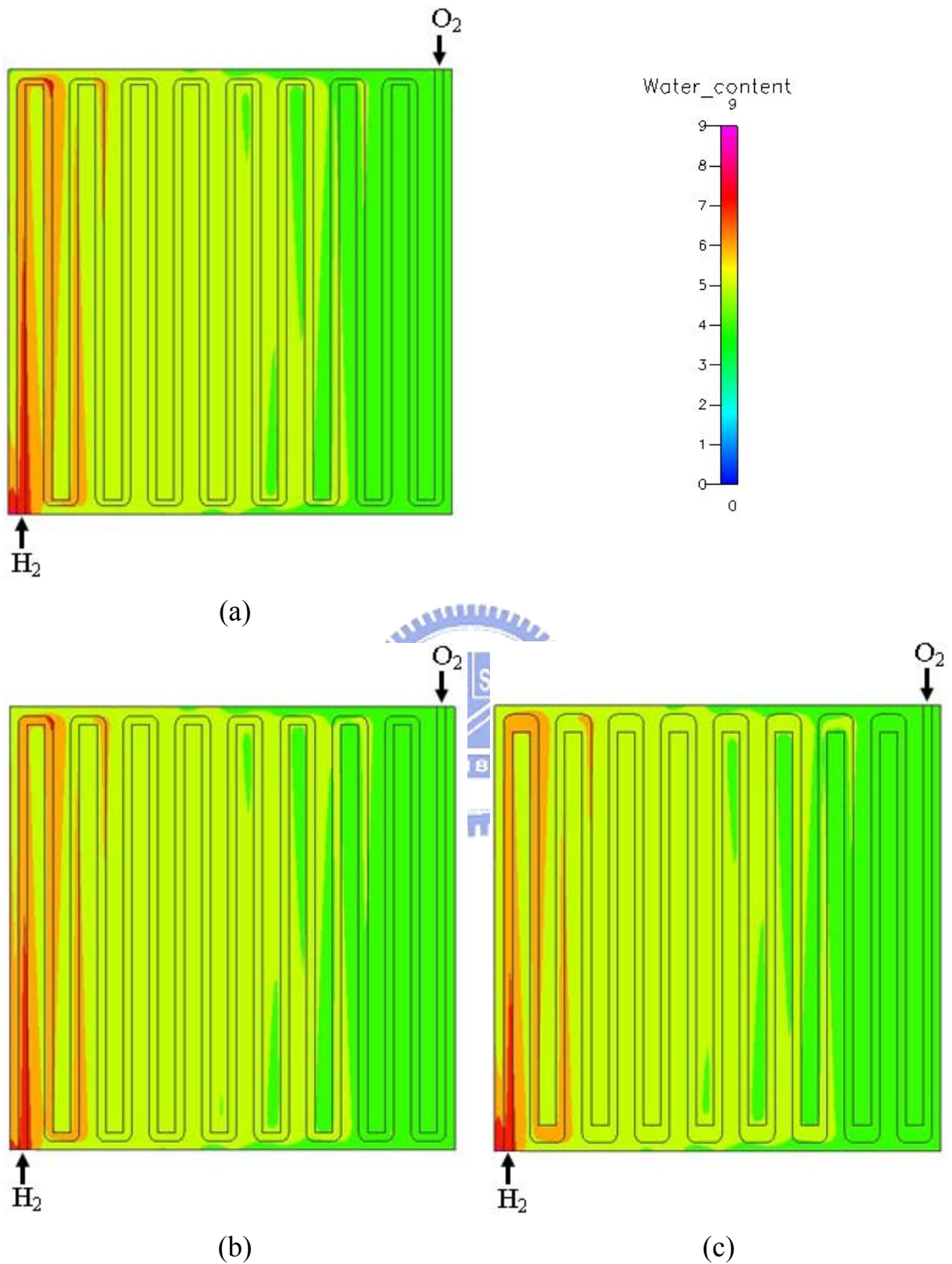


Fig. 4.33 Distributions of water content in membrane at 323K (0.4V): (a) 1007 flow pattern; (b) 90-90 flow pattern; (c) 1020 flow pattern.

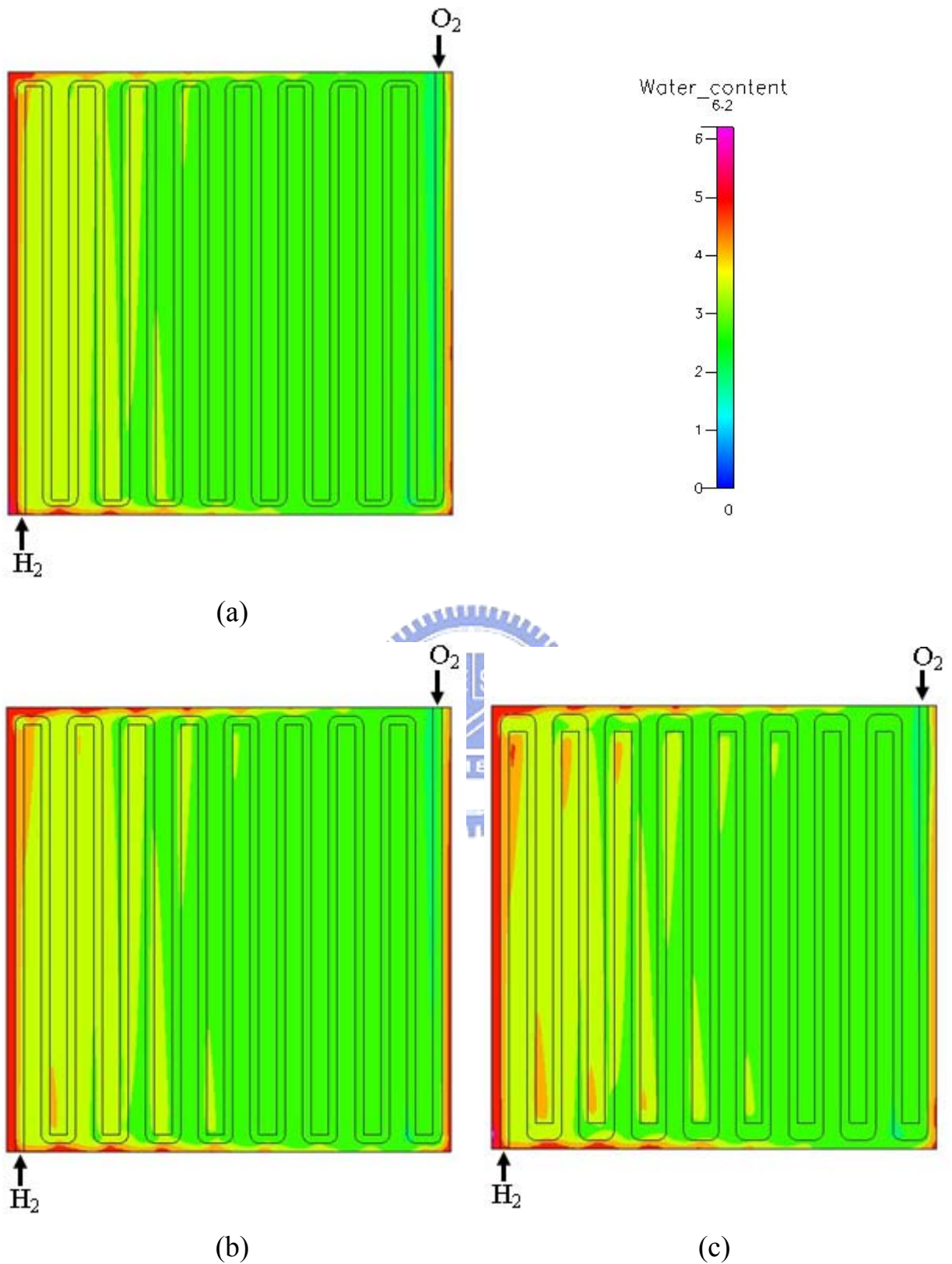


Fig. 4.34 Distributions of water content in membrane at 353K (0.4V): (a) 1007 flow pattern; (b) 90-90 flow pattern; (c) 1020 flow pattern.

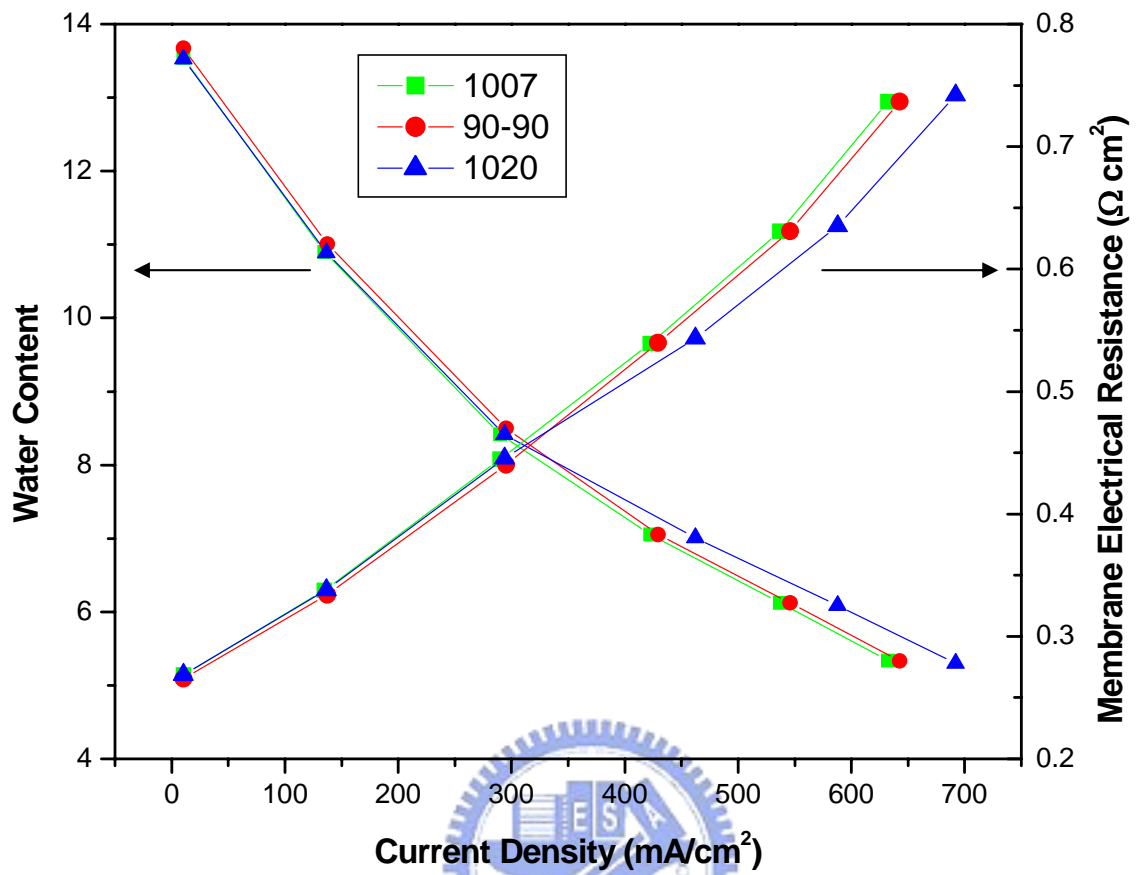


Fig. 4.35 Average value of membrane water content at 323K.

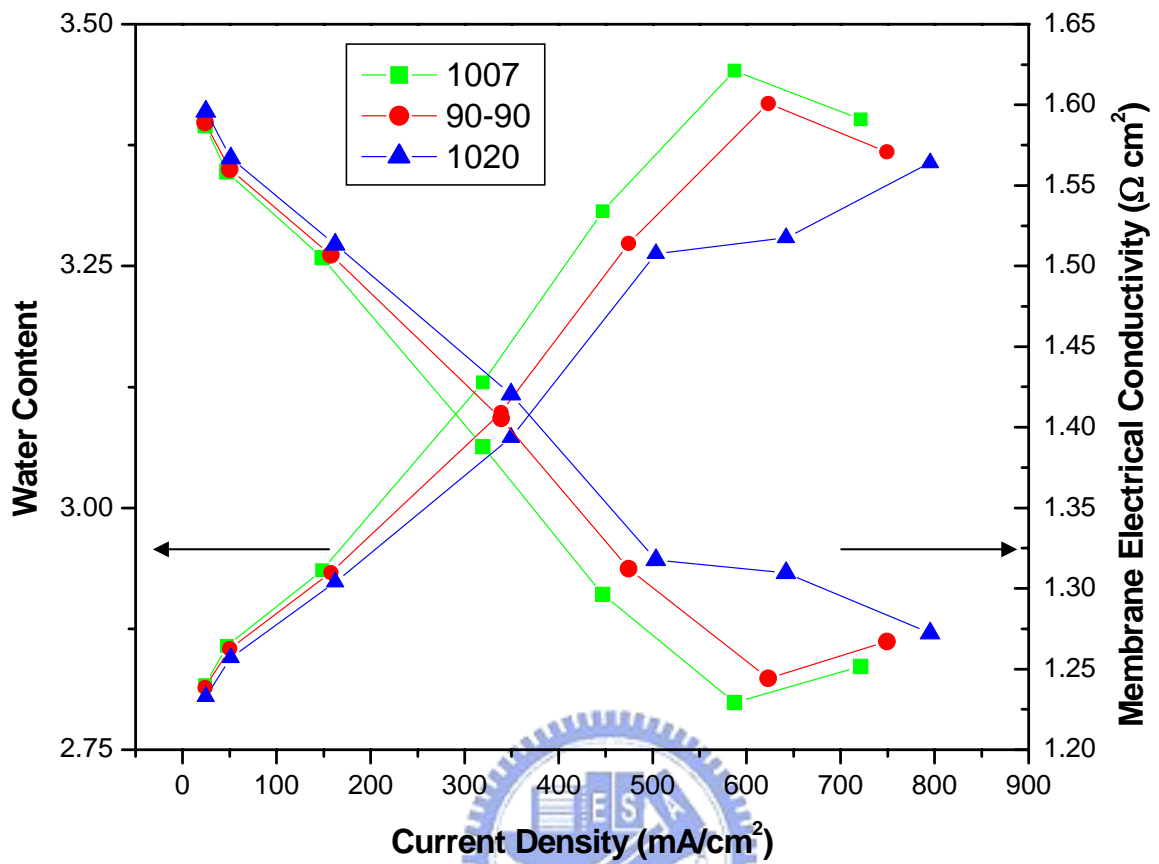


Fig. 4.36 Average value of membrane water content at 353K.

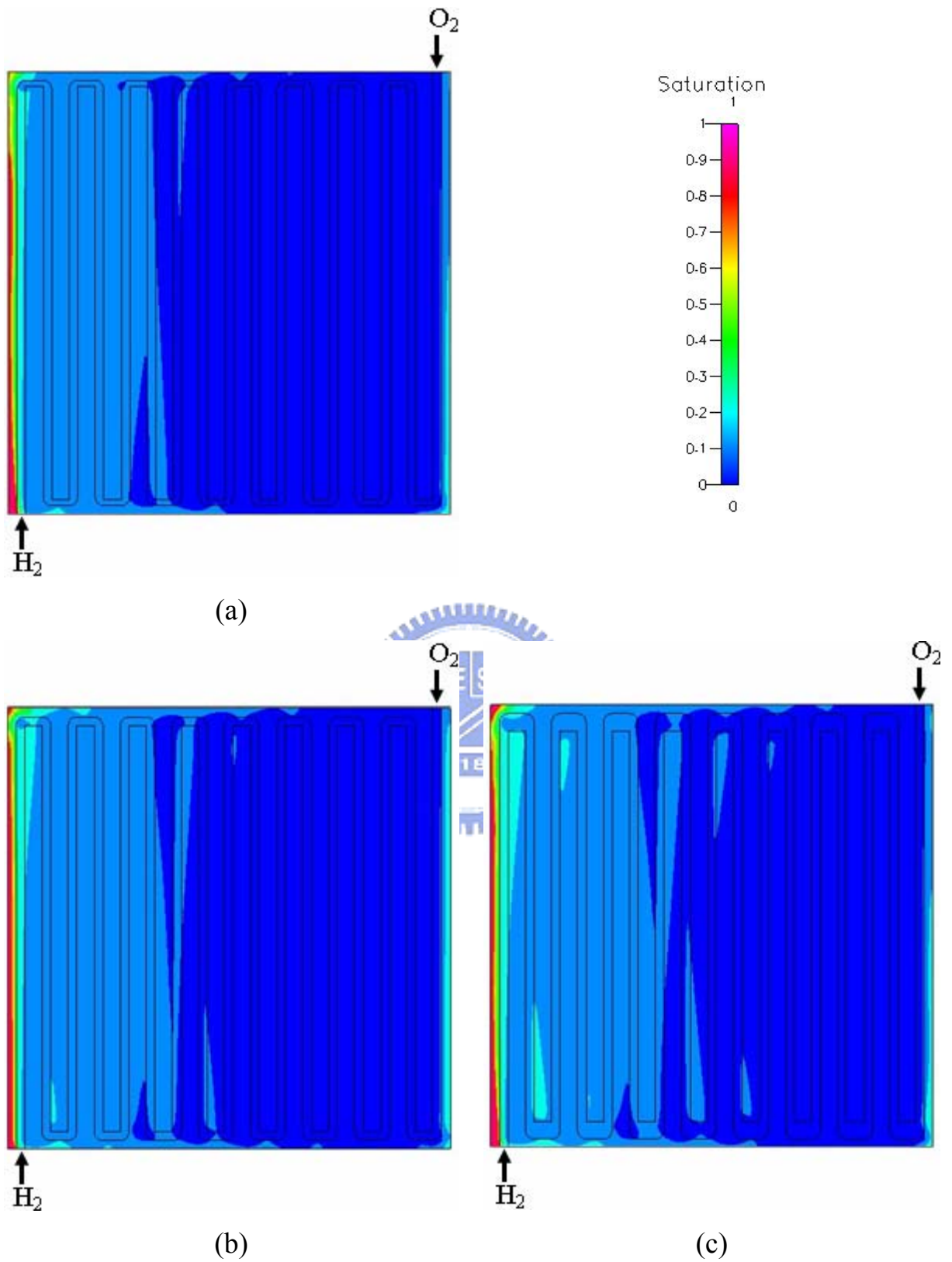


Fig. 4.37 Distributions of saturation on the interface between cathodic GDL and catalyst layer at 323K.

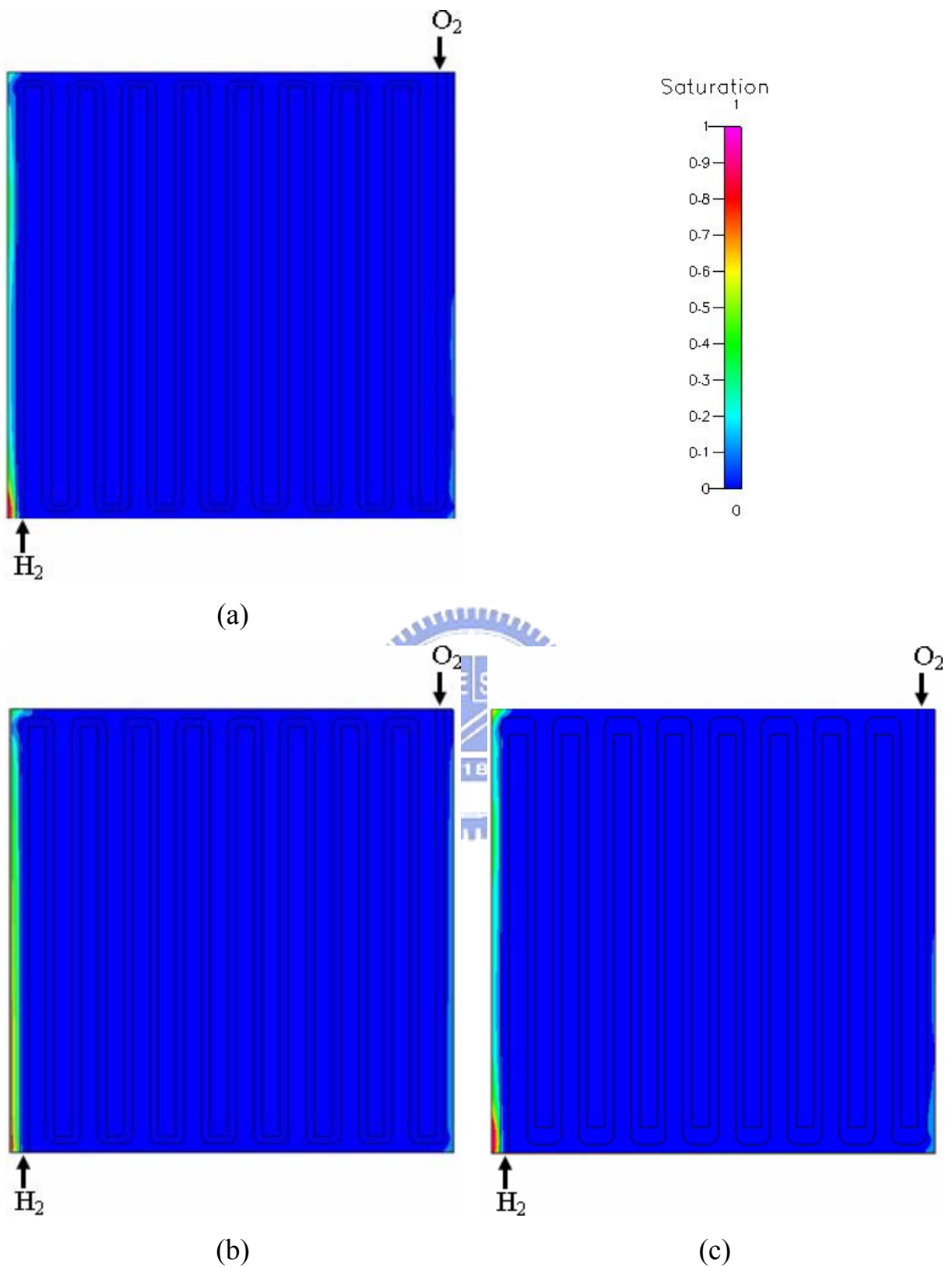


Fig. 4.38 Distributions of saturation on the interface between cathodic GDL and catalyst layer at 353K.

# Chapter 5

## Conclusions and Future Works

### 5.1 Conclusions

In this study, a steady, two-phase, multi-component and electrochemical model is presented to investigate the effects of geometries on performance of a 25 cm<sup>2</sup> PEMFC. The three-dimensional simulations are performed using a commercial package, CFD-ACE+. Five different flow patterns and their effects on PEMFC are investigated. The resultant polarization curves and variable distributions for these flow patterns are analyzed.

The fundamental behavior of flow field, temperature and other variables are analyzed in the first part. The hydrogen concentration is found to be the dominant factor affecting the distributions of current density, temperature and water content. Also, from the comparison of their distributions, it indicates that there exists a positive correlation between these variables. The variations of temperature and reacting gases on the cathode are comparatively significant comparing to the variations on the anode. Additionally, most liquid water accumulates at the anodic inlet, where the local current density appears to be high.

The second part of this research studies the effects of bend angle on the PEMFC performance with three different flow patterns at two operating temperatures, 323K and 353K, respectively. The results show that 60–120 pattern achieves the best performance at both operating temperatures due to highest mass diffusion rate, especially at low operating voltage regime. Also,



the current density at the bending areas is increased by such pattern. However, the improvement is achieved with the existence of significant variation in current density, indicating that the distribution uniformity of current density is not improved incrementally by the change of bend angle. On the other hand, water content distributions for these three patterns appear good uniformity that can reduce mechanical stress in the membrane. Note that the performances of 45–135 and 90–90 patterns are more or less similar because they show the good agreements with their variable distributions.

Three flow patterns with different bend widths are subsequently studied under the same cell temperatures stated before, in the analyses of effects of bend width on performance PEMFC. The simulations show that with wider bend 1020 pattern achieves the highest performance at both 323K and 353K since there exist expansions that enhance mass diffusion rate in channels. However, the uniformities of current density and temperature are comparatively low in 1020 to narrower bend with the existence of hot spots in the bending areas of 1020. On the other hand, high uniformity of water content is shown in the 1020 as well as the pattern with narrower bend width. Considering high performance of flow pattern with wider bend width, 1020 would be advantageous for PEMFC. However, for the practical use, there should be a compromise between PEMFC lifetime and performance.

## **5.2 Future works**

As to the future extension, current model will incorporate thermal stress analysis to study the influence of temperature variation in the membrane discussed before. It would also be necessary to develop a transient model to

study the liquid water transport with different flow patterns inside a PEMFC which has a more complicated manipulation. This is because water management, to control the water transport to avoid dehydration and flooding, is another critical issue to improve performance of PEMFC. Therefore, an understanding of flow mechanism of water transport is required for the proper flow pattern design and the optimization of operating conditions and may discover some new phenomena in PEMFC. In addition, it would be interesting to apply current flow patterns to micro PEMFC. Understanding the influences of bend angle and width on performance of micro PEMFC is indispensable for flow pattern development to establish universal heuristics and Peclet number correlations in the design of flow pattern and cell stacks.



## References

1. H. L. Trent and R. Somerville, Historical Overview of Climate Change Science, Technical Report, 2007.
2. J. Larminie and A. Dicks, Fuel Cell Systems Explained, second ed., Wiley, 2005.
3. R. O'Hayre, S. W. Cha, W. Colella and F. B. Prinz, Fuel Cell Fundamentals, Wiley, New York, 2006.
4. D. M. Bernardi, and M. W. Verbrugge, Mathematical Model of a Gas Diffusion Electrode Bounded to a Polymer Electrolyte, J. Electrochemical Society, Vol. 37, pp. 1151-1163, 1991.
5. T. E. Springer, T. A. Zawodzinski and S. Gottesfeld, Polymer Electrolyte Fuel Cell Model, J. Electrochemical Society, Vol. 138, No 8, Aug. 1991.
6. D. M. Bernardi, and M. W. Verbrugge, Mathematical Model of a Solid Polymer Electrolyte Fuel Cell, J. Electrochemical Society, Vol. 139, pp. 2477-2490, 1992.
7. C.Y. Wang and P. Cheng, Multiphase Flow and Heat Transfer in Porous Media, Advances in heat transfer, Vol. 30, pp.93-196, 1997.
8. W. S. He, J. S. Yi and T. V. Nguyen, Two-phase flow model of the cathode of PEM fuel cell using interdigitated flow fields, AIChE Journal, Vol. 46, pp. 2053-2064, 2000.
9. S. Um, C. Y. Wang and K. S. Chen, Computational fluid dynamics modeling of proton exchange membrane fuel cells, J. Electrochem. Soc., Vol. 12, pp. 4485-4493, 2000.
10. Z. H. Wang, C. Y. Wang and K.S. Chen, "Two-Phase Flow and Transport in the Air Cathode of Proton Exchange Membrane Fuel Cells", J. Power

- Sources, Vol. 94, pp. 40-50, 2001.
11. S. Mazumder and J. V. Cole, Rigorous 3-D mathematical modeling of PEM fuel cells I. Model Predictions without liquid water transport, J. Electrochem. Soc., Vol. 150, pp. A1503-A1509, 2003.
  12. S. Mazumder and J. V. Cole, Rigorous 3-D mathematical modeling of PEM fuel cells II. Model Predictions with Liquid Water Transport, J. Electrochem. Soc., Vol. 150, pp. A1510-A1517, 2003.
  13. E. Hontañón, M. J. Escudero, C. Bautista, P. L. García-Ybarra and L. Daza, Optimisation of flow-field in polymer electrolyte membrane fuel cells using computational fluid dynamics techniques, J. Power Sources, Vol. 86, pp. 363-368, 2000.
  14. J. Scholta, G. Escher, W. Zhang, L. Küppers, L. Jörissen and W. Lehnert, Investigation on the influence of channel geometries on PEMFC performance, J. Power Sources, Vol. 155, pp. 66-71, 2006.
  15. M. S. Chiang and H. S. Chu, Numerical investigation of transport component design effect on a proton exchange membrane fuel cell, J. Power Sources, Vol. 160, pp. 340-352, 2006.
  16. S. Shimpalee and J. W. Van Zee, Numerical studies on rib & channel dimension of flow-field on PEMFC performance, Int. J. Hydrog. Energy, Vol. 32, pp. 842-856, 2007.
  17. S. Fell, J. Roth, B. Steidle, D. Baker, W. Gu, M. Mathias and M. Schoeneweiss, VDI Berichte, pp. 579-600, 2002.
  18. S. Shimpalee, U. Beuscher and J. W. Van Zee, Investigation of gas diffusion media inside PEMFC using CFD modeling, J. Power Sources, Vol. 163, pp. 480-489, 2006.
  19. L. Matamoros and D. Brüggemann, Numerical study on PEMFC's

- geometrical parameters under different humidifying conditions, *J. Power Sources*, Vol. 172, pp. 253-264, 2007.
20. J. Zhang, Y. Tang, C. Song, Z. Xia, H. Li, H. Wang, J. Zhang, PEM fuel cell relative humidity (RH) and its effect on performance at high temperatures, *Electrochim. Acta*, Vol. 53, pp. 5315-5321, 2008.
21. M. Coppo, N. P. Siegal and M. R. von Spakovsky, On the influence of temperature on PEM fuel cell operation, *J. Power Sources*, Vol. 159, 560-569, 2006.
22. M. A. R. S. Al-Baghdadi, A CFD study of hygro-thermal stresses distribution in PEM fuel cell during regular cell operation, *Renew. Energy*, pp. 1-9, 2008.
23. J. Soler, E. Hontañón, L. Daza, Ekectride permeability and flow-field configuration: influence on the performance of a PEMFC, *J. Power Sources*, Vol. 118, pp. 172-178, 2003.
24. P. H. Oosthuizen, L. Sun, K. B. McAuley, The effect of channel-to-channel gas crossover on the pressure and temperature distribution in PEM fuel cell flow plates, *J. Appl. Thermal Engrg.*, Vol. 25, pp. 1083-1096, 2005.
25. S. Shimpalee, S. Greenway and J. W. Van Zee, The impact of channel length on PEMFC flow-field design, *J. Power Sources*, Vol. 160, pp. 398-406, 2006.
26. S. Karvonen, T. Hottinen, J. Saarinen and O. Himanen, Modeling of flow field in polymer electrolyte membrane fuel cell, *J. Power Sources*, Vol. 161, pp. 876-884, 2006.
27. L. Sun, P. H. Oosthuizen and K. B. McAuley, A numerical study of channel-to-channel flow cross-over through the gas diffusion layer in a PEM-fuel-cell flow system using a serpentine channel with a trapezoidal

- cross-sectional shape, *Int. J. Therm. Sci.*, Vol. 45, pp. 1021-1026, 2006.
28. J. Park and X. Li, An experimental and numerical investigation on the cross flow through gas diffusion layer in a PEM fuel cell with a serpentine flow channel, *J. Power Sources*, Vol. 163, pp. 853-863, 2007.
29. D. H. Jeon, S. Greenway, S. Shimpalee and J. W. Van Zee, The effect of serpentine flow-field designs on PEM fuel cell performance, *Int. J. Hydrog. Energy*, Vol. 33, pp. 1052-1066, 2008.
30. F. P. Incropera, D. P. Dewitt, T. L. Bergman and A. S. Lavine, *Fundamentals of Heat and Mass Transfer*, sixth ed., Wiley, 2007.
31. C. R. Wilke, A Viscosity Equation for Gas Mixtures, *J. Chem. Phys.*, Vol. 18, pp. 517-519, 1950.
32. J. O. Hirschfelder, C. F. Curtiss and R. B. Bird, *Molecular Theory of Gases and Liquids*, Wiley, New York, 1954.
33. M. Khandelwal and M. M. Mench, Direct measurement of through-plane thermal conductivity and contact resistance in fuel cell materials, *J. Power Sources*, Vol. 161, pp. 1106-1115, 2006.
34. S. Um and C. Y. Wang, Three-dimensional analysis of transport and electrochemical reactions in polymer electrolyte fuel cells, *J. Power Sources*, Vol. 125, pp. 40-51, 2004.
35. *CFD-ACE+ V2007 User Manual*, ESI CFD Inc.
36. J. P. Van Doormal and G. D. Raithby, Enhancements of the SIMPLE method for predicting incompressible fluid flows, *Numer. Heat Transfer*, pp. 147-163, 1984.
37. M. G. Santarelli and M. F. Torchio, Experimental analysis of the effects of the operating variables on the performance of a single PEMFC, *Energy Convers Manage*, Vol. 48, pp. 40-51, 2007.

38. A. D. Le, B. Zhou, Fundamental understanding of liquid water effects on the performance of a PEMFC with serpentine-parallel channels, *Electrochim. Acta*, Vol. 54, pp. 2137-2154, 2009.
39. X. Liu, H. Guo, F. Ye and C. F. Ma, Water flooding and pressure drop characteristics in flow channels of proton exchange membrane fuel cells, *Electrochim. Acta*, Vol. 52, pp. 3607-3614, 2007.
40. E. Arato, M. Pinna and P. Costa, Gas-phase mass-transfer resistance at PEMFC electrodes Part2. Effects of the flow geometry and the related pressure field, *J. Power Sources*, Vol. 158, pp. 206-212, 2006.

